STRUCTURE-PROPERTY RELATIONS IN BUBBLE AND SOLID PARTICLE SUSPENSIONS WITH MODERATE REYNOLDS NUMBERS

A Dissertation

Presented to the Faculty of the Graduate School

of Cornell University

in Partial Fulfillment of the Requirements for the Degree of

Doctor of Philosophy

by

Xiaolong Yin

January 2007

STRUCTURE-PROPERTY RELATIONS IN BUBBLE AND SOLID PARTICLE SUSPENSIONS WITH MODERATE REYNOLDS NUMBERS

Xiaolong Yin, Ph.D.

Cornell University 2007

In this study, several important properties of inertial bubble and solid particle suspensions have been characterized using numerical simulations. These properties include the hindered settling velocity and microstructure in solid particle suspensions, the scaling of the velocity variance and hydrodynamic diffusivity in solid particle suspensions, the hindered rise velocity and microstructure in suspensions of monodisperse, spherical, non-coalescing bubbles, and the lift force on bubbles in a sheared suspension. In order to simulate suspensions of monodisperse, spherical, non-coalescing bubbles, a lattice-Boltzmann boundary rule was designed. On the last subject, the lift force in a sheared suspension, experiments have also been conducted to verify the simulations.

BIOGRAPHICAL SKETCH

The author was born in Huhehaote, the capital city of Inner Mongolia, China, in the year immediately after the great "Cultural Revolution" was ended. Shortly after he was born, he was sent to Shenyang, an industrial city in the heart of Manchuria, to be raised by his grandparents, because both his parents were accepted into universities, which was an exceptional opportunity at that time. At the age of five, the author moved with his parents to Lanzhou, a city in the northwest, and spent fourteen years there until he went to Peking (Beijing) University in 1995. He earned a BS in theoretical and applied mechanics in June 1999 and decided to pursue a graduate degree overseas. He first studied at Lehigh University and received an MS in mechanical engineering, and then he entered the chemical engineering PhD program at Cornell University in August 2001.

ACKNOWLEDGEMENTS

I would like to thank my advisor, Professor Koch, whose patience and insightful guidance have made this work possible. Additionally, I would like to thank Professor Joo and Professor Louge, for their valuable advice and serving on my committee.

I am also grateful to Rolf Verberg, who introduced me to the lattice-Boltzmann method, Ying Tsang, who showed me how to operate the bubble channel apparatus, and Glenn Swan, who has been able to make every design into a workable device.

My thanks also go to my group members and officemates, for the help, discussions, and friendship over the years: Ganesh Subramanian, Chao Yang, Luying Wang, Jaehun Chun, Mansoo Shin, Paul Duru, Cormac Byrne, Yongmin Lee, and Eric Theisen.

Finally, I thank my fiancée, Xinran Li, for her love and unconditional support.

TABLE OF CONTENTS

LIST OF TABLES

LIST OF FIGURES

Chapter 1

Properties and Flow Behavior of Inertial Suspensions

1.1 Introduction

Suspensions of particles, drops, or bubbles are involved in many natural and industrial processes. One example of the natural processes involving suspensions is the transport of sediment in surface water systems (streams, rivers, lakes, etc.), which, over millions of years, can have great impact on the landscape, such as the formation of deep gorges and large river deltas. Examples of industrial applications of suspensions include many nuclear, chemical, and biological reactors, internal combustion and jet engines with fuel injection, paint, ink, etc. Understanding the properties and the flow behavior of suspensions, thus, is very important. This work focuses on the properties of inertial suspensions where the effect of inertia is important even at the smallest length scale — the size of individual particles, drops, or bubbles. More specifically, we considered two types of suspensions: one type consists of monodisperse spherical solid particles; another type consists of monodisperse, spherical and non-coalescing bubbles. The properties of interests are: the relation between the drag and the concentration of the discrete phase, the microstructure in inertial suspensions, and the response of inertial bubble suspensions to a linear shear.

The inertial effect in our suspensions is measured by the Reynolds number

$$\mathrm{Re} = \rho_f u d/\eta \ , \tag{1.1}$$

and the Stokes number

$$\mathrm{St} = \rho_d u d/\eta \ , \tag{1.2}$$

where u is a characteristic velocity, d is the size of the particle or bubble, η is the viscosity of the continuous phase, and ρ_f and ρ_d are the densities of the continuous phase and the discrete phase, respectively. Clearly, Re measures the inertia of the continuous phase and St measures the inertia of the discrete phase. The ratio between St and Re is the density ratio ρ_d/ρ_f. In the solid particle suspensions that we studied in this work, both Re and St are moderate. In the bubble suspensions that we studied, St is zero but Re is always kept moderate.

For these finite Re suspensions, there is a large body of experimental studies available. To discuss these experimental studies in detail is beyond the scope of this work. Thus, we only list here a few most notable contributions. On the relation between the drag and the volume fraction in a suspension of freely settling solid particles, Richardson and Zaki [110] proposed that the hindered settling velocity can be expressed as a power-law function of $1-\phi$, ϕ being the volume fraction of the suspension. On the velocity fluctuations of solid particles in finite Re suspensions, there are the papers by Parthasarathy and Faeth [105, 104]. On the rise velocity and fluctuations in bubble suspensions, the most well controlled experiments were conducted by Zenit *et al.*[138, 140]. On the microstructure, the work by Cartellier and Rivière [15] suggests that the pair probability distributions in finite Re bubble suspensions are not random but have deficits in the vertical direction. These experimental studies are very important, because they provide valuable information

on the properties of finite Re suspensions. It is worth pointing out, however, that experimental studies have two severe limitations. First, the quality of experiments depends strongly on how well the experimental conditions were controlled. For example, in experiments involving solid particle suspensions, it is important to be able to control and assess the effects of the polydispersity and non-sphericity of the particles. In bubble suspensions, the situation is more complicated — bubbles are deformable, and they can coalesce and break. Thus, to get a better understanding of how different factors affect the properties of suspensions, one must put great effort in improving the experimental conditions such that the factor of interest can be isolated and other non-ideal effects can be minimized. Second, even in well-controlled experiments, quantities such as the fluctuations in particle or bubble velocities and the microstructure are very difficult to measure, especially when the concentration of the discrete phase is high. These quantities, however, can have a significant effect on the rheology of the suspension. Due to these limitations present in the experiments, direct numerical simulations of suspensions, where one can have a better control of parameters, are essentially important in improving our understanding of these suspensions.

The need for direct numerical simulations is specifically important for inertial suspensions with finite Reynolds numbers, because the dynamics in such suspensions is particularly difficult due to the anisotropic hydrodynamic interactions and the nonlinearity of the flow. In finite Re suspensions, the anisotropy in the hydrodynamic interactions is enhanced by the fact that the velocity disturbance around an isolated particle or bubble does not have the fore-aft symmetry that is seen around a low Re particle or bubble. The nonlinearity, on the other hand, comes from the convective term in the Navier-Stokes equation, which is impossible to re-

duce when Re is finite. It is well known that theoretical modelling of particle and bubble suspensions are available when Re is either very small or very large. In the low Re limit, if St is also very small, the inertial effect can be totally ignored and the governing equations are linear, which makes it possible to superpose many individual solutions to satisfy the complex boundary condition in a suspension. One example of such studies is by Mo and Sangani [93]. When Re is very small but St is very large (e.g. in a gas-solid suspension), we can either neglect the continuous phase completely, as what has been done in various granular flow theories, or use the viscous drag to represent the leading order effect of the continuous phase and develop a kinetic theory [59, 116, 63]. When Re is large and St is zero, as in a high Re bubble suspension, the vorticity produced by a bubble is confined in a very thin boundary layer, and the flow outside the boundary layer can be regarded as a gradient of a velocity potential [94, 95]. As the equations governing the velocity potentials are also linear, it is possible then to treat high Re bubble suspensions in a similar way to low Re suspensions and establish theories [137, 121]. When Re is intermediate, we cannot neglect the inertial term in the Navier-Stokes equations, nor can we assume that the flow in the continuous phase is a potential one. The best way to study such suspensions, thus, is through direct numerical simulations.

Since direct numerical simulations have a high demand of computational power, it is only recently that large scale simulations of three-dimensional suspensions with hundreds of particles or bubbles become available. Although there are a number of numerical studies available to date involving inertial particle and bubble suspensions, many of them focus on simulation method and only relatively few of them have studied the properties of the suspensions systematically. Such works include those by Wachmann and coworkers [130, 131], Pan *et al.*[102], and Climent and

Maxey [25] on solid particle suspensions, and those by Esmaeelli and Tryggvason [34, 35, 36], and Bunner and Tryggvason [10, 11, 12] on bubble suspensions. These simulations have successfully obtained some suspension properties such as hindered settling or rise velocities, velocity variance, and limited information on the microstructure. However, as we will discuss in detail in the next section, there are still many unresolved problems and our knowledge on finite Re suspensions is quite far from being complete.

1.2 Motivations

This study on finite Re solid particle and bubble suspensions is motivated by the lack of knowledge in the following areas:

The microstructural arrangement of the discrete phase due to the anisotropic pairwise hydrodynamic interactions at finite Re. In many experimental and numerical studies, it has been observed that when particles settle or bubbles rise, they tend to align in the direction perpendicular to the direction of gravity, and a deficit of particle or bubble can be found in the vertical direction [15, 138, 10, 25, 36]. This non-random distribution of particles or bubbles is believed to be the result of the anisotropic pairwise interaction at finite Re. However, a strict quantification of this non-randomness in terms of the pair probability density distributions has not been done.

The velocity fluctuations and hydrodynamic dispersions of particles in finite Re suspensions. It is well known that in unbounded low Re suspensions, due to the long-range hydrodynamic interaction, the velocity variance and hydrodynamic diffusivity of solid particles diverge algebraically with increasing

domain size [14, 61]. In dilute finite Re solid particle suspensions, based on a superposition of Oseen wakes, Koch [60] predicted that the velocity variance of solid particles will diverge logarithmically with increasing domain size. These diverging behaviors, however, are based on the assumption that the particles are randomly distributed in the suspension. When there is a non-random microstructure in the suspension, the divergence of the velocity variance can be partially screen or even totally suppressed [60, 64]. It is important, therefore, to examine from simulations the scaling of the velocity variance and the hydrodynamic diffusivity in unbounded finite Re suspensions with respect to domain size.

The properties of a simple bubble suspension with monodisperse, non-coalescing, spherical bubbles. The bubble suspensions are much more complex than solid particle suspensions, because bubbles are deformable, and they are able to coalesce or break, which can modify the size distribution of the suspension over time. Due to these complexities, it is desirable to have a simple suspension with monodisperse, non-coalescing, nearly spherical bubbles such that one can isolate and assess the effect of the free shear stress boundary condition on suspension properties. In experiments by Zenit *et al.*[138, 140], such suspensions were successfully generated by using an electrolyte solution. The role of the electrolyte (magnesium sulfate) is to suppress the coalescence between bubbles and maintain the free shear stress boundaries on bubble surfaces. In the experiments, Re is about 200. In this work, with a newly developed lattice-Boltzmann boundary rule [135], we are able to simulate suspensions of monodisperse, non-coalescing, spherical bubbles at reduced Reynolds numbers. As these simple bubble suspensions are different from solid particle suspensions only by the boundary conditions. Direct comparison between these two types of suspensions can give us valuable in-

formation on how boundary condition between the discrete and the continuous phases affects the behavior of a suspension.

The response of a bubble to a linear shear under the influence of hydrodynamic interactions. When a bubble moves in a flow field with a velocity gradient, it will experience a transverse force known as the lift force. For spherical bubbles, this lift force is an inertial effect, because the reversibility of the Stokes flow does not allow such a force to occur. The lift force on an isolated bubble has been studied in detail [2, 78, 79]. In a sheared suspension, however, the flow field around a bubble is modified by the presence of other bubbles. The lift force acting on a bubble in a sheared suspension, therefore, is not the same as that under the isolated condition. This difference is worth investigating, because in many practical bubbly flows, the effect of hydrodynamic interactions is not negligible. It is usually difficult to produce an ideal shear flow of a bubble suspension and isolate the lift force from other forces, such as the gradient of bubble phase pressure. In this study, it is found that a nearly viscometric flow can be generated in the middle of a slightly inclined channel, from which the lift force in a shear suspension can be accurately determined.

1.3 Outline

This dissertation is divided into six chapters. The role of the first chapter is to give an overview of the problems considered in this work. It also serves as a portal to the remaining chapters, which were written with the intention that they could be read by themselves without referencing other chapters too often. The remaining chapters have their own introductions, literature reviews, and descriptions of

methods. These chapters are arranged in a logical order that the later chapters can cite results from the previous chapters if necessary.

In the second chapter, we studied the microstructure in finite Re solid particle suspensions and its impact on the hindered settling behavior. The Reynolds numbers based on the terminal velocities of particles range from 1 to 20, the ratio of the solid to fluid density is $\rho_p/\rho_f = 2.0$, and the solid volume fraction is varied from 0.005 to 0.40. At volume fractions larger than about 0.05, the ratio of the mean settling velocity to the terminal velocity u^* can be fit by a power law expression $u^* = k(1-\phi)^n$ where k and n are functions of the Reynolds number based on the terminal velocity. The constant k is typically about 0.86 - 0.94 and u^* deviates from the power law behavior in dilute suspensions. The extent of this deviation increases with increasing Reynolds number. We show that the hindered settling velocity follows a power law when the particle microstructure is similar to that in a hard sphere suspension. The deviation from the power-law behavior can be correlated with an anisotropic microstructure resulting from wake interactions among the spheres. This microstructure, which occurs in dilute suspensions and is most pronounced at the higher Reynolds numbers explored in our study, consists of a decreased pair distribution function for pairs with vertical separation vectors and a peak in the pair distribution function for horizontal separations corresponding to about two particle diameters.

In the third chapter, we characterized the scaling of velocity variance and hydrodynamic diffusivity of particles in unbounded finite Re suspensions with respect to domain size. The simulations are carried out in cubic computational domains surrounded by periodic boundaries, where it is known that under Stokes flow condition the velocity variance and particle diffusivity will diverge algebraically with

increasing domain size. Our simulations show that with finite inertia the velocity variance does not depend on domain size as strong as in Stokes suspensions. Instead of an algebraic growth, the velocity variance in finite Re suspensions grow logarithmically with increasing domain size, in qualitative agreement with Koch's theory [60]. The magnitude of the velocity variance, however, is lower than the theoretical prediction due to a partial screening of the velocity disturbance in the wake region. The dispersion of particles is shown to be a random-walk process, and the particle diffusivities obtained in our simulations are proportional to the product of root-mean-square velocity and the domain size. Comparison between simulations with Re = 1 and Re = 10 reveals that both velocity variance and particle diffusivity decrease with increasing Reynolds number, because there are more large scale convective motions present in lower Re suspensions. The anisotropy in the velocity variance and the dispersion is the strongest in dilute, higher Re suspensions, possibly due to the influence of the anisotropic microstructure.

In the fourth chapter, we developed a lattice-Boltzmann method to recover the slip boundary condition at a liquid-gas interface. This rule enables one to use a single-component lattice-Boltzmann model to simulate bubbly flows where bubbles are nearly spherical and coalescence is prohibited. Numerical tests showed this method to be robust and accurate in simulating both steady and unsteady flows around spherical bubbles in the Reynolds number range $0 < Re < 30$.

In the fifth chapter, we used the method developed in Chapter 4 to simulate the free rise of bubbles in periodic domains and vertical channels. The bubbles are monodisperse, spherical and non-coalescing. The Reynolds numbers based on the terminal velocities are 5.4 and 20. We first characterized the average rise velocities and microstructure in unbounded, periodic computational domains. It is found

that the inertial interaction between pairs of bubbles creates a microstructure in which bubbles have a stronger tendency to align in the horizontal direction than solid particles with comparable Reynolds numbers. Chapter 2 reveals that in solid particle suspensions, there is a relation between the power-law behavior of the hindered settling velocity and a random, hard sphere-like microstructure. In bubble suspensions, the microstructure is more anisotropic than that in solid particles suspensions. Thus, the hindered rise velocity in bubble suspensions does not fit to power-law functions of $1 - \phi$ as well as the hindered settling velocity in solid particle suspensions. We then simulated the rise of bubbles in vertical channels with a pair of solid walls and determined the volume fraction and velocity profiles. We find that there are deficits of bubbles near the walls, and volume fraction peaks right next to the deficits. These high volume fraction peaks then induce layers that extend all the way into the bulk region. The distance between the layers equals the most probable separation between bubble pairs in unbounded suspensions.

In the last chapter, we generated a nearly viscometric shear flow of a homogeneous suspension of bubbles in the middle of a slightly inclined channel and obtained the effective lift force coefficient in a sheared suspension. We first simulated the free rise of monodisperse, non-coalescing, spherical bubbles in a slightly inclined channel. The volume fraction and flow profiles from simulations indicate that a nearly viscometric linear shear flow region is generated in the middle of the channel, where the volume fraction, shear rate, and relative velocity between the two phases are all constant. In this linear shear flow region, the force balance on the bubbles in the direction perpendicular to the walls involves only the gravity and the lift force. The effective lift force coefficients in sheared suspensions can therefore be determined accurately. The simulations indicate that the effective lift

force coefficients are higher than the lift force coefficients of isolated bubbles. An experimental study of bubbly flows in a slightly inclined channel is then conducted to verify the simulations, and it is found that the experimentally determined effective lift force coefficients are in good agreement with those obtained from the simulations.

Chapter 2

Settling Velocity and Microstructure in Finite Re Solid Particle Suspensions

2.1 Introduction

Sedimentation is a very common process in which solid particles settle through liquids under the influence of gravity. As the particle-fluid interaction in a sedimentation system is the same as in a steady and homogeneous liquid fluidized bed, sedimentation and liquid fluidization are often considered as closely related problems. The main subject of this chapter is the average settling velocity and the microstructure in sedimentation systems with non-negligible inertia. Here the inertia is measured by the Reynolds number $\mathrm{Re} = \rho_f u_t d/\eta$, where u_t is the terminal velocity of an isolated particle, d is the sphere diameter, ρ_f is the density of the fluid, and η is the viscosity. In this work, Re varies from 1 to 20, and the particle-fluid density ratio $\rho_p/\rho_f = 2$. Thus, both fluid phase inertia and particle phase inertia are important.

When the Reynolds number is vanishingly small, the Navier-Stokes equations that govern the flow in the continuous phase are reduced to a linear set of equations, and a number of well established simulation methods, many of which exploit the linearity of the problem, have been developed [70, 73, 74, 75, 98, 99, 106, 93]. The knowledge of the average settling velocity and microstructure in low Reynolds

number suspensions is comprehensive, while the velocity fluctuations in these systems have also received considerable attention. For suspensions of finite Reynolds number settling particles, the inertial term in the Navier-Stokes equation creates wakes behind settling particles, breaking the fore-aft symmetry of the velocity field around the particles and complicating the hydrodynamic interactions. Due to the nonlinearity of the inertial term, it is generally believed that the best way to study the properties of such inertial suspensions is through direct numerical simulations.

It is only relatively recently that numerical methods and computational power sufficient to characterize the average properties and microstructure of suspensions with significant microscale fluid inertia have become available. Among the challenges in this problem is the need for a method that can handle solving the nonlinear Navier-Stokes equation in the presence of a complex and evolving microstructure. The method must be capable of accurately describing the close interactions of particles that frequently occur in a suspension. It is also important to simulate a large number of particles over a long period of time to establish steady state flow properties characteristic of an unbounded suspension.

Efforts have been made to develop finite element simulations of the fluid motion in suspensions of freely suspended particles [54, 55, 56, 50, 51]. For example, Johnson and Tezduyar developed a finite element method [54] with an unstructured grid and simulated the sedimentation of hundreds of spheres [55, 56]. An advantage of these methods is that the grid between slightly separated particles can be refined to accurately capture lubrication forces. However, the need to regenerate the grid as the particle configuration changes leads to considerable computational challenges for these methods and so the work to date has focused primarily on method development rather than providing average suspension properties at steady states.

A simulation in which particles may move across a fixed grid may be more computationally efficient and is certainly simpler to implement. Wachmann and coworkers [130, 131] have used a finite difference method to solve the Navier-Stokes equation in a particle suspension. The no-slip boundary condition is applied at the particle surfaces and the particle velocities and rotation rates are updated based on the net force and torque exerted by the fluid on the particle surface. Pan *et al.*[102] have developed a method in which fluid is present inside as well as outside the particles. The fluid within the particle experiences a fluid-particle interaction force and Lagrange multipliers are used to enforce a condition that the flow within the particles is a rigid body motion. The equations of motion for both internal and external fluid are solved on a fixed finite element grid. The work of Kuusela *et al.*[69] is similar except that the particle-fluid interaction is treated in an explicit manner (integration of hydrodynamic stress over particle surface), and the equations are solved using a finite difference method. A general difficulty with such fixed grid methods is its inability to resolve the hydrodynamic lubrication stresses in the gaps between particles whose separation is comparable or smaller than the grid spacing. Thus, lubrication interactions are often dropped and either elastic collisions [130, 131, 69] or repulsive forces [102] are used to prevent particle overlap.

To date, none of these methods has been applied to determine the average flow properties and microstructure of unbounded settling suspensions with Reynolds numbers exceeding one. Wachmann and coworkers [130, 131] studied the hindered settling velocity and fluctuations in suspensions where $\mathrm{Re} = 0.5$. Pan *et al.*[102] studied the fluidization of many spheres with Reynolds numbers on the order of hundreds confined in a channel with a gap thickness comparable to the sphere

diameter. Kuusela *et al.*[69] simulated sedimentation with Re = 0.5 in channels with variable gap thickness (between 1.6 and 22.9 particle diameters) to study the effect of gap thickness on average properties.

Climent and Maxey have used an approximate method to simulate the hindered settling velocity and velocity fluctuations in unbounded suspensions with $0 < \mathrm{Re} < 10$ and $0.01 < \phi < 0.12$. In this method, the particles are represented by Gaussian force density distributions whose width is proportional to the particle size. The integral of this force density is independent of time and equal to the weight of the particle less the buoyancy. The entire computational domain is filled with fluid allowing a spectral method to be used to solve the fluid velocity on a fixed grid. However, the fluid within the particles does not satisfy a rigid body motion. The particle velocity is taken as the average of fluid velocity in the Gaussian envelope. A force barrier is set up to prevent the particles from overlapping. Because of these approximations, the authors limited their consideration to relatively dilute suspensions with $\phi < 0.12$.

In the present work, we will apply a lattice-Boltzmann method to obtain more accurate results for the hindered settling velocity in unbounded suspensions. We will consider an extended parameter range: $1 < \mathrm{Re} < 20$ and $0.005 < \phi < 0.40$ and will also characterize the particle microstructure and discuss how this influences the mean settling velocity. The lattice-Boltzmann method used in this study was developed by Ladd [71, 72]. The lattice-Boltzmann method reproduces the flow associated with the continuum incompressible Navier-Stokes equations when the particle size is large compared with the grid spacing. Greater accuracy can be achieved for finite particle radius to grid length ratios by using an effective particle radius set to reproduce the particle's Stokes drag force. The particles have well-

defined no-slip boundaries and the motions of the particles are determined by particle equations of motion that include particle inertia, gravitational forces and a surface integral of the hydrodynamic stresses. The lubrication interactions between particle pairs with separations comparable with the grid spacing is implemented explicitly using analytical results [97].

It is well known that the mean settling velocity in a homogeneous suspension of uniform spheres is less than the terminal velocity of an isolated sphere. The hindered settling velocity has been studied experimentally by many authors [110, 39, 109, 23, 13, 29, 43, 108, 32, 22, 31] and there are a number of empirical formulas available [110, 3, 39, 109, 28, 31]. The simplest and perhaps the best known of these formulae is the Richardson-Zaki [110] equation, which is based on sedimentation and liquid fluidization (under homogeneous expansion) experiments. In this equation, the hindered settling velocity u is expressed as a power-law function of $1-\phi$

$$u^* = \frac{u}{u_t} = (1-\phi)^n \ , \tag{2.1}$$

where u_t is the terminal velocity of an isolated particle in an unbounded fluid and n is the power-law exponent which depends on the Reynolds number based on u_t:

$$n = \begin{cases} 4.65 & , \quad \mathrm{Re} < 0.2 \\ 4.4\mathrm{Re}^{-0.03} & , \quad 0.2 < \mathrm{Re} < 1 \\ 4.4\mathrm{Re}^{-0.1} & , \quad 1 < \mathrm{Re} < 500 \\ 2.4 & , \quad 500 < \mathrm{Re} \end{cases} . \tag{2.2}$$

Garside and Al-Dibouni [39] conducted more ideal fluidization experiments and proposed a new expression for n

$$\frac{5.1-n}{n-2.7} = 0.1\mathrm{Re}^{0.9} \ , \tag{2.3}$$

which improves the accuracy of Eqs. (2.1) and (2.2) from $\pm 19.6\%$ to $\pm 9.8\%$ in the range of $0 < \mathrm{Re} < 30000$:

In later experimental studies [39, 109, 23, 29, 32, 31], it was found that there is a rapid increase in the settling velocity with decreasing volume fraction in dilute suspensions. The average velocity in this regime cannot be described by the power-law formulae Eqs. (2.1) to (2.3). The deviation from power-law behavior becomes more pronounced with increasing Re [39]. In view of this rapid change in the settling velocity at small volume fractions, the power-law valid for higher volume fractions:

$$u^* = k\,(1-\phi)^n \tag{2.4}$$

must include a pre-factor k, whose value has been found to be in the range of 0.8 to 0.9 [23, 32, 31].

In view of the extensive experimental evidence for the hindered settling velocities, they provide an excellent opportunity to validate numerical simulations of inertial suspensions. In our simulations, we find the hindered settling velocities in concentrated suspensions fits very well to power laws in the form of Eq. (2.4) with k varying between 0.86-0.94. In dilute suspensions deviations from the power laws are observed. When $\mathrm{Re} \leq 2$, k is close to one and the deviation is not very obvious; when $\mathrm{Re} \geq 5$, the deviation becomes more significant, consistent with experimental observations. More importantly, numerical simulations provide an opportunity to identify the mechanism leading to a deviation of the settling velocity from the power law in dilute suspensions. It is known that the nature of the microstructure can have a dramatic influence on the velocity variance in a settling suspension at zero or finite Reynolds numbers [14, 64, 60] even determining whether the variance grows with increasing system size. While the effect of a non-random microstruc-

ture on the mean velocity is more modest, we find that it does account for the observed deviation of the mean settling velocity from the power-law correlations at small volume fractions.

In Section 2.2 of this chapter, we briefly describe the numerical method — the lattice-Boltzmann method — and discuss the simulation protocol. In Section 2.3, we report the hindered settling velocities and the microstructure in dilute and concentrated suspensions of low and moderate Re and discuss their relations. In Section 2.4, we give conclusions of this chapter.

2.2 Lattice-Boltzmann Method

The computations presented here are conducted using the lattice-Boltzmann simulation method developed by Ladd [71, 72] for hard sphere suspensions. The details of the method are also discussed in the review article by Ladd and Verberg [76]. Rather than directly solving the continuum equations of motion, the lattice-Boltzmann method simulates the velocity distribution function for fluid molecules with a discrete set of velocities that allow the molecules to translate across a space filling lattice. The macroscopic quantities, such as mass, momentum, and stress, can then be obtained from the moments of the velocity distribution function. The update of the distribution function follows simplified kinetic models designed in such a way that the dynamics the macroscopic quantities obey the Navier-Stokes equation on large length and time scales.

The velocity distribution function in our lattice-Boltzmann method is a set of 19 different velocities that allow the fluid molecules to stay at the current lattice position [000], propagate to the nearest neighbors [100], or the next-nearest [110]

neighbors. The update of the velocity distribution function occurs by two steps: collision and propagation. In the collision step, the populations of molecules with various velocities at each lattice node are rearranged in a way that conserves mass and momentum and allows the velocity distribution function to relax toward a local equilibrium. In the propagation step, the fluid molecules travel to the neighboring lattice nodes based on the post-collision distribution. This method recovers the mean velocity and pressure fields associated with the incompressible Navier-Stokes equation in the limit of small Mach number, with a compressibility error that is proportional to the Mach number squared [76]. Here the Mach number is defined as the ratio of hydrodynamic velocity to the isothermal speed of sound. The isothermal speed of sound non-dimensionalized by the lattice spacing and time step is $c_s = 1/\sqrt{3}$. In our simulations the Mach number was always kept below 0.1. To achieve moderate values of Re without violating this constraint, we used a low viscosity and/or increased the sphere size. For Re ≤ 2 simulations we used a viscosity of $\eta = 6.0$; for higher Re simulations we used $\eta = 0.36$. The density of the lattice fluid is $\rho_f = 36$.

The lattice nodes in the particle suspension are marked as solid nodes if they lie within a specified input particle radius from the center of any of the particles and as fluid nodes otherwise. Fluid molecule populations that would propagate from a fluid to a solid node during the propagation step are bounced back with a small adjustment of the population density proportional to the sphere velocity. This adjustment is designed to enforce the no-slip boundary condition at boundary nodes located half-way along the links between the solid and fluid nodes [71, 72, 76]. This method leads to a representation of the boundary conditions on a smooth sphere with errors that are linear in the ratio of the lattice spacing to the sphere

Table 2.1: The effective sphere diameters used in this work and the corresponding input diameters and viscosities. The values are in terms of lattice units.

Effective diameter	Input diameter	Viscosity
5.84	5.84	6.0
11.68	11.66	6.0
5.84	5.38	0.36
11.68	11.18	0.36

diameter, owing to the roughness of the surface created by connecting the boundary nodes. The convergence can be improved to be approximately second order if one uses an effective hydrodynamic diameter to describe the rough sphere [76]. The hydrodynamic diameter, which depends only on the input diameter and viscosity, is determined by comparing the lattice-Boltzmann simulation results for the steady-state drag due to Stokes flow through a cubic array of spheres to the corresponding analytical results [113]. The input and effective diameters used in this work were determined by averaging simulation results for 5 to 7 randomly chosen positions of the particle relative to the lattice and are listed in Table 2.1. The larger input diameter 11.68 was used in test runs to confirm that the computations were well resolved. These calculations indicate that the simulation results reported in this work, which were obtained with an input diameter of 5.84, are within $\pm 3\%$ of the results obtained with an input diameter of 11.68.

From the momentum change of the fluid molecule populations that are bounced back from the surface of a sphere, we can calculate the stress on the particle surface. When spheres are very close to one another, the lattice resolution does not provide

an accurate calculation of the short-range hydrodynamic interaction. However, the flow in these thin lubrication gaps is dominated by viscosity even when $Re = O(1)$. Thus, we can use analytical results for the lubrication forces to describe these short-range interactions [76]. The lubrication force between two spheres colliding with a given velocity diverges as the separation between the spheres approaches zero. In a physical system, this divergence may be removed by particle roughness, non-continuum flows or a variety of other effects. In the simulation method, this effect can be treated approximately by allowing the lubrication force to remain a constant for separations smaller than a specified lubrication cut-off distance. The break-down of the lubrication force plays a critical role in the properties of sheared gas-solid suspensions where it limits the magnitude of the dissipation of particle kinetic energy [116]. However, in the present study of sedimenting particle-liquid suspensions, we found the results for the hindered settling velocity and suspension microstructure to be insensitive to the lubrication cut-off distance, which was then typically set to a value of 0.01 lattice spacings. The dynamics of the particle motion is determined by solving equations of linear and angular momentum conservation for each sphere using hydrodynamic forces and torques obtained by integrating the stresses determined from the lattice-Boltzmann simulation and lubrication corrections.

The simulations are carried out in cubic computational domains of size L^3 with periodic boundary conditions. Initially, N non-overlapping spheres of diameter d are randomly placed in the computational domain, giving a volume fraction of

$$\phi = \frac{N\pi}{6}\left(\frac{d}{L}\right)^3 . \tag{2.5}$$

By specifying the gravitational acceleration $\mathbf{g}$, each sphere is assigned a force

$$\mathbf{F} = \frac{\pi d^3}{6} \left(\rho_p - \rho_f\right) \mathbf{g} \ , \tag{2.6}$$

resulting from gravitational and buoyancy effects. A pressure gradient is applied to the fluid to ensure that the net volumetric flow rate of the suspension is zero. Initially, the spheres and the fluid are both at rest. Simulation results presented here are those obtained after the system reaches a statistical steady state.

Since the terminal velocity of the particle is not an input parameter to the simulation, the dimensionless parameter that can be most precisely controlled is the Archimedes number, defined as

$$\mathrm{Ar} = \frac{\rho_f \left(\rho_p - \rho_f\right) g d^3}{\eta^2}. \tag{2.7}$$

To determine the Reynolds number based on the terminal velocity that will be obtained for a given Archimedes number, we can make use of empirical relations for the drag coefficient for an isolated sphere [24]. The drag coefficient $\mathrm{C_D}$ defined as

$$\mathrm{C_D} = \frac{8 \left|\mathbf{F}\right|}{\rho_f u_t^2 \cdot \pi d^2} \tag{2.8}$$

is related to Re by

$$\mathrm{C_D} = \begin{cases} \frac{24}{\mathrm{Re}} \left[1 + 0.1315 \mathrm{Re}^{(0.82 - 0.05 \log_{10} \mathrm{Re})}\right] & , \quad 0.01 < \mathrm{Re} < 20 \\ \frac{24}{\mathrm{Re}} \left[1 + 0.1935 \mathrm{Re}^{0.6305}\right] & , \quad 20 < \mathrm{Re} < 260 \end{cases} . \tag{2.9}$$

Using Eqs. (2.7) and (2.8), one can obtain the following relationship between Ar, Re, and $\mathrm{C_D}$:

$$\mathrm{C_D} = \frac{4}{3} \frac{\mathrm{Ar}}{\mathrm{Re}^2} \ . \tag{2.10}$$

Thus, for given fluid and sphere (ρ_p, ρ_f, η, and d), Re is uniquely determined by

Ar through

$$\mathrm{Ar} = \begin{cases} 18\mathrm{Re}\left[1 + 0.1315\mathrm{Re}^{(0.82-0.05\log_{10}\mathrm{Re})}\right] & , \quad 0.01 < \mathrm{Re} < 20 \\ 18\mathrm{Re}\left[1 + 0.1935\mathrm{Re}^{0.6305}\right] & , \quad 20 < \mathrm{Re} < 260 \end{cases} . \qquad (2.11)$$

In this work, we chose the values of Ar based on Eq. (2.11) such that they give Re of approximately 1, 2, 5, 10, and 20 (Table 2.2).

2.3 Simulation Results

In this section, we first present the terminal velocities obtained from simulations and compare the results to the empirical correlation of drag coefficient C_D vs. Reynolds number Re for a sphere. We then use the terminal velocities to normalize the hindered settling velocities in suspensions and compare the normalized velocities to the power law formulae Eqs. (2.1) to (2.4). After that, we show the microstructure in the suspension for different Reynolds numbers and different volume fractions, in the forms of pair probability density distributions, radial distributions and order parameters. In the end, the mechanism behind the anisotropic microstructure and the relation between the microstructure and the anomalous behavior of the settling velocity in the dilute limit are discussed.

2.3.1 Terminal velocities

We first simulated the settling of a single sphere in a large cubic periodic domain to check whether the terminal velocities agree with the empirical Ar-Re relation Eq. (2.11). As the accuracy of our simulations can be affected by periodicity, we kept L/d sufficient large and used two different ratios — $L/d = 10.3$ and 20.6 — to assess the effect of L/d on the settling velocities. For every combination of Ar

(Re) and L/d, we kept the magnitude of the gravitational vector $\mathbf{g}$ but randomly changed its orientation 6-7 times. Meanwhile, the directions that are close to the primary lattice directions were avoided to ensure that the drag on the sphere is not affected by the wake of its own periodic image [62, 48, 49]. The terminal velocity reported is then the average of these 6-7 simulations with $\mathbf{g}$ oriented differently relative to the underlying lattice each time. This procedure increases the positions sampled by the sphere and minimizes the influence from the discrete lattice. The results from these single-sphere simulations are summarized in Table 2.2. The maximum deviation to Eq. (2.11) is $\sim 3\%$ and this only occurs for the highest Re. This agreement proves that our lattice-Boltzmann results are fairly accurate in this intermediate Reynolds number regime. Thus, we will use the simulated terminal velocities listed in Table 2.2 to normalize the hindered settling velocities.

2.3.2 Hindered settling velocities

Suppose the settling velocity of the ith sphere at time t is $\mathbf{u}_i(t)$ $(i = 1, 2, ..., N)$. The hindered settling velocity of the suspension $\mathbf{u}$ is the average of $\mathbf{u}_i(t)$ over i and t. The statistical accuracy of $\mathbf{u}$ depends on the number of particles, the number of realizations (independent runs) and the length of the steady states. In our simulations, the steady states usually have 150 - 600 dimensionless time units $t^* = tu_t/d$; in addition, we run 4-5 simulations for every combination of Re and ϕ, each time with a different initial configuration of particles. These procedures ensure that the statistical variations in the hindered-settling velocities are very small — less than 2% of the mean. The dimensionless settling velocity u^* is then obtained by normalizing $u = |\mathbf{u}|$ using the terminal velocities obtained from single particle simulations (Table 2.2).

Table 2.2: The Archimedes numbers used in this work and the terminal velocities and Reynolds numbers. The four columns in the middle are obtained from simulations and they are compared to the last column, which is obtained from Eq. (2.11). For Ar = 20.8 and Ar = 40.0, $\eta = 6.0$. For the higher Ar's, $\eta = 0.36$. In all simulations, the sphere size $d = 5.84$. Each entry in this table is the average of 6-7 runs. The standard deviations in u_t and Re, from run to run, are always less than 2% of the means.

Ar	$L/d = 10.3$		$L/d = 20.6$		Re From
	u_t	Re	u_t	Re	Eq. (2.11)
20.8	0.0277	0.97	0.0289	1.01	1.02
40.0	0.0503	1.75	0.0522	1.82	1.83
132	0.0082	4.79	0.0083	4.85	5.00
319	0.0163	9.52	0.0166	9.71	9.98
815	0.0325	19.0	0.0331	19.3	20.0

We first simulated a few suspensions with very small Reynolds numbers so that we can compare our settling velocities to the simulation results by Ladd [70] and Mo and Sangani [93]. In these low Re simulations, the Archimedes number Ar = 1.80, which yields Re = 0.10. When Re is very small, the range of the hydrodynamic interaction is very long and the finite size of the computational system can have a very significant effect on u. This finite system size effect can be corrected using a procedure outlined in the paper by Mo and Sangani [93]:

$$u(\infty) = u(N) + 1.7601 S_0 \frac{|\mathbf{F}|}{3\pi d\eta^*} \left(\frac{\phi}{N}\right)^{1/3} , \tag{2.12}$$

where S_0 is the structure factor [see Eq. (2.17)] in the suspension in the limit of zero wave number $\boldsymbol{\kappa} \to 0$, and η^* is the apparent viscosity

$$\frac{\eta}{\eta^*} = \frac{1}{1 + 2.5\phi} . \tag{2.13}$$

In low Re suspensions, the microstructure is very similar to that in a hard sphere suspension [70]. Thus, S_0 can be estimated from the Carnahan-Stirling approximation

$$S_0 = \frac{(1-\phi)^4}{1 + 4\phi + 4\phi^2 - 4\phi^3 + \phi^4} . \tag{2.14}$$

In Table 2.3, the normalized settling velocities, before and after correction using Eq. (2.12), are listed and they are compared to the results in [70] and [93], which were obtained using methods based on multi-pole expansion. The corrected results from our simulations are in good agreement with those from previous studies.

For suspensions with higher Reynolds numbers, we conducted test runs to assess the effect of system size on the settling velocities. We find that when Re $\geq$ 5, systems with $L/d = 10.3$ and $L/d = 15.4$ give nearly identical settling velocities [see Fig. (3d)]. In the simulations where Re = 1 and 2, however, we find that

Table 2.3: Settling velocities in Stokesian suspensions. Ar = 1.8 and Re = 0.10. The simulations are carried out in domains with $L/d = 10.4$ and $d = 5.84$. The viscosity of the fluid $\eta = 6.0$.

ϕ	0.05	0.10	0.25
Re	6.95×10^{-2}	5.42×10^{-2}	2.56×10^{-2}
u^*	0.69 ± 0.02	0.54 ± 0.01	0.256 ± 0.002
u^* (corrected)	0.77	0.55	0.265
Mo and Sangani [93]		0.52	0.20
Ladd [70]	0.76	0.53	0.24

L/d has a non-negligible effect on u^*. It turns out that when Re ≤ 2, we can still apply a procedure like Eq. (2.12) to correct the effect of L/d on u^*. The correction in Eq. (2.12) is based on two conditions: first, the drag of a periodic array is larger than the drag of a single sphere by a factor proportional to $1.7601\phi^{1/3}$ to the leading order [45, 113]; second, the microstructure of the suspension is similar to that of a hard sphere suspension. In Re ≤ 2 suspensions, we will see shortly that the first condition is approximately satisfied, and the second condition is not satisfied when $\phi > 0.10$.

When Re is finite, there is no theoretical prediction on how periodicity affects drag. However, we can simulate finite Re flows past simple cubic arrays of spheres and check whether the drag still agrees with the low Re scale of $1 - 1.7601\phi^{1/3}$ [45, 113]. In our simulations, the simple cubic arrays were constructed by placing a sphere in a cubic, periodic computational domain and a pressure gradient was applied to the fluid to drive the flow. We varied the size of the computational

domain and studied the drag as a function of the volume fraction. The results plotted in Fig. (2.1) show that when Re = 1, the drag of the array still agrees reasonably well with the low Re scale of $1-1.7601\phi^{1/3}$; when Re = 1.8, we start to see some deviations; finally, when Re = 5, it becomes quite clear that the low Re scale does not work any more. This test tells us that the first condition of Eq. (2.12) is approximately satisfied when Re ≤ 2 and is not satisfied when Re = 5. When it comes to the microstructure, as as we will find out later in this chapter, S_0 in finite Re suspensions can be quite different from that of a hard sphere suspension when $\phi \leq 0.10$. For example, when Re = 1 and $\phi = 0.01$, S_0 from simulation is 30% less than that calculated from Eq. (2.14). However, since S_0 appears as a simple proportionality constant, we can use the actual structure factor from simulations to replace the Carnanhan-Stirling formula Eq. (2.14) when $\phi \leq 0.10$. Although such a correction procedure is *ad hoc* in nature and cannot be regarded as precise, we believe that it covers the major source of errors that L/d may impose on u^*. As we will see in Fig. (2.2), it does improve the accuracy of u^* considerably when Re ≤ 2.

Fig. (2.2) shows the hindered settling velocities in Re ≤ 2 suspensions after corrections were applied. Compare the simulation results to the power laws with $k = 1$ [Eqs. (2.1) to (2.3)], and we can see that the agreement is very good in concentrated regime ($\phi > 0.10$), where the simulation data generally fall in between the two power laws — they are closer to Garside-Al-Dibouni curve when $\phi < 0.25$ and closer to Richardson-Zaki curve when $\phi > 0.25$. When $\phi \leq 0.10$, our simulation data are below both Richardson-Zaki and Garside-Al-Dibouni power laws, and it is apparent that a power law in the form of Eq. (2.4) with $k = 0.94$ gives slightly better fits. As ϕ approaches zero, u^* increases rapidly and deviates

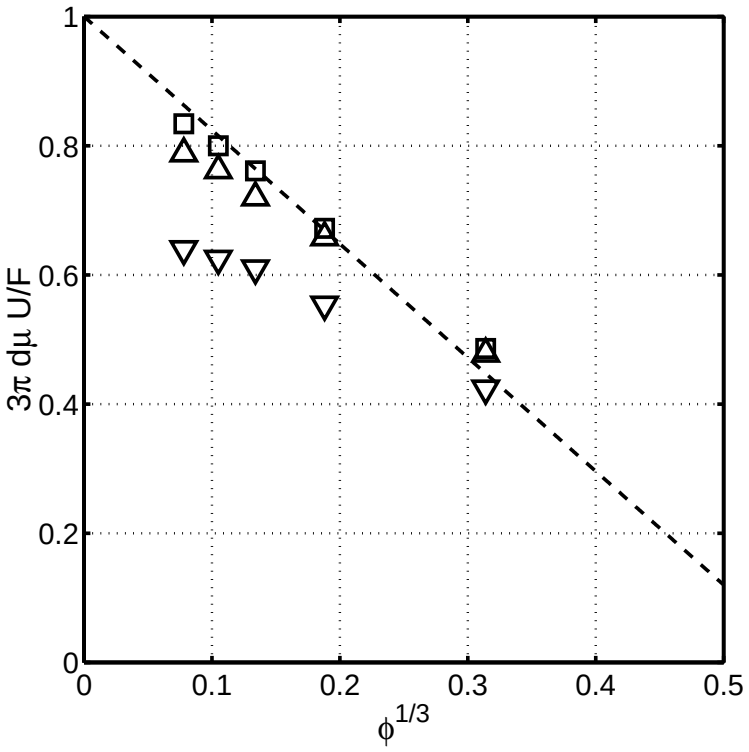

Figure 2.1: The drag on a simple cubic array of spheres when Re is finite. The drag F is normalized by the Stokes drag $3\pi d\mu U$ and is compared to Sangani and Acrivos's prediction (dashed line): $3\pi d\mu U/F = 1 - 1.7601\phi^{1/3}$ [113]. The squares represent Re = 1; the upward triangles represent Re = 1.8; the downward triangles represent Re = 5.

from the power-law fits. Batchelor has predicted that in a random dilute low Re suspension $u^* = 1 - 6.55\phi$ in the small ϕ limit [4]. This asymptote was included in Fig. (2.2) and it can be seen that the rapid increase of u^* in the dilute limit is pretty close to Batchelor's prediction.

As Re increases, the simulation data show more significant deviations from the power laws in the dilute regime, as one can readily observe in Fig. (2.3). Due to the rapid change of u^* in the dilute limit, both Richardson-Zaki [Eq. (2.2)] and Garside-Al-Dibouni [Eq. (2.3)] power laws with $k = 1$ overestimate u^*. In this case using a power law with prefactor $k < 1$ to fit u^* in concentrated regime is clearly a better choice than Richardson-Zaki and Garside-Al-Dibouni power laws, even though it does not take into account the anomalous rise in the dilute regime. In the next section we will see that the anomalous behavior of u^* in the dilute limit is associated with a change in the microstructure.

Assume that u^* follows a power-law in the form of Eq. (2.4), and we can plot $\log_{10} u^*$ against $\log_{10}(1-\phi)$. Such a plot is shown in Fig. (2.4) and one can see that the simulation data fit very well to straight lines, except some small deviations at the upper right corner, which correspond to the anomalous rise u^* in the dilute limit. One can use linear regression, then, to find out the power-law exponents n and prefactors k as functions of Re. The values of n and k that provide the best fits to our simulation data are listed in Table 2.4 and plotted in Fig. (2.5). Our values of n seem to agree more with the Richardson-Zaki formula [Eq. (2.2)] when Re ≤ 2 and more with the Garside-Al-Dibouni formula [Eq. (2.3)] when Re ≥ 5. Due to the variations in statistics and and experimental conditions, such as container size, secondary flow, instability, and polydispersity, it is difficult to judge from experimental data which formula gives more accurate prediction of n

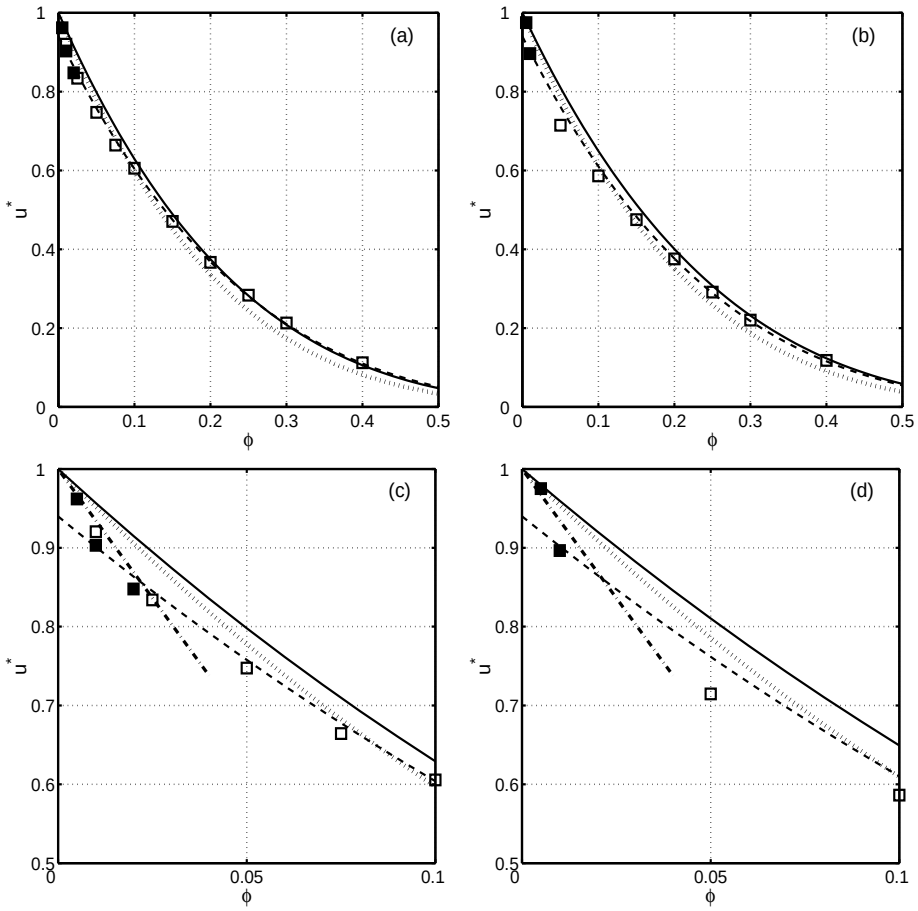

Figure 2.2: Hindered settling velocities in small Re (≤ 2) suspensions. (a): Ar = 20.8, Re $\sim$ 1; (b): Ar = 40.0, Re $\sim$ 2; (c) and (d) are the enlarged views of (a) and (b) in the dilute limit. The open symbols are obtained with $L/d = 10.3$ and the filled symbols are obtained with $L/d = 15.4$. The solid lines correspond to Richardson-Zaki power-law Eq. (2.2); the dotted lines correspond to Garside-Al-Dibouni law Eq. (2.3); the dashed lines are the best power-law fits using n and k from Table 2.4. The dash-dot lines correspond to Batchelor's asymptote of $u^* = 1 - 6.55\phi$ for dilute low Re suspensions [4].

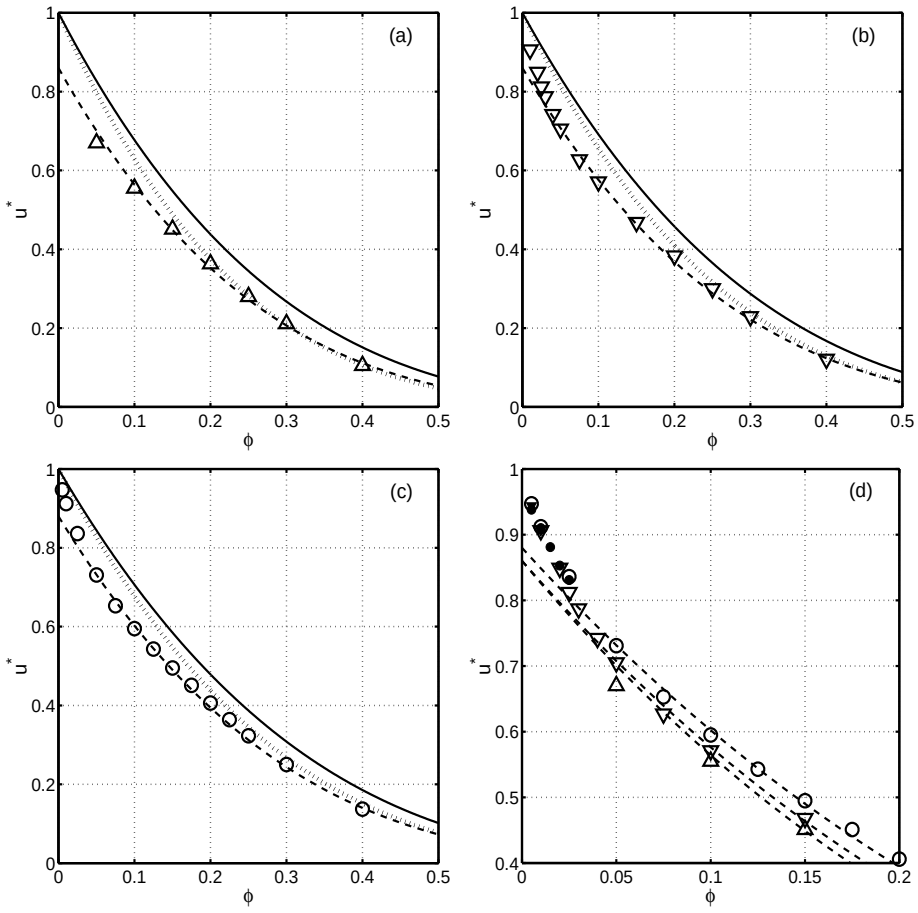

Figure 2.3: Hindered settling velocities in suspensions with higher Re (≥ 5). (a): Ar = 132 and Re = 5; (b): Ar = 319 and Re = 10; (c): Ar = 815 and Re = 20; (d): an enlarged view of the dilute regime. The definitions of the symbols follow those in Fig. (2.2). The open symbols are obtained from systems with $L/d = 10.3$ and filled symbols are obtained from systems with $L/d = 15.4$. The solid lines are the power laws using Eqs. (2.1) and (2.2); the dotted lines are the power laws based on Eqs. (2.1) and (2.3); the dashed lines are the best power-law fits in the form of Eq. (2.4) with $k \neq 1$.

in this particular range of Reynolds number $0 < \mathrm{Re} < 20$. As our simulations are not affected by any of the aforementioned uncontrollable conditions and there is no significant statistical variations in our simulation data, we think n from our simulations are perhaps more accurate and less ambiguous than those from experiments. In the range of $1 < \mathrm{Re} < 20$, our values of n can be represented by a quadratic polynomial

$$n = 4.23 - 0.0536\mathrm{Re} + 0.00111\mathrm{Re}^2 \tag{2.15}$$

with an R^2 value of 0.99. From Fig. (2.5), it seems that Eq. (2.2) is more accurate in the lower Re regime $\mathrm{Re} \leq 2$ and Eq. (2.3) is more accurate when $\mathrm{Re} \geq 20$. Unlike the power-law exponents n, k is not well documented in the literature. In a paper by Di Felice [31], based on his own experiments and a few previous studies, k is estimated to be 0.8 - 0.9. In our simulations, k is found to be 0.94 when Re is less than 2, and 0.86 - 0.88 when $\mathrm{Re} \geq 5$, which agrees with Di Felice's estimation. In our simulations, k decreases with increasing Re, because u^* deviates more from power laws in the dilute regime when Re increases.

2.3.3 Microstructure

The microstructure in a settling suspension is important and interesting because it describes how particles rearrange themselves in the sedimentation process. The microstructure in a suspension can be characterized by either the pair probability distribution function $\mathrm{P}(\mathbf{r})$

$$\mathrm{P}(\mathbf{r}) = \frac{L^3}{N^2} \left\langle \sum_i \sum_{j \neq i} \delta\left(\mathbf{r} - \mathbf{r}_{ij}\right) \right\rangle \ , \tag{2.16}$$

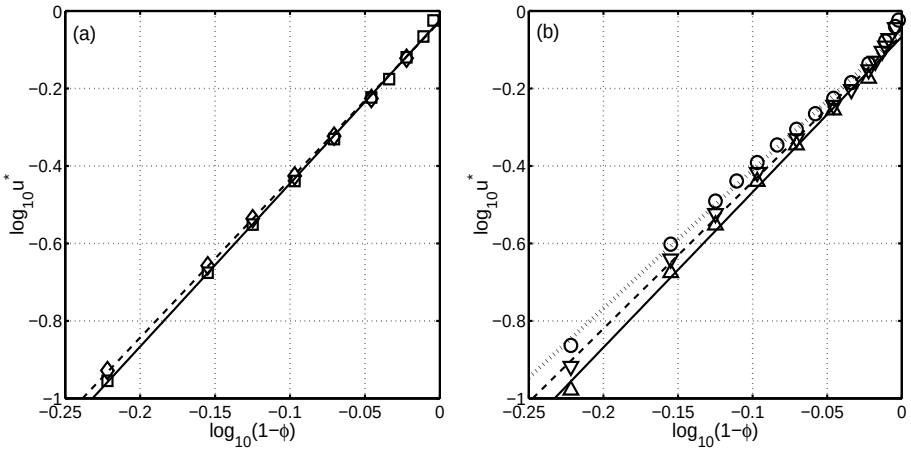

Figure 2.4: Hindered settling velocities as functions of ϕ on a logarithmic scale. (a): Re ≤ 2 [Ar = 20.8 ($\square$) and 40.0 ($\diamond$)]; (b): Re ≥ 5 [Ar = 132 ($\triangle$), 319 ($\triangledown$), and 815 ($\circ$)]. The lines are the best linear fits based on Table 2.4. All data are obtained from systems with $L/d = 10.3$.

Table 2.4: Power-law exponent n and prefactor k that provide the best fits to the settling velocities in concentrated suspensions ($\phi > 0.05$). The quality of the linear fits can be found from the R^2 values. The numbers after $\pm$ signs are the 95% confidence intervals of the fits. For comparison, we included the power-law exponents n_{RZ} calculated from Eq. (2.2) and n_{GA} calculated from Eq. (2.3).

Ar	n	k	R^2	n_{RZ}	n_{GA}
20.8	4.2 ± 0.1	0.94 ± 0.02	0.999	4.4	4.9
40.0	4.1 ± 0.1	0.94 ± 0.03	0.999	4.1	4.7
132	4.0 ± 0.3	0.86 ± 0.06	0.997	3.7	4.4
319	3.8 ± 0.2	0.86 ± 0.04	0.998	3.5	4.0
815	3.6 ± 0.1	0.88 ± 0.02	0.998	3.3	3.7

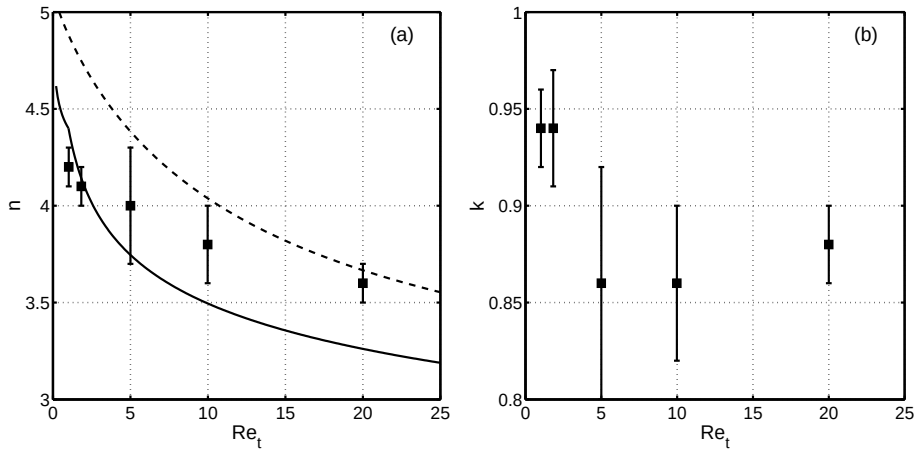

Figure 2.5: n and k in power laws obtained from simulations. (a): the power-law exponent n as a function of Re; (b): the prefactor k as a function of Re. The solid line in (a) corresponds to n_{RZ} based on Eq. (2.2) and the dashed line in (b) corresponds to n_{GA} based on Eq. (2.3).

or the structure factor $\mathrm{S}(\boldsymbol{\kappa})$, which is the Fourier transform of $\mathrm{P}(\mathbf{r})$

$$\mathrm{S}(\boldsymbol{\kappa}) = \frac{1}{N}\left\langle \sum_i \sum_j e^{-i\boldsymbol{\kappa}\cdot\mathbf{r}_{ij}} \right\rangle \ . \tag{2.17}$$

Experimental determination of microstructure in a settling suspension is very difficult. In colloidal suspensions, the structure factor can be obtained using light scattering techniques. In non-colloidal suspensions, the large size of the particles does not allow light scattering. Talini *et al.*[125] has proposed a scattering technique for non-colloidal suspensions based on NMR. However, it is only applicable to nearly stationary suspensions since the particles must not change their positions during an NMR scan. In principle, one can track the positions of spheres using imaging techniques and directly measure the pair distribution function. In practice, direct imaging of particles is limited to very dilute suspensions [120, 81] or suspensions confined in a narrow Hele-Shaw cell [111]. For dense suspensions,

it is possible to track a few marked particles in a index-matched suspension but impossible to track all particles. To our knowledge no one has ever attempted to measure $\mathrm{P}(\mathbf{r})$ experimentally in a three-dimensional sedimenting suspension.

In numerical simulations, it is easier to obtain the microstructural information because the positions of the particles can be tracked accurately at all times. However, to ensure that the microstructure obtained is accurate and meaningful, the suspensions of interest must contain sufficient number of particles and the simulations must be long enough such that we can average over many independent configurations. Due to the high computational cost involved, we only studied the microstructure in $\mathrm{Re} = 1$ and $\mathrm{Re} = 10$ suspensions in detail. For each Re, we calculated the pair probability distributions and structure factors at three volume fractions: $\phi = 0.01$ (dilute), 0.05 (intermediate), and 0.20 (concentrated).

The pair probability distributions were determined based on Eq. (2.16). For a suspension with N particles, there are $N(N-1)/2$ pairs that contribute to the statistics of $\mathrm{P}(\mathbf{r})$. For each combination of Re and ϕ, we ran 4-5 simulations with different initial particle configurations. After the sedimentation reaches steady state, we sample 300-500 configurations from each simulation. The time interval between samples is 1-2 in terms of the dimensionless time $t^* = tU_t/d$. By comparing the pair probabilities obtained from different simulations, we were able to ensure that our pair probability distributions are independent of initial condition and are statistically accurate. For all $\mathrm{P}(\mathbf{r})$ presented in this work, the standard deviation in $\mathrm{P}(\mathbf{r})$ is less than 10% of the mean value.

The structure factors were calculated based on Eq. (2.17) for wave vectors that are parallel ($\kappa_\parallel$) and perpendicular ($\kappa_\perp$) to the mean settling direction. The latter includes two orthogonal directions. We find that the two orthogonal directions

can be randomly picked and the structure factors in the two orthogonal directions are always identical within statistical fluctuations. This identity suggests that the microstructure is axisymmetric about the settling direction and there is no need to distinguish the two orthogonal directions. Therefore, we use $S_{\parallel}$ to represent the structure factor calculated using $\mathbf{k}$ that are parallel to the settling direction, and $S_{\perp}$ to collectively represent the structure factors in the two perpendicular directions.

The axisymmetry of the microstructure allows us to present $P(\mathbf{r})$ in a spherical coordinate system as a function of two variables: the center-to-center distance r, and the angle θ between the mean settling direction to the line connecting the centers of the two spheres. Fig. (2.6) shows $P(r, \theta)$ in $Re = 1$ suspensions. When the volume fraction is low ($\phi = 0.01$), there is a weak deficit region surrounding the center particle which extends a little further in the vertical direction ($\theta = 0$) than in the horizontal direction ($\theta = \pi/2$). As ϕ increases to 0.05, the deficit region almost disappears and the pair probability becomes fairly isotropic even though there is still a hint of deficit in the vertical direction. At the highest volume fraction ($\phi = 0.20$), high probability starts to appear at $r/d = 1$ due to steric repulsion, and the pair probability now becomes very isotropic. The anisotropy in the microstructure can also be seen in the structure factors, where $S_{\parallel}$ is slightly different from $S_{\perp}$ at low wave numbers.

In a hard sphere suspension, the particles do not interact with each other except when they collide. The suspension is thus totally isotropic and the microstructure should not depend on any particular direction. In this case the structure factor is governed by the Percus-Yevick equation and can be solved approximately [1]. We included these approximate solutions in the figures of structure factors to show the difference between the inertial settling suspensions and a hard sphere suspension.

Fig. (2.6) shows that the structure factors in Re = 1 suspensions is not very different from that of a hard sphere suspension, except for some deviation in the low wave number limit. Ladd [70] finds from simulations that the structure factors $S_{\parallel}$ and $S_{\perp}$ in low Re settling suspensions are very close to each other, and both are very close to that of a hard sphere suspension. In contrast, our $S_{\parallel}$ and $S_{\perp}$ are slightly different from each other, and both of them deviate from the isotropic structure factor at low wave numbers. This suggests that the finite inertia brings weak anisotropy into the suspension, and the anisotropy is most obvious at low volume fractions.

When Re = 10, the anisotropy in the suspension becomes much stronger. As Fig. (2.7) shows, at $\phi = 0.01$ and 0.05 the deficit region surrounding the center particle becomes more obvious, and it extends much further in the vertical direction. Moreover, the deficit in the pair probability is not evenly distributed: one can observe from Fig. (2.7a) and Fig. (2.7b) that there is more deficit in the horizontal direction than in the vertical direction. Perhaps the most interesting feature in the plots of $P(r, \theta)$ is the high pair probability peak in the horizontal direction. This high probability peak is located at $r/d \sim 2.5$ when $\phi = 0.01$, and $r/d \sim 2$ when $\phi = 0.05$. The combination of the deficit region and the peak suggests that at equilibrium state the spheres are more likely to separate and align horizontally as they settle. When $\phi = 0.20$, the anisotropy is not as significant as that at lower volume fractions. However, compared with Fig. (2.6c), Fig. (2.7c) is still noticeably more anisotropic.

The plots of structure factors tell a similar story. First of all, when Re = 10, $S_{\parallel}$ and $S_{\perp}$ are more different from each other, suggesting that there is more anisotropy in the suspension when Re is increased. Moreover, at wave lengths corresponding

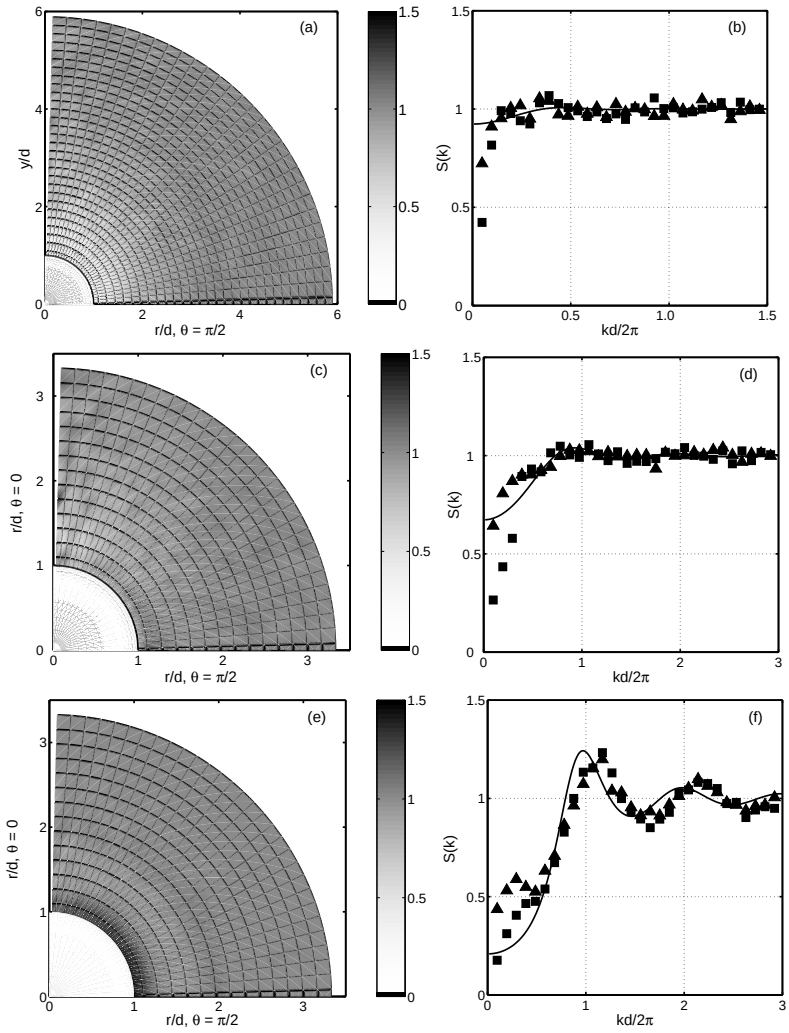

Figure 2.6: The pair probability density distributions and structure factors in suspensions with Re = 1. (a), (c), and (e) show the pair probability distributions in dilute ($\phi = 0.01$), intermediate ($\phi = 0.05$), and concentrated ($\phi = 0.20$) suspensions; (b), (d), and (f) show the corresponding structure factors. The triangles represent $S_{\parallel}(\kappa)$ and the squares represent $S_{\perp}(\kappa)$. The solid lines in the plots of structure factors are the solutions for hard sphere suspensions [1]. The simulations of dilute suspensions [(a) and (d)] were carried out in systems with $L/d = 15.4$. For the rest of the simulations $L/d = 10.3$.

to the positions of high probability regions, the structure factors deviate quite significantly from the hard sphere structure factor: when $\phi = 0.01$, there is a deviation at $kd/2\pi = 0.4$ that corresponds to the peak in $\mathrm{P}(r,\theta)$ at $r/d = 2.5$; when $\phi = 0.05$, a deviation occurs at $kd/2\pi = 0.5$, which corresponds to the peak in $\mathrm{P}(r,\theta)$ at $r/d = 2$.

From the pair probability distributions we can calculate the radial and angular distribution of particles. Here the radial distribution function $\mathrm{g}(r)$ is defined as the angular average of $\mathrm{P}(r,\theta)$

$$\mathrm{g}(r) = \frac{1}{2}\int_0^\pi \mathrm{P}(r,\theta)\sin\theta \mathrm{d}\theta \ . \tag{2.18}$$

The angular distribution, or the order parameter, is the expectation of the second order Legendre polynomial

$$\langle \mathrm{P}_2 \rangle(r) = \frac{\int_0^\pi \mathrm{P}(r,\theta)\mathrm{P}_2(\cos\theta)\sin\theta \mathrm{d}\theta}{\int_0^\pi \mathrm{P}(r,\theta)\sin\theta \mathrm{d}\theta} \tag{2.19}$$

where $\mathrm{P}_2(\cos\theta) = (3\cos^2\theta - 1)/2$. The radial distribution describes the probability of pair separations in a suspension; the angular distribution, on the other hand, measures the probability of pair orientations. These two quantities allow us to inspect the radial and angular distributions of particles separately and in a more quantitative way than what we can do with the pair probability $\mathrm{P}(r,\theta)$.

We calculated $\mathrm{g}(r)$ and $\langle \mathrm{P}_2 \rangle(r)$ for $\mathrm{Re} = 1$ and $\mathrm{Re} = 10$ suspensions and plotted the results in Fig. (2.8) and Fig. (2.9). These figures can be interpreted as follow. In a perfectly random suspension, $\mathrm{P}(r,\theta) = 1$. The corresponding equilibrium values of $\mathrm{g}(r)$ and $\langle \mathrm{P}_2 \rangle(r)$ are 1 and 0, respectively. Aside from the equilibrium value, $\langle \mathrm{P}_2 \rangle(r)$ also has two important limits: if all pairs are oriented to the direction of $\theta = 0$, $\langle \mathrm{P}_2 \rangle(r) = 1$; if all pairs are oriented to the direction of $\theta = \pi/2$, $\langle \mathrm{P}_2 \rangle(r) = -1/2$. Thus, a positive value of $\langle \mathrm{P}_2 \rangle(r)$ means that the pairs

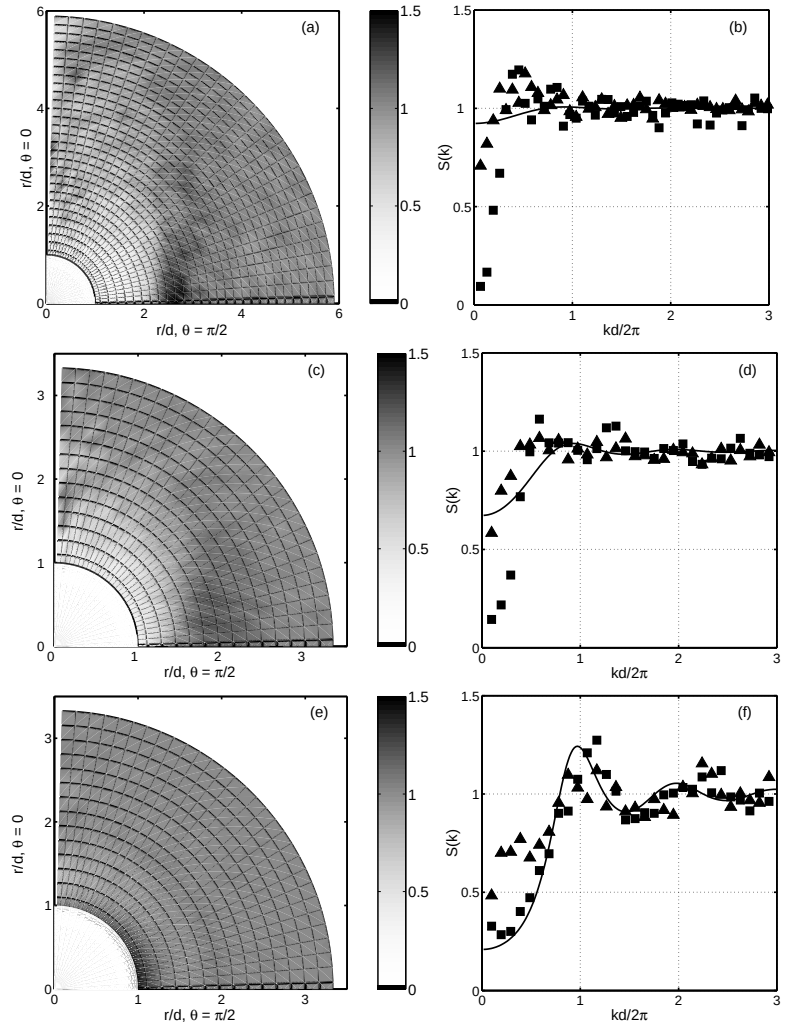

Figure 2.7: The pair probability density distributions and structure factors in suspensions with Re = 10. The volume fractions, from top to bottom, are $\phi = 0.01$, 0.05, and 0.20. For the definition of symbols and lines, as well as the information on the system size, see the caption of Fig. (2.6).

prefer to align in the vertical direction, and a negative value of $\langle P_2 \rangle(r)$ means that the pairs prefer to align in the horizontal direction.

The plots of $g(r)$ in Fig. (2.8) show that in dilute suspensions ($\phi = 0.01$) there is quite significant amount of deficit near the center particle. When Re = 1, this deficit extends to a distance of $r/d \sim 4$; when Re = 10, there is more deficit but it does not extend as far — only reaches $r/d \sim 2.5$. Note that this cut-off distance of the deficit happens to be the distance where the peak of high pair probability is found. Thus, we believe that the cut-off of the deficit in Re = 10 suspensions is due to the high pair probabilities on the side. With increasing volume fraction, the deficit in $g(r)$ decreases: in fact there is only very little deficit in Re = 1 suspensions. At the highest volume fraction ($\phi = 0.20$) $g(r)$ for both Re = 1 and Re = 10 become very much like that of a hard sphere suspension.

Fig. (2.9) shows the order parameters in the suspensions. When Re = 1, $\langle P_2 \rangle(r)$ shows only a small preference for horizontal alignment at $\phi = 0.01$, and this preference disappears fairly quickly with increasing ϕ. When Re = 10, $\langle P_2 \rangle(r)$ has a similar shape but quantitatively the deviations from the equilibrium value of zero become much stronger. The most significant deviation occurs at $\phi = 0.01$: $\langle P_2 \rangle(r)$ is positive when $r/d < 2$ and negative when $r/d > 2$, which means close pairs within $r/d < 2$ are more likely to align vertically and pairs that are further apart are more likely to align horizontally. This microstructure is consistent with the plot of $P(r, \theta)$ in Fig. (2.7), where there is a peak in the horizontal direction and an uneven distribution of deficits in the short range.

Finally, we would like to comment that the anisotropic microstructure observed in the simulations does not affect the homogeneity of the suspension on large length scales. It can be observed from Fig. (2.8) and Fig. (2.9) that both radial

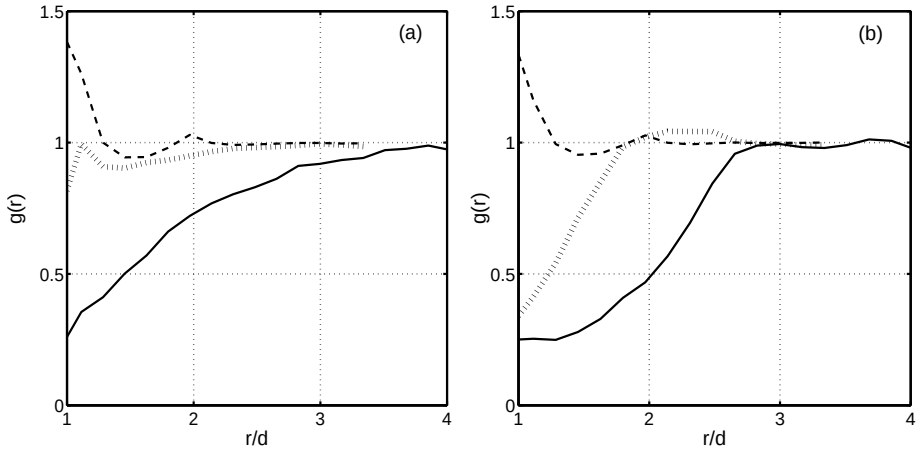

Figure 2.8: The radial distributions of settling spheres in suspensions with (a): Ar = 20.8 and Re = 1; (b): Ar = 319 and Re = 10. The solid lines represent $\phi = 0.01$; the dotted lines represent $\phi = 0.05$; and the dashed lines represent $\phi = 0.20$.

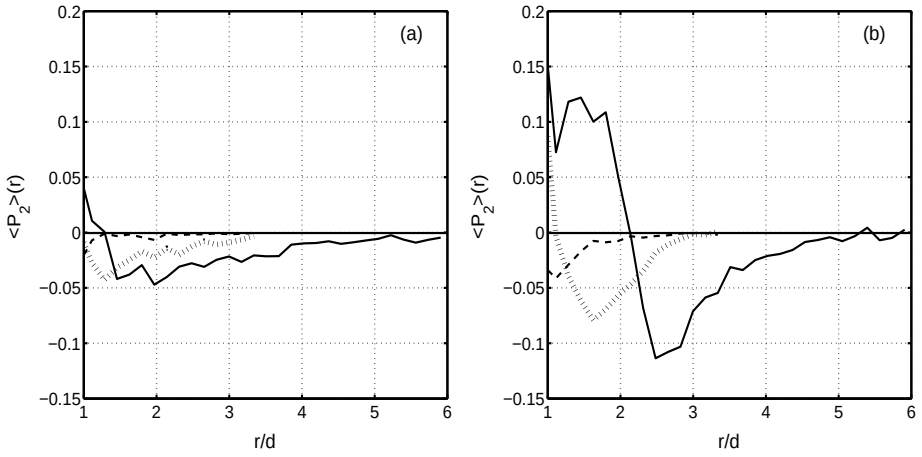

Figure 2.9: The order parameters in settling suspensions. (a): Ar = 20.8 and Re = 1; (b): Ar = 319 and Re = 10. The solid lines represent $\phi = 0.01$; the dotted lines represent $\phi = 0.05$; the dashed lines represent $\phi = 0.20$.

and angular distributions approach their equilibrium values at large r/d, which suggests that on large scales the suspensions are still homogeneous and random.

2.3.4 Discussions

We believe that the anisotropy in the microstructure in finite Re suspensions is driven by the wake interaction between pairs of settling spheres. When a solid sphere settles through the fluid with zero inertia, the flow field in front and behind the sphere is perfectly symmetric. When a solid sphere settles with finite Reynolds number, a velocity defect, or wake, is generated behind the sphere and the fore-aft symmetry of the flow field is broken. Due to the presence of wake, in a reference frame that moves with the sphere, one would observe incoming fluxes from behind. In order to conserve mass, the incoming flux must be redistributed to other directions. As a result, there are outgoing fluxes in front and on the sides to satisfy mass conservation [see Fig. (2.10)]. Due to this particular distribution of incoming and outgoing fluxes, if one sphere enters another sphere's wake, it experiences less drag and will therefore be drafted toward the leading sphere. According to the screening mechanism proposed by Koch [60], when a trailing sphere approaches the leading sphere in the wake, it experiences a lift force, which produces a horizontal motion that eventually pushes the trailing sphere out of the wake region. Another possibility is that when the inertial effect is strong, the lift force may not be sufficient to push the trailing particle away in a short interaction period. Then, there would be a collision and rotation, which is commonly referred to as the drafting-kissing-tumbling phenomena [37]. In both cases, once the trailing sphere moves out of the leading sphere's wake, the two spheres repel and separate from each other in the horizontal direction due to the outgoing fluxes [see Fig. (2.10)].

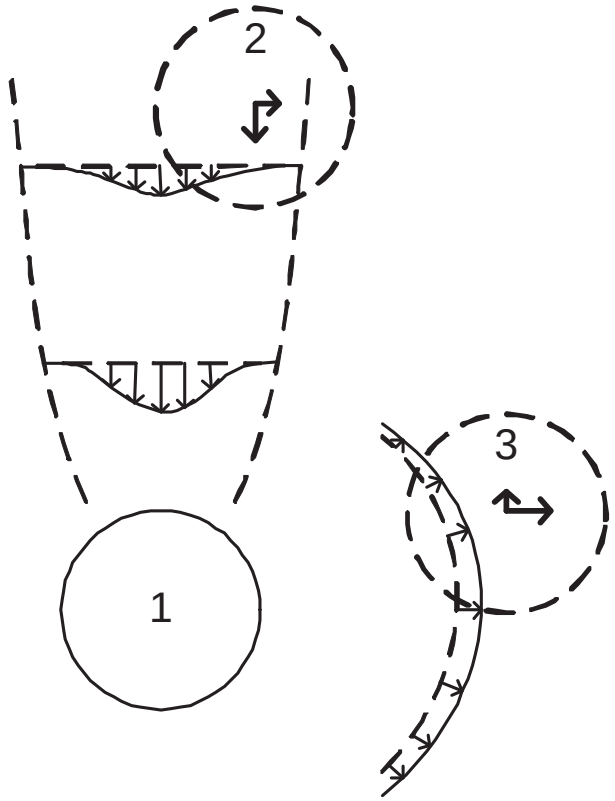

Figure 2.10: A qualitative view of the velocity field around a sphere settling with finite Re and the interaction between pairs of spheres. The velocity field shows the structure of a undisturbed and non-detached wake behind a sphere and the outgoing fluxes in other directions. A sphere located at 2 would be in the wake of 1 and thus would be attracted toward 1. At the same time the lift force, or the collision would push 2 away to the side. Finally, out of the wake region, a sphere located at 3 would be repelled.

In our simulations, we do observe pairs of spheres interacting with each other in a way consistent with the description above. One of such interactions is captured in a sequence of images shown in Fig. (2.11). In this sequence, Re = 20 so the spheres have relatively large inertia. Therefore, they touch and rotate as described by the drafting-kissing-tumbling mechanism. Before they touch, however, the trailing sphere also undergoes lateral motions. Thus, it is likely that both the lift force and drafting-kissing-tumbling are relevant in this pairwise interaction. After they touch and rotate, they separate in the horizontal direction as expected. Given enough time, this pairwise interaction eventually removes most spheres from each other's wake. Due to the confinement imposed by other spheres, the spheres that are pushed away cannot move apart forever. Thus, a peak is formed at a certain distance in the horizontal direction. In the end, a microstructure with a net deficit in the vertical direction and a peak in the horizontal direction is formed. The short-range uneven distribution of deficits, i.e. more deficit in the horizontal direction than in the vertical direction within the deficit region, which is most obvious in Fig. (2.7a) and Fig. (2.7b), we believe, is associated to the fact that the pair interaction is repulsive in horizontal direction and attractive in the vertical direction.

In our simulations we observed that the strength of anisotropy increases with increasing Reynolds number and decreases with increasing volume fraction. The dependence on Re is not difficult to understand because the anisotropy is driven by the wake interaction, the strength of which increases with Re. The dependence on ϕ, we think, is due to the competition between multi-body interaction and pair-wise interaction. The wake interaction that drives the anisotropy is pairwise in nature. In dilute suspensions, pairwise interactions dominate and the microstructure is very

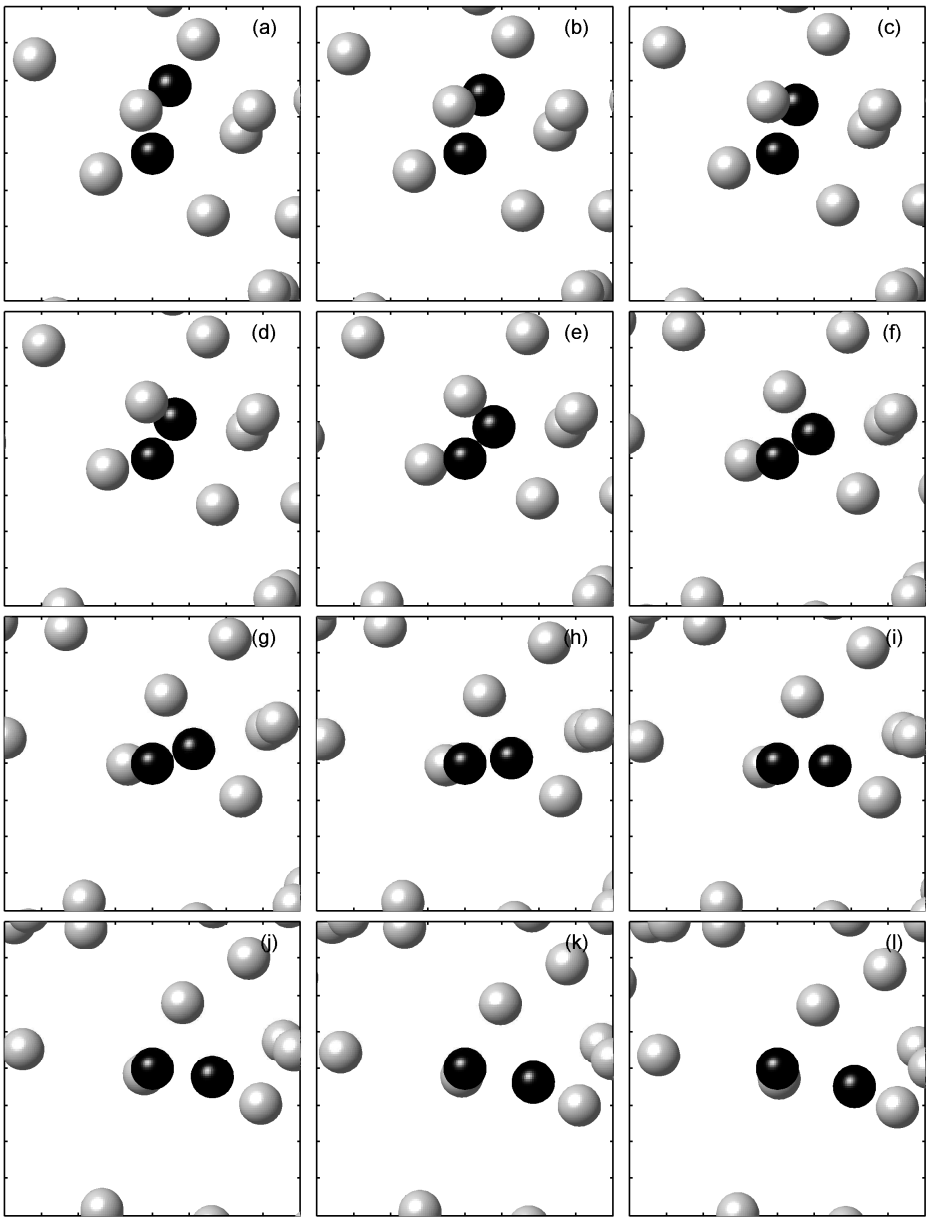

Figure 2.11: A sequence of images taken from a simulation showing the interaction between a pair of solid spheres. The pair of interest is painted into black and all the other spheres are in gray. The settling direction points downward. The reference frame moves with one of the spheres such that it always stays in the center. Simulation parameters: Ar = 815, Re = 20, $\phi = 0.01$, $L/d = 15.4$.

anisotropic; in concentrated suspensions, multi-body interactions become more important and they make the suspension more random and more chaotic. As a result, the microstructure becomes more isotropic than that in dilute suspensions.

Earlier in this chapter, we find that when Re $\leq$ 2, the settling velocity u^* follows power laws pretty well, with only a small deviation in the dilute limit; when Re $\geq$ 5, the deviation of u^* from power laws becomes more significant [see Fig. (2.2) through Fig. (2.4)]. We have reasons to believe that the anomalous behavior of u^* in the dilute regime is caused by the anisotropic microstructure found in dilute suspensions. As the pair probabilities indicate, in dilute suspensions most spheres are separated and aligned horizontally. This particular configuration has more hindering effect, because the spheres can not take advantage of each other's wake to enhance their settling velocities. As a result, in suspensions with anisotropic microstructure, u^* should decrease more rapidly with increasing ϕ than in suspensions with isotropic and random microstructure. This is exactly what we observed from the simulations: in the dilute limit, u^* decreases more rapidly with increasing ϕ than the power laws predict, and the anomalous behavior of u^* starts to develop near $\phi \sim 0.05$, contemporaneously with the volume fraction at which significant amount of anisotropy is seen in the microstructure. This finding also implies that the power-law behavior of u^* is associated with a random and isotropic suspension microstructure, which could be an interesting topic for further theoretical considerations.

2.4 Summary

In this chapter, using direct numerical simulation, we characterized the hindered settling velocities and microstructure in a suspension of monodisperse and non-colloidal spheres. We are particularly interested in the case where the spheres and the fluid have non-negligible inertia, because many of the properties of such suspensions are still not very well characterized and not very well understood to this date.

Our simulations show that the hindered settling velocities in concentrated suspensions $\phi > 0.05$ fit very well to power law functions of $1 - \phi$. In the dilute regime, however, there is an anomalous decrease of u^* with increasing ϕ, the slope of which is higher than predicted by the power laws. This anomalous behavior of u^* is not very obvious when $\mathrm{Re} \leq 2$ but becomes more significant at higher Reynolds numbers. As a result, the best power-law fits for the settling velocities in concentrated suspensions are in the form of $u/u_t = k\,(1-\phi)^n$. In our simulations, k is between 0.86 and 0.94 and it decreases with increasing Re. This anomalous behavior of u^* in dilute suspensions has been noted in the literature and our range of k is in good agreement with the range reported in a recent paper by Di Felice [31].

We believe that the anomalous behavior of u^* in the dilute regime is caused by a change in the microstructure. In the regime where u^* follows the power-law, the microstructure is close to that of the equilibrium distribution of hard spheres. In the dilute limit where a rapid decrease in u^* is observed, there is always significant amount of anisotropy in the microstructure. The anisotropic microstructure, driven by the inertial wake interaction between pairs of spheres, indicates that in dilute

suspensions, the spheres are more likely to separate and align in the horizontal direction as they settle. This spatial configuration of spheres increases the flow resistance and causes u^* to change more rapidly with ϕ than if the spheres were random distributed in the suspension.

Chapter 3

Velocity Fluctuations and Hydrodynamic Dispersion of Solid Particles in Finite Re Suspensions

3.1 Introduction

In a suspension of sedimenting solid particles, due to the hydrodynamic interactions, the settling velocity of the particles will fluctuate around the mean, and the particles will disperse away from their original positions. These fluctuations and dispersions of particles are fundamental properties of a suspension, because they play important roles in mixing and transport. In this chapter, we simulated the sedimentation of many monodisperse, spherical solid particles in cubic, periodic computational domains and characterized the velocity variance and hydrodynamic dispersion of particles as functions of domain size L, Reynolds number Re, and volume fraction ϕ. Here Re is defined as $\mathrm{Re} = \rho_f U_t d/\eta$, where U_t and d are the terminal velocity and the diameter of the particles, and ρ_f and η are the density and viscosity of the fluid. Re defined this way measures the level of fluid inertia on the length scale of particles. When Re is very small, it is well known that the long-range Stokes hydrodynamic interactions lead to an algebraic divergence of particles' velocity variance and diffusivity with increasing domain size [14, 70, 61, 74, 25]. Such a divergence, however, is contradictory to the experimen-

tal observations [43, 101, 100, 120, 42], thus is very surprising. Over the years, there has been many attempts to reconcile this conflict between the experiments and the theory and simulations [64, 73, 8, 75, 96, 98, 99]. In finite Re suspensions, the hydrodynamic interactions are more complex in nature due to the non-linear inertial effects, and very little is known on how such interactions affects the scaling behaviors of the velocity variance and particle diffusivity. Using direct numerical simulation, this study presents for the first time detailed scaling of the velocity variance and particle diffusivity in finite Re suspensions with the size of the computational domains. Our study encompasses a Reynolds numbers range of 1 - 10, and includes both dilute ($\phi = 0.01$) and moderately concentrated ($\phi = 0.20$) suspensions.

It is known that the microstructure of the suspension can have a significant effect on the scaling of the velocity variance. When Re is low, Calflisch and Luke [14] have shown that in an unbounded dilute suspension the velocity variance would diverge linearly with L/d if the particles are distributed randomly in space. This linear dependence of the velocity variance on L/d has been observed in several numerical studies conducted in periodic domains [70, 61, 74, 25]. It was suggested that a microstructural rearrangement may occur during the sedimentation process and it can modify the random distribution of particles and suppress the divergence of the velocity variance [64]. Recent numerical simulations [75, 98, 99] suggest that this microstructural change can come from the container walls, the presence of which can limit the large scale convective motions in the suspension and suppress the divergence of the velocity variance.

When Re is finite, with increasing inertia the velocity disturbance produced by a particle is no longer fore-aft symmetric. In the vertical (settling) direction,

due to the inertia of the fluid, the velocity disturbance produced by a test particle extends much further behind than in other directions. This asymmetry flow structure is often referred to as a wake, whose strength increases with increasing Re. In the horizontal direction, however, the velocity disturbance decays faster than that generated by a low Re solid particle thus has a reduced range. When Re is small but finite, based on a superposition of Oseen wakes, Koch [60] has shown that the vertical velocity variance in an unbounded, dilute, and random inertial suspension does not depend on L/d as strongly as in low Re suspensions — the velocity variance only diverges logarithmically with increasing L/d. This logarithmic dependence was verified in a numerical study by Climent and Maxey [25], where they used an approximate method and simulated the sedimentation of solid particles with Re $= 5$ and $\phi = 0.06$ in cubic periodic domains with size up to $L/d = 48$. It should be pointed out, though, that the distribution of particles in an inertial settling suspension is not a random one, because the inertial wake interactions between pairs of particles will produce a deficit of particle pairs in the vertical direction and an excess of particle pairs in the horizontal direction in Chapter 2. This deficit, as pointed out in [60], can screen the velocity disturbances at length scales beyond $O(d\phi^{-1})$ and keep the velocity variance finite [60].

Based on the above discussions, it is worthwhile to carry out a full numerical simulation to characterize the velocity variance such that we can verify whether a screening of velocity disturbances is occurring in finite Re suspensions. It is also of great interest to study the velocity variance in more concentrated suspensions, where the hydrodynamic interactions are expected to be more intense due to the close interactions among many solid bodies. Although the range of L/d in our simulations is still well below the scale of $O(d\phi^{-1})$, where it is expected that a total

screening would occur, we do find signs of partial screening in dilute suspensions that are consistent with Koch's prediction [60]. In addition, the horizontal velocity variance, and the velocity variance (vertical and horizontal) in more concentrated suspensions are also found to follow logarithmic scales.

We also characterized from simulations the scaling of the hydrodynamic diffusivity of particles with domain size L/d. In low Re suspensions, Koch [61] predicted that the diffusivity of point particles is proportional to the product of the root-mean-square (rms) velocity and the system size L. This theoretical prediction is supported by the numerical results by Ladd [70] and Cunha and coworkers [26, 27]. In this study, we find that the diffusivity of particles in finite Re suspensions are still proportional to the product of the rms velocity and the system size, which suggests that the hydrodynamic diffusion of particles in our simulations is still primarily controlled by large scale convective motions on the size of the domain.

Finally, it is worth mentioning that Parthasarathy and Faeth [105, 104] have measured from sedimentation experiments the velocity fluctuations of particles that are settling with finite Reynolds numbers. However, their results are heavily affected by the polydispersity and non-sphericity of the particles. As our simulations are free of these non-ideal effects, we can characterize the velocity variance and the diffusivity of the particles with less ambiguity.

This chapter is organized as follow: in Section 3.2, we give a brief description on the numerical method; in Section 3.3, we present the simulation results on the velocity variance and diffusivity of particles; in the last section, we summarize and discuss the major findings.

3.2 Numerical method

In this work we are using a lattice-Boltzmann method developed by Ladd [71, 72, 76] for solid particle suspensions. The lattice-Boltzmann method does not solve the Navier-Stokes equations directly. Instead, it solves the evolution of fluid molecular velocity distribution on a space-filling lattice using a simplified kinetic model. The molecular rules are designed in such a way that the moments of the molecular velocity distribution, which are equivalent to the macroscopic quantities such as density, momentum and stress, obey the Navier-Stokes equations. In our method, the spheres are implemented as groups of solid nodes on the lattice. The molecular interaction between a fluid node and a solid node is modelled to recover the no-slip boundary condition half way between the fluid node and the solid node. Therefore, the spheres in our method have staggered but well-defined no-slip boundaries. The method is first order accurate, and can be calibrated by using a hydrodynamic radius to give approximate second-order accuracy [76]. The accuracy increases with increasing lattice resolution. In our simulations, we used $d = 5.84$ in terms of the lattice spacing as the diameter of the particles. This resolution, compared with a higher lattice resolution ($d = 11.68$), is sufficiently accurate for the flow field around the particles and it allows us to simulate relatively large systems. It is not sufficient, however, to capture the lubrication interaction, which occurs in a very small gap between pairs of particles. To resolve this issue, the lubrication forces and torques are explicitly applied to close pairs of particles [98]. To avoid singularities, a cut-off distance can be set, within which no lubrication corrections are applied. If particles overcome lubrication forces and touch, elastic collisions are assumed. In most of our simulations we used a cut-off distance of 0.01 (lattice spacing),

and the choice of this cut-off distance, as long as it is reasonably small, does not have any noticeable effect on our results. Finally, we would like to emphasize that our computational grid is fixed but the particles move dynamically based on the instantaneous balance among weight, buoyancy, and the sum of fluid stresses on their surfaces.

The computational domains are cubic in shape and bounded by periodic boundaries from all directions. The system size L/d is varied between 10.3 and 25.7 when $\phi = 0.01$; and between 5.1 and 15.4 when $\phi = 0.20$. The particles are randomly placed in the domain and they have zero initial velocities. The particle density is twice of that of the fluid: $\rho_p/\rho_f = 2$. Due to this density difference, the particles accelerate in the gravity direction until the sedimentation reaches the steady state. A reverse pressure gradient is applied to the fluid to ensure that the net flow rate of the suspension is zero as if the sedimentation were carried out in a batch system with a bottom wall.

In this work, each data point shown is the average of 3-5 simulations with the same set of parameters but a different initial configuration of particles. The simulations are run for 1000-2000 dimensionless times $t^* = tU_t/d$, of which usually less than the initial 1/4 is spent on reaching the steady states and the final 1/2 is used for the statistics. Two examples of the velocity variance as functions of time are shown in Fig. (3.1).

3.3 Simulation results

In this section, we present the velocity variance and the hydrodynamic diffusivity of particles in settling suspensions as functions of system size L/d. The simulations

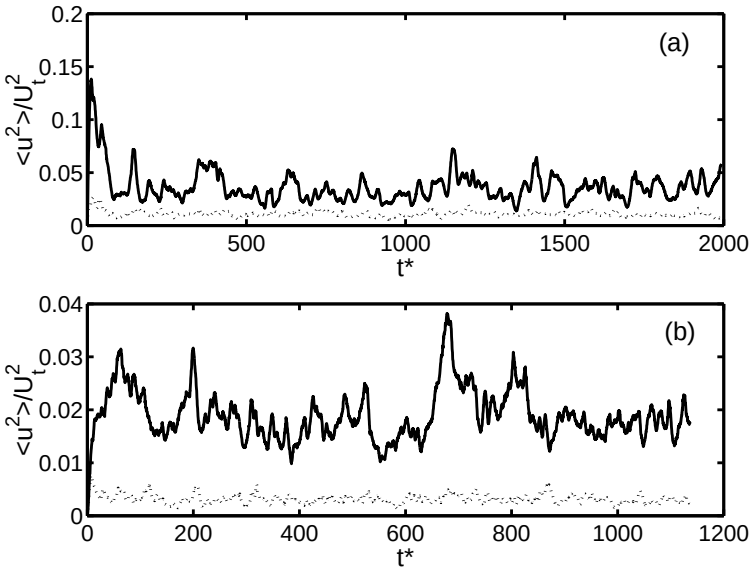

Figure 3.1: Two examples of the particle velocity variance obtained in the simulations. (a): $\phi = 0.01$ and $\mathrm{Re}_t = 1$; (b): $\phi = 0.01$ and $\mathrm{Re}_t = 10$. The solid line is the velocity variance in the vertical direction and the dotted line is the variance in the horizontal direction. In both simulations $L/d = 18.0$. The dimensionless time is defined as $t^* = tU_t/d$.

are divided into two groups: one with Re = 1 and another with Re = 10 to represent different levels of inertia. For each group, we simulated a dilute suspension with $\phi = 0.01$, and a concentrated suspension with $\phi = 0.20$.

3.3.1 Velocity variance

The velocity variance is important because it reflects the intensity of the fluctuating motions in a suspension. In earlier numerical studies [70, 25], the term "velocity variance" always refers to the velocity variance of particles. Here we would like to make a distinction between the particle velocity variance and the fluid velocity variance, because we find from our simulations that they are clearly different. They largely follow the same scale but the fluid velocity variance always has higher magnitudes. In this work, we report the velocity variance of both fluid and particles but only discuss in detail the velocity variance of particles.

Fig. (3.2) and Fig. (3.3) show the velocity variance of the fluid and that of the particles obtained from our simulations as functions of domain size L/d. When Re = 1, the simulation data in general fit quite well to logarithmic scales. It can be noticed, however, that in Fig. (3.2d) the fitting is not as good as the others. When Re = 1 and $\phi = 0.20$, the actual Reynolds number based on the average settling velocities is only about 0.4. Thus, inertial hydrodynamic interactions are fairly weak in this suspension and probably even weaker in the horizontal direction, which explains why the horizontal velocity variance of the fluid and the particles in Fig. (3.2d) do not follow logarithmic scales as well as in other figures but more like linear functions of L/d. As we increase the Reynolds number to 10, the velocity variance in Fig. (3.3) all fit very nicely to $\ln(L/d)$. Compare Fig. (3.2) and Fig. (3.3) and one can find that the magnitude of velocity variance is higher when Re = 1,

which agrees with the observation by Climent and Maxey [25] that there are more large scale convective motions present in lower Re suspensions.

Fig. (3.2) and Fig. (3.3) tell us that the logarithmic scaling proposed by Koch [60] is correct not only in dilute suspensions as it was originally proposed, but also in suspensions with much higher particle concentrations. Furthermore, the horizontal velocity variance also follows logarithmic scales, which suggests that part of the energy associated with the fluctuating motions in the vertical direction has been transferred to the horizontal direction by the non-linear hydrodynamic interactions. Koch [60] predicted that due to the deficit of particles in the vertical direction induced by the wake, the velocity variance would stop diverging when system becomes sufficiently large [$L/d \sim O(\phi^{-1})$]. Although we are not able to reach that size due to computational limitations, the velocity variance in Fig. (3.3a) does show very weak dependence on L/d in the largest systems we simulated.

Since the velocity variance in our simulations fit very well to logarithmic functions of L/d in the form of

$$\frac{\langle u^2 \rangle}{U_t^2} = A \ln(L/kd) \ , \tag{3.1}$$

it is natural to compare the coefficients A in our simulations to those predicted by the theory. Based on a random distribution of point particles and the superposition of their Oseen wakes, it was predicted [60] that the vertical particle velocity variance in dilute finite Re suspensions should follow

$$\frac{\langle u_\parallel^2 \rangle}{U_t^2} = \frac{3\phi}{4\pi^2 \mathrm{Re}} \left(\frac{F}{\eta U_t d} \right)^2 \left[\ln \left(\frac{L}{d} \right) + O(1) \right] \ . \tag{3.2}$$

In this equation, F is the forcing term which equals the weight of the particle less the buoyancy. The comparison in Table 3.1, however, reveals that A from the simulations are smaller than the theoretical predictions by 70% - 75%. This

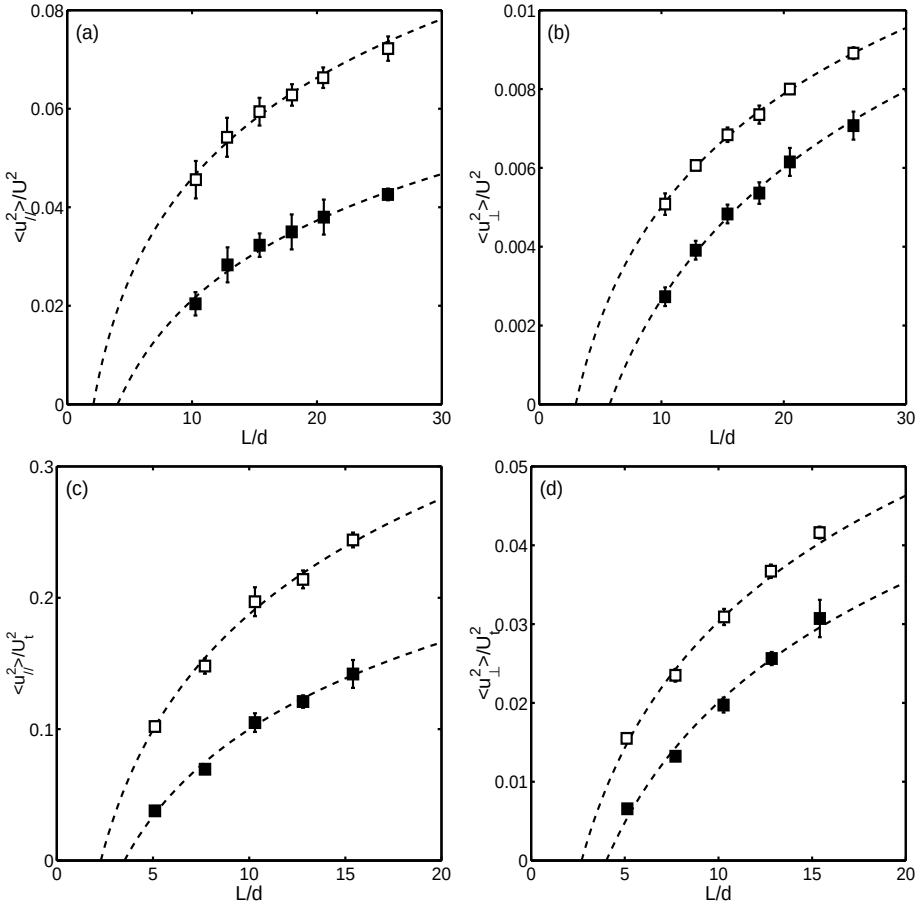

Figure 3.2: Particle and fluid velocity variance as functions of L/d (Re = 1). (a): $\phi = 0.01$, vertical direction; (b): $\phi = 0.01$, horizontal direction; (c): $\phi = 0.20$, vertical direction; (d): $\phi = 0.20$, horizontal direction. The filled symbols are the particle velocity variance and the open symbols are the fluid velocity variance. The error bars represent the standard deviations. The dashed lines are the best logarithmic fits in the form of Eq. (3.1).

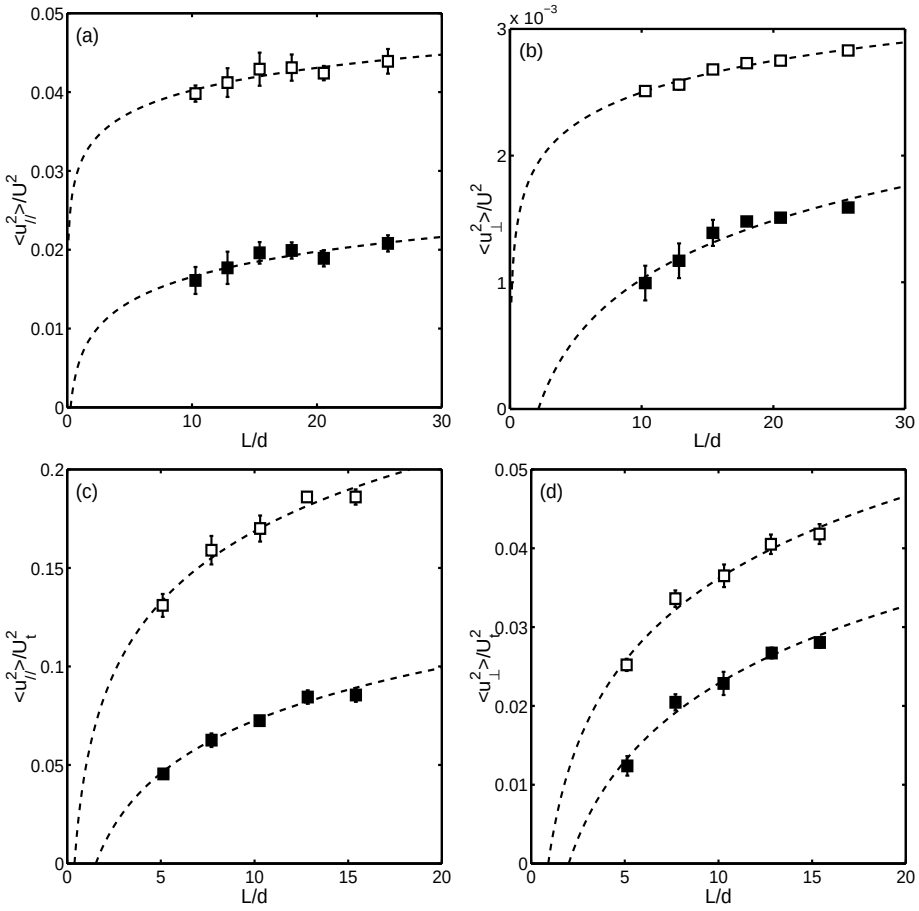

Figure 3.3: Particle and fluid velocity variance as functions of L/d (Re = 10). (a): $\phi = 0.01$, vertical direction; (b): $\phi = 0.01$, horizontal direction; (c): $\phi = 0.20$, vertical direction; (d): $\phi = 0.20$, horizontal direction. The filled symbols are the particle velocity variance and the open symbols are the fluid velocity variance. The error bars represent the standard deviations. The dashed lines are the best logarithmic fits in the form of Eq. (3.1).

Table 3.1: The values of A and k in Eq. (3.1) that provide the best fits to the particle velocity variance. The numbers after "$\parallel$" symbol are for the vertical variance and the numbers after "$\perp$" are for the horizontal variance. The coefficients from Eq. (3.2) are included for comparison.

		A (simulation)	k (simulation)	A [Eq. (3.2)]
$\mathrm{Re} = 1,$	$\parallel$	2.5×10^{-2}	4.4	8.7×10^{-2}
$\phi = 0.01$	$\perp$	4.8×10^{-3}	5.5	
$\mathrm{Re} = 10,$	$\parallel$	4.6×10^{-3}	0.27	1.9×10^{-2}
$\phi = 0.01$	$\perp$	6.7×10^{-4}	2.2	
$\mathrm{Re} = 1,$	$\parallel$	9.6×10^{-2}	3.5	
$\phi = 0.20$	$\perp$	2.2×10^{-2}	4.0	
$\mathrm{Re} = 10,$	$\parallel$	3.9×10^{-2}	1.5	
$\phi = 0.20$	$\perp$	1.5×10^{-2}	1.9	

rather large difference in A between the simulations and the theory, we think, is primarily because the particles are not randomly distributed in the suspension. A study of the suspension microstructure shows that there is a net deficit of particles in the wake region. This deficit, as predicted by the theory [60], partially screens the velocity disturbance in the wake and reduces the growth rate of the velocity variance with increasing L/d.

The microstructure in a suspension can be characterized by the pair probability density distribution function $\mathrm{P}(\mathbf{r})$, defined as

$$\mathrm{P}(\mathbf{r}) = \frac{L^3}{N^2} \left\langle \sum_i \sum_{j \neq i} \delta\left(\mathbf{r} - \mathbf{r}_{ij}\right) \right\rangle \ . \tag{3.3}$$

In a settling suspension, $\mathrm{P}(\mathbf{r})$ is axisymmetric about the settling direction and thus

can be reduced to a function of two variables: the pair separation r, and the angle θ from the settling direction to the orientation vector connecting the pairs. When $\theta = 0$ the pair is aligned in the vertical (settling) direction; when $\theta = \pi/2$, the pair is aligned in the horizontal direction. $\mathrm{P}(r, \theta)$ has an equilibrium value of 1, which corresponds to a random distribution of particle pairs. $\mathrm{P}(r, \theta) > 1$ means an excess of particle pairs and $\mathrm{P}(r, \theta) < 1$ means a deficit.

We calculated the pair probability distributions in our dilute suspensions and find that these dilute suspensions are not random at all. As shown in Fig. (3.4), there is quite appreciable amount of deficit near the center particle, and it extends much further in the vertical direction than in the horizontal direction when Re is high. This deficit is produced by the inertial wake interaction between pairs of particles: when one particle settles in another particle's wake, it experiences less drag, and thus will be attracted toward the leading particle; at the same time, it experiences a lift force due to the velocity gradient present in the wake and will be gradually pushed to the side [60]; when the attraction finally brings them together, they rotate and change orientation, then separate from each other in the horizontal direction [37]. Due to this interaction, at steady state, a microstructure with a deficit of pairs in the horizontal direction and an excess of pairs in the horizontal direction is developed.

This deficit in the pair probability distribution has a very important effect on the particle velocity variance. As we have emphasized, Eq. (3.2) is derived by superposing the Oseen velocity disturbances in a suspension, assuming that the pair probability distribution is uniform everywhere in the suspension. When the particle distribution in a suspension is non-random, in principle one must carry out a conditional average using the non-uniform pair probability distribution $\mathrm{P}(r, \theta)$

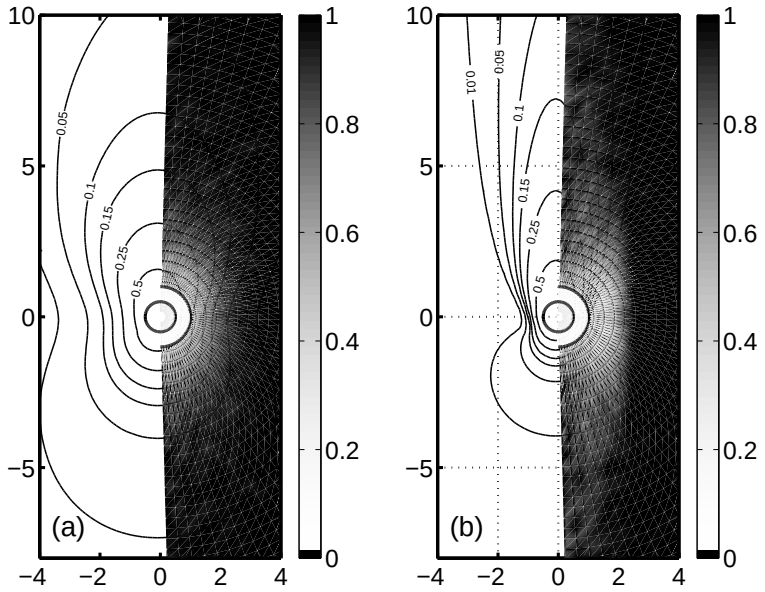

Figure 3.4: Contours of the velocity disturbance in the settling direction $u_{\parallel}/U_t$ of a single particle and the pair probability density distributions in dilute suspensions with $\phi = 0.01$. (a): Re $= 1$; (b): Re $= 10$. In each picture, the velocity disturbance is shown on the left and the pair probability density distribution is shown on the right. The numbers in the velocity disturbance plots are the size of the disturbances (in the settling direction) relative to the terminal velocities. The color scale of the pair probabilities is adjusted such that regions with $\mathrm{P}(r, \theta) \geq 1$ are painted in black and various shades of gray represents the deficit regions with $\mathrm{P}(r, \theta) < 1$.

as the weight to find out the velocity variance. Such calculation, however, is not trivial, because one must know accurately the value of $\mathrm{P}(r,\theta)$ at all locations, including the far-field, where $\mathrm{P}(r,\theta)$ are not very different from a uniform distribution, and the determination of $\mathrm{P}(r,\theta)$ may be affected by the periodicity of the system. Nevertheless, even without a detailed calculation, by looking at the distribution of deficits in $\mathrm{P}(r,\theta)$ and the velocity disturbance field caused by an isolated particle [Fig. (3.4)], one can tell that the velocity disturbances in the deficit regions are going to be screened, at least partially, and the velocity variance from the conditional average is going to be reduced.

The relation between a net deficit of particles in the neighborhood of the center particle and resulting screening of the velocity disturbance has also been discussed in the paper by Koch and Shaqfeh [64], where it was predicted that if the deficit in the pair probability distribution $\mathrm{P}(r,\theta)$, evaluated by the integral

$$I(R) = 2\pi n \int_{d/2<r<R} [\mathrm{P}(r,\theta) - 1]\, r^2 \sin\theta \mathrm{d}\theta \mathrm{d}r \ , \tag{3.4}$$

reaches -1 on an intermediate length scale $R < L/2$ that is independent of the choice of L, the divergence of the velocity variance with increasing L can be suppressed. We calculated $I(R)$ in dilute suspensions and plotted the results in Fig. (3.5), where it can be observed that $I(R)$ decreases fairly rapidly toward -1 with increasing R. The decrease in $I(R)$ is nearly independent of L until $I(R)$ reaches about -0.7. After that, the choice of L starts to affect the behavior of $I(R)$, which suggests that what is occurring in our simulations is a partial screening of the velocity disturbances. This partial screening makes the velocity variance diverge logarithmically with L/d. The rates of the divergence, however, are smaller than the theoretical predictions.

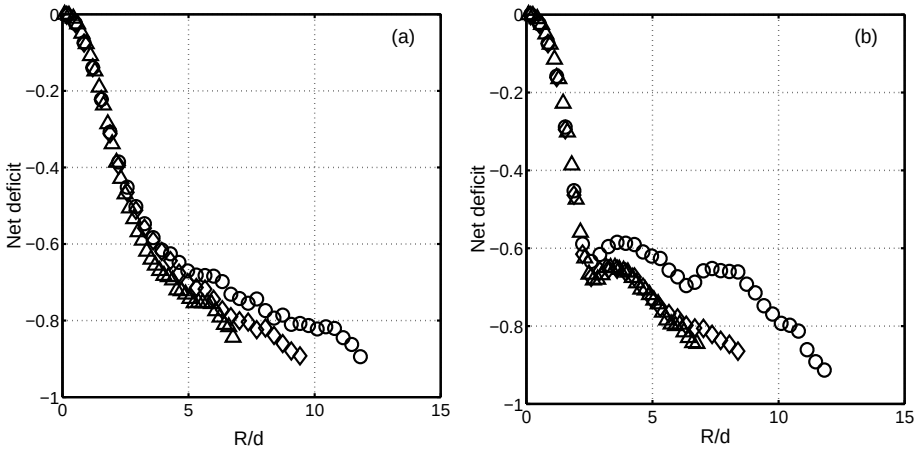

Figure 3.5: The deficits of particles in $\phi = 0.01$ suspensions as functions of R. These deficits are evaluated from Eq. (3.4). (a): Re = 1; (b): Re = 10. The triangles, diamonds, and circles represent results from systems with $L/d = 15.4$, 20.5 and 25.7, respectively.

In the sedimentation process, the velocity fluctuations are often anisotropic in the sense that the fluctuation in the vertical direction is usually higher than that in the horizontal direction. The ratio of the root-mean-square (rms) velocities $\Delta u_{\parallel}^*/\Delta u_{\perp}^*$ is a measure of this anisotropy, where $\Delta u_{\parallel}^*$ and $\Delta u_{\perp}^*$ are defined as

$$\begin{aligned} \Delta u_{\parallel}^* &= \langle u_{\parallel}^2 \rangle^{1/2}/U_t \\ \Delta u_{\perp}^* &= \langle u_{\perp}^2 \rangle^{1/2}/U_t \ . \end{aligned} \tag{3.5}$$

In Table 3.2, we listed the ratios of $\Delta u_{\parallel}^*/\Delta u_{\perp}^*$ in our simulations as functions of Re and ϕ. The highest ratio of $\Delta u_{\parallel}^*/\Delta u_{\perp}^*$ occurs at Re = 10 and $\phi = 0.01$. From studies on the suspension microstructure (Chapter 2), it has been found out that this combination of Re and ϕ also produces the strongest pair-wise inertial wake interaction, and the most anisotropic pair probability distributions as shown in

Fig. (3.4). It is very likely, then, that the high ratio of rms velocities at Re = 10 and $\phi = 0.01$ is related to the anisotropy in the microstructure. Table 3.2 also shows a trend that the anisotropy in the rms velocities decreases with increasing ϕ. This trend, we believe, is the result of the more random and chaotic multi-body interactions present in high particle concentration suspensions.

3.3.2 Hydrodynamic dispersion

The hydrodynamic dispersion in particle suspensions is characterized by the hydrodynamic diffusivity of particles, which can be calculated either from the rate of mean square displacements

$$\mathbf{D} = \lim_{t\to\infty} \frac{1}{2t} \langle [\mathbf{R}(t) - \mathbf{R}(0) - \langle \mathbf{U} \rangle t]^2 \rangle \tag{3.6}$$

or from the autocorrelations of particle velocities

$$\mathbf{D} = \int_0^\infty \langle \mathbf{u}(t)\mathbf{u}(0) \rangle \mathrm{d}t \ . \tag{3.7}$$

In Eq. (3.6), the diffusivity tensor $\mathbf{D}$ is calculated from the displacements of particles relative to the mean motion prescribed by $\langle \mathbf{U} \rangle t$; in Eq. (3.7), $\mathbf{D}$ is calculated using the fluctuating velocities of particles $\mathbf{u} = \mathbf{U} - \langle \mathbf{U} \rangle$. We used both Eqs. (3.6) and (3.7) to calculate $\mathbf{D}$ and the results are very similar: $\mathbf{D}$ obtained from our simulations are tensors whose diagonal elements are clearly dominating the non-diagonal ones. $\mathbf{D}$ can thus be characterized by $D_\parallel$, the diagonal element in the settling direction, and $D_\perp$, the diagonal elements in the horizontal directions, which, due to the axisymmetry of the suspension, are always identical to each other. Just as the rms velocities of particles, the diffusivity of particles is also very anisotropic. We will find out later that the values of $D_\parallel$ are usually much higher than the values of $D_\perp$.

Fig. (3.6) shows an example of the normalized particle velocity autocorrelations $\mathbf{C}(t) = \langle \mathbf{u}(t)\mathbf{u}(0)\rangle / \langle u^2 \rangle$, and an example of the mean square displacements $\langle [\mathbf{R}(t) - \mathbf{R}(0) - \langle \mathbf{U} \rangle t]^2 \rangle$ as functions of time. As discussed, these tensors can be represented by their diagonal elements in the vertical and horizontal directions. From the velocity autocorrelation functions, we observed that it always takes longer time for $C_{\parallel}$ to relax to zero than for $C_{\perp}$. Moreover, this relaxation time increases with increasing Re but decreases with increasing ϕ. The dispersive behavior of the particles show that at short time scales, the mean square displacements are quadratic functions of t^*, which simply means that the particle displacement is directly proportional to time by its velocity. With increasing t^*, the mean square displacements undergo a transition and become eventually linearly correlated with t^*, which proves that over long times the hydrodynamic dispersion of particles is a random-walk process.

Fig. (3.7) and Fig. (3.8) show the normalized particle diffusivities $D^*_{\parallel} = D_{\parallel}/U_t d$ and $D^*_{\perp} = D_{\perp}/U_t d$ as functions of L/d. It can be observed that the diffusivities increase nearly monotonically with increasing L/d, following scales that are clearly stronger than the logarithmic scales followed by the velocity variance. A comparison between Fig. (3.7) and Fig. (3.8) shows that the magnitude of the particle diffusivity decreases with increasing Re. This trend, being consistent with that of the velocity variance, is not surprising since both the fluctuating motions of the particles and the dispersion of them are primarily due to the large scale convective motions that are more pronounced in lower Re suspensions. Finally, these figures show that between $\phi = 0.01$ and $\phi = 0.20$ suspensions, $D_{\parallel}$ have similar magnitudes but $D_{\perp}$ is clearly higher when $\phi = 0.20$. It is generally expected that the hydrodynamic diffusivity of particles would grow with increasing ϕ in dilute

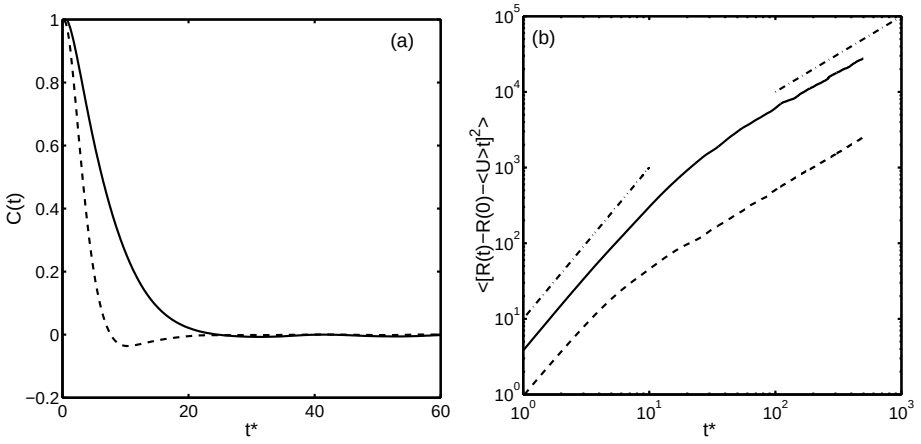

Figure 3.6: Examples of the autocorrelation of particle velocities and the mean square displacements as functions of time. (a): vertical and horizontal velocity autocorrelations; (b): vertical and horizontal mean square displacements. The solid lines represent the correlations/displacements in the vertical direction and the dashed lines represent those in the horizontal direction. In (b) we also included dash-dot lines to represent slopes of 1 and 2. In both figures Re = 1 and $\phi = 0.20$. The system size $L/d = 12.8$.

suspensions, reach a maximum at some intermediate concentration, and decrease with further increase of ϕ due to the constraint imposed by neighbor particles. Our results indicate that the maximum of $D_{\parallel}$ probably occurs between $\phi = 0.01$ and $\phi = 0.20$. For $D_{\perp}$, however, one would need more data points between $\phi = 0.01$ and $\phi = 0.20$ to be able to determine the trend.

In low Re suspensions, Koch [61] predicts that the hydrodynamic diffusivity of point particles is proportional to the product of the rms velocity and the system size. Since the rms velocity is proportional to $(L/d)^{1/2}$ in low Re suspensions, the diffusivity of particles should be proportional to $(L/d)^{3/2}$. To check whether the diffusivity in finite Re suspensions is still proportional to the product of the rms velocity and the system size, we plotted the values of $D/\left(\langle u^2\rangle^{1/2}L\right)$ in Fig. (3.9). It can be observed that at large L/d $D/\left(\langle u^2\rangle^{1/2}L\right)$ approach constant values, which indicates that it is still valid to write the diffusivity as the product of the rms velocity and the system size. Now that the rms velocity is proportional to $[\ln(L/d)]^{1/2}$ instead of $(L/d)^{1/2}$, the dependence of the particle diffusivity on L/d is weaker than $(L/d)^{3/2}$ but still marginally stronger than the linear scale of L/d.

Finally, we would like to present the ratios of $D_{\parallel}/D_{\perp}$ in our simulations, which represents the anisotropy in the dispersion process. The ratios of $D_{\parallel}/D_{\perp}$ are listed in Table 3.2 and they are all higher than the ratios of rms velocities, which means that the hydrodynamic diffusivities of particles are more anisotropic than the fluctuating velocities. The highest ratio of $D_{\parallel}/D_{\perp}$, again, occurs at Re = 10 and $\phi = 0.01$ thus is likely to be the result of the anisotropic microstructure. In low Re suspensions, extremely high values of $D_{\parallel}/D_{\perp}$ reaching $O(100)$ can occur in dilute suspensions due to the cubic shape of the computational domain, where it is pointed out that a particle does not have enough time to sample enough horizontal

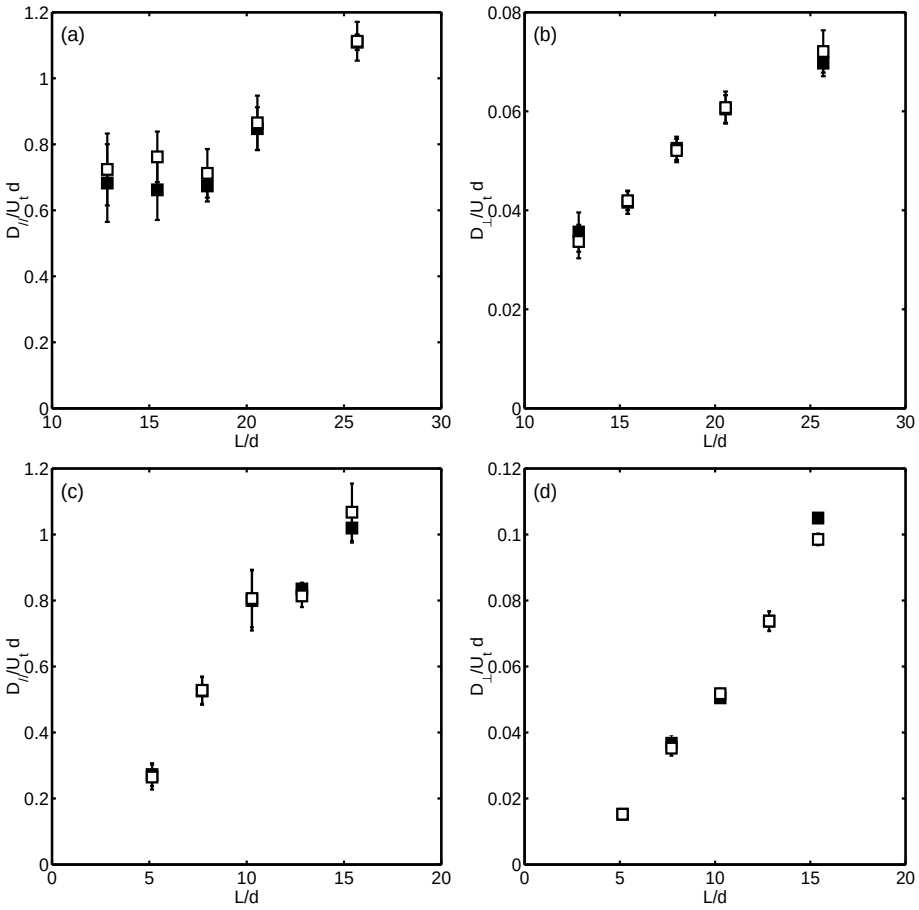

Figure 3.7: Normalized vertical and horizontal particle diffusivities in Re = 1 suspensions. (a) and (b) show $D^*_{\parallel}$ and $D^*_{\perp}$ in dilute suspensions where $\phi = 0.01$; (c) and (d) show $D^*_{\parallel}$ and $D^*_{\perp}$ in concentrated suspensions where $\phi = 0.20$. The filled symbols and open symbols represent the results from mean square displacements [Eq. (3.6)] and autocorrelations [Eq. (3.7)], respectively. The error bars are the standard deviations from 3-5 runs.

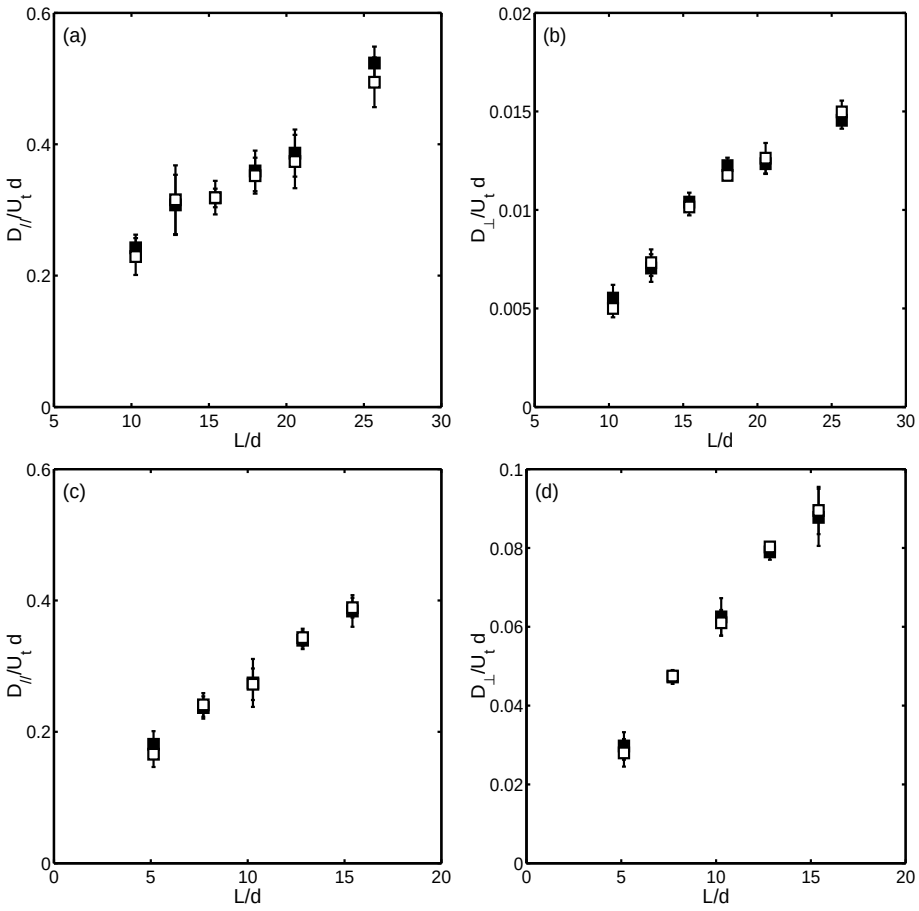

Figure 3.8: Normalized vertical and horizontal particle diffusivities in Re = 10 suspensions. (a) and (b) are for $\phi = 0.01$; (c) and (d) are for $\phi = 0.20$. The filled symbols and open symbols represent the results from mean square displacements [Eq. (3.6)] and autocorrelations [Eq. (3.7)], respectively. The error bars are the standard deviations from 3-5 runs.

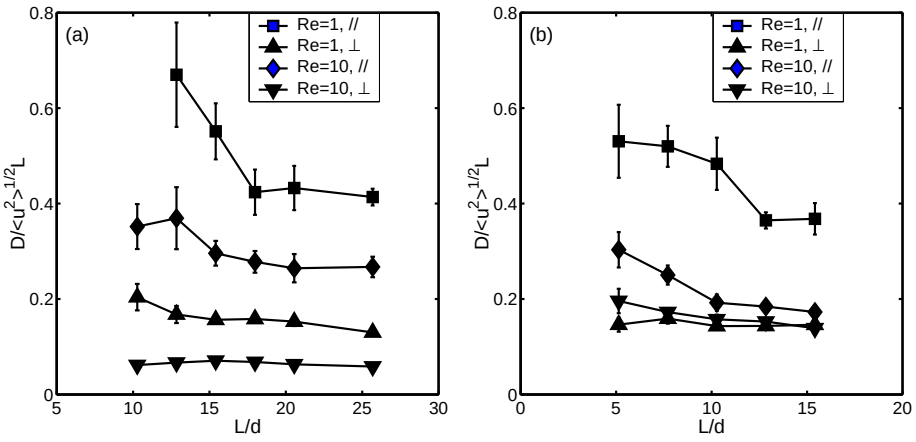

Figure 3.9: The particle diffusivities normalized by the root-mean-square velocity $\langle u^2 \rangle^{1/2}$ and the system size L. (a): dilute suspensions ($\phi = 0.01$); (b): concentrated suspensions ($\phi = 0.20$). The error bars are the standard deviations. The solid lines are included to show the trend that the normalized diffusivities approach constant values with increasing L/d.

Table 3.2: $\Delta u^*_\parallel/\Delta u^*_\perp$ and $D_\parallel/D_\perp$ in the simulations. These ratios are obtained in the largest computational domains with $L/d = 25.7$.

ϕ	Re = 1		Re = 10	
	$\Delta u^*_\parallel/\Delta u^*_\perp$	$D_\parallel/D_\perp$	$\Delta u^*_\parallel/\Delta u^*_\perp$	$D_\parallel/D_\perp$
0.01	2.5	14	3.6	32
0.20	2.1	11	1.7	4.3

positions compared to the vertical positions [61]. In fact, when the computational domain with an oblong shape (2:1) is used, with the longer axis aligned with the settling direction, the ratio of $D_\parallel/D_\perp$ drops significantly to approximately 1/3 of the original value [61]. To check whether the shape of the domain has a similar effect on the diffusivity ratio, we simulated the sedimentation process with Re = 10 and $\phi = 0.01$ in an oblong domain where $L_x/d = 30.8$ and $L_y/d = L_z/d = 15.4$. The result shows that the reduction in $D_\parallel/D_\perp$ in such a domain is merely 20%, much less than the reduction seen in low Re suspensions. Thus, the high diffusivity ratio observed at Re = 10 and $\phi = 0.01$ is not likely affected by the shape of the computational domain, but is more related to the highly anisotropic microstructure of the suspension.

3.4 Summary

In this chapter, we have studied the scaling of the velocity variance and hydrodynamic diffusivity of particles on the size of the computational domain. The particles are monodisperse and spherical, and are with a density ratio twice of that of the fluid. The Reynolds numbers are 1 and 10; the solid volume frac-

tions are chosen to be 0.01 and 0.20 to represent typical dilute and moderately concentrated suspensions.

We find that the particle velocity variance in our suspensions always grows logarithmically with increasing domain size, irrespective of the choice of Re and ϕ. Thus, the logarithmic scaling proposed by Koch [60] is correct not only in dilute suspensions as it was originally intended, but also in more concentrated suspensions. More detailed study on the velocity variance in dilute suspensions shows that the coefficients of the logarithmic growth in the simulations are much less than those predicted by the theory. This difference, we believe, is caused by a partial screening of the velocity disturbances in the wake, where there is a deficit of particles due to the inertial wake interactions between pairs of particles.

We show that the hydrodynamic dispersion in finite Re suspensions is a random-walk process. The dispersion coefficients, or the particle diffusivities, have a stronger dependence on the domain size than the velocity variance. In our simulations, the diffusivities are still proportional to the product of the root-mean-square velocity and the domain size, like in low Re suspensions [61].

By comparing simulations with Re = 1 and those with Re = 10, the effect of inertia on the velocity variance and hydrodynamic dispersion is clear. First of all, with increasing Re, there are less large scale convective motions present in suspensions. Thus, the magnitudes of the velocity variance and the diffusivity of particles are reduced. Secondly, in dilute suspensions the velocity disturbance produced by a particle, the pairwise interaction between particles, and the microstructure of the suspension all become highly anisotropic at high Reynolds numbers. As a result, in high Re dilute suspensions the fluctuating velocities and the hydrodynamic diffusivities are also highly anisotropic.

Chapter 4

Development of a Lattice-Boltzmann Method for the Simulation of Monodisperse, Spherical, Non-Coalescing Bubble Suspensions

4.1 Introduction

Bubbly flows are frequently encountered in chemical engineering applications where contact between gases and liquids is desired to promote heat and mass transport. Typically bubble suspensions differ from suspensions of solid particles in three important ways. First, the fluid velocity can "slip" at the gas-liquid interface; second, the gas-liquid interface can deform, therefore a bubble does not necessarily maintain a predetermined shape; third, bubbles can coalesce and break, leading to a bubble size distribution that is continuously evolving in time. The presence of a slip boundary condition at the gas-liquid interface greatly reduces the vorticity transported from the bubble interface into the liquid at high Reynolds numbers. Consequently the drag on a bubble is much lower than that on a solid particle and the average flow properties of a bubble suspension may differ substantially

from those of solid particle suspensions . To understand the consequences of this distinction in a simple setting, it is desirable to study a bubble suspension in which the bubbles remain spherical and do not coalesce.

In this chapter, we present a newly developed numerical method to simulate a special class of bubbly flows in which the bubbles are nearly spherical and where bubble coalescence is suppressed. Such flows are of fundamental interest since they allow us to isolate the effect of the slip boundary condition. And they are also accessible to laboratory experiments, as discussed in detail below.

The deformability of bubbles in a flow dominated by fluid inertia can be characterized by the Weber number $We = \rho U a^2/\sigma$, where ρ is the density of the liquid, a is the bubble radius, U is the bubble velocity relative to the mean velocity of the suspension or mixture, and σ is the surface tension of the liquid-gas interface. For an inertia-dominated flow with $We \ll 1$, the fluid pressure does not deform the bubbles. Air bubbles with diameters of about 1 mm in clean water are a good example of an inertia-dominated low Weber number system. For slower flows, it is important that the capillary number (ratio of viscous stresses to surface tension) and the Bond number (ratio of gravity to surface tension) be small to assure small deformation of the bubbles. Alternatively, one can consider the Morton and Eotvos numbers of the bubble suspension, which form the basis of the empirical diagram of regimes of bubble deformation presented in Grace, Clift and Weber [24].

Coalescence can be prevented by adding either electrolytes [82] or surfactants to the liquid. It is known that surfactants create a surface tension gradient, which immobilizes the gas-liquid interface and increases the drag [24]. Electrolytes, unlike surfactants, do not cause this so-called Marangoni effect, thus the slip boundary condition at the gas-liquid interface is maintained. The use of electrolytes to

stabilize bubbly suspensions was demonstrated recently by Zenit *et al.* [138], who used a magnesium sulfate solution (0.05 mol/l) to suppress coalescence and were able to maintain a high degree of monodispersity up to 15% volume fractions. Hence, the class of bubbly suspension we study is also experimentally relevant.

Due to the bubble's small deformability and resistance to coalescence, it is most convenient to model this type of bubble suspension as a system of hard spheres with slip boundaries. This model enables us to use a single-component fluid mechanics solver to simulate the flow in the continuous phase and eliminates the need for a second fluid component, which is commonly used in simulations of drops and bubbles. As a result, the computational cost is reduced and the robustness of the computation is improved.

For bubbly suspensions with spherical, non-coalescing bubbles, it is possible to derive the averaged equations of motion from first principles, provided that the Reynolds number is either very small or very large. Here the Reynolds number is defined as $Re = 2\rho U a/\eta$. For $Re \ll 1$, the flow is dominated by viscous effects and governed by the Stokes equation. These equations are linear and can be solved directly by using a multi-pole expansion method (see for example Mo and Sangani [93]). For $Re \gg 1$, as pointed out by Moore [94, 95] and later validated experimentally by Duineveld [33], the vorticity is confined to a small boundary layer near the liquid-gas interface. The fluid velocity outside this boundary layer can be written as the gradient of a potential (hence the name "potential flow"), which is governed by Laplace's equation. Since Laplace's equation is linear, one can solve the potential flow interactions among spherical bubbles and derive the equations of motion for such suspensions [5, 115, 141, 9, 137, 57, 121]. In Zenit *et al.*'s experiments [138], nitrogen bubbles with diameters of about 1 mm in size were

generated and left to rise in a vertical channel filled with water. Here, $Re = O(100)$ and $We = O(1)$, making these experiments the ideal tool to validate the predictions of the potential flow theory. Indeed, good qualitative agreement was found between the results and the theoretical predictions of Spelt and Sangani [121].

In the intermediate Reynolds number regime, however, we cannot use the potential flow approximation, nor can we ignore the presence of inertial effects. This makes it difficult to solve the many-body interaction problem and close the equations of motion. One has to resort to either well controlled experiments or direct numerical simulations. Past numerical work on bubbly flows in the intermediate Reynolds number regime include the works of Esmaeeli and Tryggvason [34, 35], Bunner and Tryggvason [10, 11], Sankaranarayanan *et al.* [117, 118], Sankaranarayanan and Sundaresan [119], Tölke *et al.* [126], and Inamuro *et al.* [52]. These authors used different approaches, but all of them were based on two-component models for the suspension — one component represents the continuous phase; another component, with a density and viscosity that are much smaller than those of the continuous phase, represents the droplets or bubbles. Typically, the density and viscosity ratios are of order 0.01 to 0.02, with the exception of Inamuro *et al.* [52], who was able to implement a projection method into a two-component lattice-Boltzmann model and reduced the density ratio to $\rho_b/\rho = 0.001$. For the sake of comparison, the density and viscosity ratios for air in water under normal conditions are $O(10^{-3})$ and $O(10^{-2})$, respectively.

Using a finite difference method with a front tracking technique, Esmaeeli and Tryggvason studied the rise of an array of deformable, nearly spherical bubbles for $Re = O(1)$ [34] and for deformable, ellipsoidal bubbles at $Re \approx 20$ [35]. Bunner and Tryggvason [10, 11] later used the same method to study the rise of a relatively large

number of nearly spherical bubbles with moderate Reynolds numbers $Re \approx 20$. In their method, the bubbles have well-defined boundaries. Thus coalescence can be prevented by simply not allowing the boundaries to merge when they closely approach each other. It is then possible to study the suspension's properties over relatively long times.

Sankaranarayanan *et al.* [117, 118], Sankaranarayanan and Sundaresan [119], Tölke *et al.* [126], and Inamuro [52] all used a two-component lattice-Boltzmann model for an immiscible binary mixture to simulate the rise of an array of bubbles. This model leads to the formation of bubbles that are by nature deformable, although the bubble's interface is diffusive and often suffers from spurious velocities [132]. As it is difficult to implement a plausible mechanism to prevent the bubbles from coalescing, in [117, 118, 119] only the flow around a single bubble in a periodic box was studied in detail. From the simulations, the drag coefficient, the virtual mass coefficient, and the lift force were obtained and these parameters were then used to propose a set of averaged equations of motion for bubble suspensions at moderate Reynolds numbers.

Our approach differs from the aforementioned studies in that we only attempt to solve the flow in the continuous phase. When the flow drives bubbles into contact, the normal relative velocity of the bubbles is reversed instantaneously as it would be for elastic hard spheres, thereby preventing coalescence without the need to account for the detailed deformation involved during the collision process. The slip boundary condition is imposed on the bubble surface by ensuring explicitly in the lattice-Boltzmann models that there is neither a tangential stress at the surface nor a normal velocity relative to the surface. In this model the bubbles have sharp, well defined interfaces, as opposed to the diffuse interfaces in the conventional two-

phase lattice-Boltzmann models. Our model performs well for density ratios ρ_b/ρ as low as 1.2×10^{-3}, which is the approximate value for air in water under normal conditions. We obtained accurate results from a range of test cases, suggesting that our model captures the essential physics of a bubbly flow and that it can be used as an accurate method to simulate bubbly flows in the moderate Reynolds number regime.

This chapter is organized as follows. In Section 4.2, we give a brief overview of the lattice-Boltzmann method. In Section 4.3, we derive the new boundary rule to recover the slip boundary condition at the liquid-gas interface. In Section 4.4, we discuss three test cases: i) unidirectional flow in a system bounded by a free surface from above and driven by an impulsively started solid plate from below, ii) creeping flow past a cubic array of bubbles, and iii) moderate Reynolds number steady and unsteady flows around an isolated bubble. The first two test cases have analytical solutions, the last one has been studied extensively in the past [24, 67, 134, 85, 91, 103]. In Section 4.5, we conclude with a summary and a discussion of our main results.

4.2 Review on the lattice-Boltzmann method

Our numerical method is based on a lattice-Boltzmann model for particle-laden flows as reviewed in detail by Ladd and Verberg [76]. The lattice-Boltzmann method is different from most conventional numerical methods in fluid dynamics in the sense that it does not involve a direct solution of the continuum equations. Rather, it uses a simplified kinetic model to simulate the motion of fluid "particles" on a simple lattice such that the averaged properties of the system obey the desired

Navier-Stokes equation. It is also different from molecular simulations since it does not deal with individual molecules but rather with their velocity distribution function. The lattice-Boltzmann method is therefore a mesoscopic model, whose local rules are guided by molecular phenomena, but whose emergent behavior captures the continuum properties of the system. Due to this mesoscopic nature, the lattice-Boltzmann method is very versatile, leading to the a wide variety of models for a range of different applications [76, 19, 71, 72].

The fundamental quantity in the lattice-Boltzmann method, as in all kinetic models, is the single-particle velocity distribution function $n_i(\mathbf{r}, t) \equiv n(\mathbf{r}, \mathbf{c}_i, t)$, describing the density of fluid particles at position $\mathbf{r}$ and time t, with a velocity $\mathbf{c}_i$. Here, $\mathbf{r}$, $\mathbf{c}_i$ and t are discrete variables, but the distribution function itself is continuous. In three dimensions, $\mathbf{r}$ takes on the values from a space-filling rectangular lattice. We used a discrete set of 19 velocities to represent the velocity space. These velocities correspond to fluid particles that can either stay at their current lattice position ($\mathbf{c} = [\,000\,]$), or propagate to the nearest ($\mathbf{c} = [\,100\,]$) and next-nearest ($\mathbf{c} = [\,110\,]$) neighbors on a cubic lattice. The macroscopic properties, the density ρ, the momentum density $\mathbf{j}$, and the momentum flux $\mathbf{\Pi}$, are then moments of n_i over the discrete velocity space, i.e.,

$$\begin{aligned} \rho &= \sum_i n_i \\ \mathbf{j} &= \sum_i n_i \mathbf{c}_i = \rho \mathbf{u} \\ \mathbf{\Pi} &= \sum_i n_i \mathbf{c}_i \mathbf{c}_i \ . \end{aligned} \tag{4.1}$$

Here, $\mathbf{u}$ is the local fluid velocity.

The time evolution of the velocity distribution function is governed by a discretized Boltzmann equation [38], and occurs as a sequence of two steps, a collision

step and a propagation step:

$$n_i\left(\mathbf{r}+\mathbf{c}_i\Delta t, t+\Delta t\right)=n_i^*\left(\mathbf{r},t\right)=n_i\left(\mathbf{r},t\right)+\Delta_i\left[\mathbf{n}\left(\mathbf{r},t\right)\right]\ . \tag{4.2}$$

In the collision step, all populations at $\mathbf{r}$ undergo instantaneous molecular collisions, producing the post-collision distribution $n_i^*\left(\mathbf{r},t\right)$. Here, the collision operator, Δ_i, represents the change in n_i due to this collision process. In the propagation step, the post-collision populations travel to neighboring nodes in the direction of their velocity $\mathbf{c}_i$. The time step Δt and the lattice spacing Δx are chosen such that fluid particles always reach the next node in the direction of their velocity in precisely one time step.

Each n_i can be divided into an equilibrium part and a non-equilibrium part: $n_i \equiv n_i^{eq}+n_i^{neq}$, where the n_i evolve in time toward local equilibrium. For flow velocities much less than the speed of sound, the equilibrium part can be obtained by expanding the Maxwell-Boltzmann distribution as a Taylor series in the local velocity $\mathbf{u}$, i.e.,

$$n_i^{eq}=a^{c_i}\left[\rho+\frac{\mathbf{j}\cdot\mathbf{c}_i}{c_s^2}+\frac{\rho\mathbf{u}\mathbf{u}:\left(\mathbf{c}_i\mathbf{c}_i-c_s^2\mathbf{I}\right)}{2c_s^4}\right]\ , \tag{4.3}$$

where $\mathbf{I}$ is the unit tensor. Here c_s is the isothermal speed of sound in the fluid, which is chosen as $c/\sqrt{3}$, with $c=\Delta x/\Delta t$. The weights a^{c_i} describe the fraction of molecules moving in the direction of $\mathbf{c}_i$. They only depend on the magnitude of the velocity and are equal to $\frac{1}{3}$, $\frac{1}{18}$, and $\frac{1}{36}$ for the $[\,000\,]$, $[\,100\,]$, and $[\,110\,]$ directions, respectively. The expansion in Eq. (4.3) is truncated at $O(\mathbf{u}^2)$, which turns out to be sufficient to simulate the Navier-Stokes equation [46]. The second moment of the equilibrium distribution function gives the familiar Eulerian expression for the stress tensor with an ideal-gas equation of state $p=\rho c_s^2$:

$$\mathbf{\Pi}^{eq}=\sum_i n_i^{eq}\mathbf{c}_i\mathbf{c}_i=p\mathbf{I}+\rho\mathbf{u}\mathbf{u}\ . \tag{4.4}$$

The collision operator can take any form subject to the constraints of mass and momentum conservation. The most widely used one is the so-called single exponential relaxation time collision operator $\Delta_i = -n_i^{neq}/\tau$ [107, 17, 20]. However, for reasons discussed in detail by Ladd and Verberg [76] and d'Humières *et al.* [30] (among others), we used the more general collision operator [76],

$$\Delta_i = \sum_j \mathcal{L}_{ij} n_j^{neq}(\mathbf{r}, t) \ . \tag{4.5}$$

Here, $\mathcal{L}_{ij}$ are the matrix elements of the linearized collision operator $\mathcal{L}$ that must satisfy the following eigenvalue equations

$$\begin{aligned}
\sum_i \mathcal{L}_{ij} &= 0 \\
\sum_i \mathbf{c}_i \mathcal{L}_{ij} &= 0 \\
\sum_i \overline{\mathbf{c}_i \mathbf{c}_i} \mathcal{L}_{ij} &= \lambda \overline{\mathbf{c}_j \mathbf{c}_j} \\
\sum_i c_i^2 \mathcal{L}_{ij} &= \lambda_B c_j^2 \ ,
\end{aligned} \tag{4.6}$$

where $\overline{\mathbf{c}_i \mathbf{c}_i}$, indicates the traceless part of $\mathbf{c}_i \mathbf{c}_i$. The first two equations follow from conservation of mass and momentum, and the last two equations describe the relaxation of the viscous stress tensor. The eigenvalues λ and λ_B must lie in the range $(-2, 0)$ and are related to the shear and bulk viscosities through [76]

$$\begin{aligned}
\eta &= -\rho c_s^2 \Delta t \left(\frac{1}{\lambda} + \frac{1}{2} \right) \\
\eta_B &= -\frac{2\rho c_s^2 \Delta t}{3} \left(\frac{1}{\lambda_B} + \frac{1}{2} \right) \ .
\end{aligned} \tag{4.7}$$

Mass and momentum are conserved quantities and therefore unmodified during the collision step; hence $\sum_i n_i^{neq} = \sum_i n_i^{neq} \mathbf{c}_i = 0$, as can be readily verified from Eqs. (4.1) and (4.3). However, the second moment of n_i^{neq}, i.e., $\mathbf{\Pi}^{neq} \equiv \mathbf{\Pi} - \mathbf{\Pi}^{eq} = \sum_i n_i^{neq} \mathbf{c}_i \mathbf{c}_i$, is in general non-zero and modified during the collision process. Hence,

its post-collision value, $\mathbf{\Pi}^{neq,*}$, depends on the particular choice of the collision operator; in our case (see Eqs. (4.5) and (4.6)) this results in [76]

$$\mathbf{\Pi}^{neq,*} = (1+\lambda)\overline{\mathbf{\Pi}^{neq}} + \frac{1}{3}(1+\lambda_B)(\mathbf{\Pi}^{neq} : \mathbf{I})\mathbf{I} \ , \tag{4.8}$$

where $\overline{\mathbf{\Pi}^{neq}}$ stands for the traceless part of $\mathbf{\Pi}^{neq}$. The post-collision distribution function in Eq. (4.3) can then be written as

$$n_i^* = a^{c_i}\left[\rho + \frac{\mathbf{j}\cdot\mathbf{c}_i}{c_s^2} + \frac{(\rho\mathbf{u}\mathbf{u} + \mathbf{\Pi}^{neq,*}) : (\mathbf{c}_i\mathbf{c}_i - c_s^2\mathbf{I})}{2c_s^4}\right] \ . \tag{4.9}$$

Thus, Eqs. (4.8) and (4.9) determine explicitly the post-collision distribution function in terms of moments of the pre-collision distribution function.

Eq. (4.9) describes the evolution of the lattice-Boltzmann model in the absence of external forces. If an external force density is present, e.g., a pressure gradient or a gravitational field, the evolution of the lattice-Boltzmann model includes additional contributions as discussed in [76].

By using multi-time-scale analysis, one can show that the lattice-Boltzmann model as described in this section recovers the incompressible Navier-Stokes equation in the limit of small Mach number $M = u/c_s \ll 1$ [76]. In our simulation we kept M below 0.1. This limits u to a fairly small number, hence in order to increase the range of Reynolds numbers we decreased the viscosity and increased the bubble radii. Furthermore, since compressibility effects are of order M^2, we set $\lambda_B = -1$, such that the isotropic part of $\mathbf{\Pi}^{neq}$ relaxes to zero in one lattice-Boltzmann time step.

4.3 Development of a lattice-Boltzmann boundary rule for the no-slip boundary condition

During the propagation step of the lattice-Boltzmann algorithm, the post-collision populations either stay at the same node or propagate to a neighboring node depending on their velocities. If this propagation would cause fluid particles to cross a fluid-solid or fluid-bubble interface, a boundary condition must be applied. For a solid interface, a large number of different approaches are available in the literature [38, 71, 128, 41, 92, 21] (among others). A particularly simple and robust means of imposing a no-slip boundary condition at a solid-fluid interface is the so-called link-bounce-back rule [38, 71]. Here, the interface is represented by boundary nodes, defined as those positions located halfway along each link that connects neighboring solid and fluid nodes. Populations of fluid particles that are propagating toward a boundary node are reflected back in the direction from which they came from with a modified velocity distribution function given by [71]

$$n_{i'}\left(\mathbf{r}, t+\Delta t\right) = n_i^*\left(\mathbf{r}, t\right) - \frac{2\rho a^{c_i}\mathbf{c}_i \cdot \mathbf{u}_b\left(\mathbf{r}_b, t\right)}{c_s^2} \tag{4.10}$$

Here $n_{i'}$ is the population with a velocity in the opposite direction of the incoming velocity ($\mathbf{c}_{i'} = -\mathbf{c}_i$), and $\mathbf{r}_b = \mathbf{r} + \frac{1}{2}\mathbf{c}_i\Delta t$ and $\mathbf{u}_b$ are the respective position and velocity of the boundary node. Eq. (4.10) results in a no-slip boundary condition that is satisfied at the boundary node, i.e., half way between the fluid node and its neighboring solid node with a relative error that is of first order in the spatial discretization [47].

To simulate bubbly flows, we need to develop a method that enforces a free-slip boundary condition at the fluid-bubble interface. Similar to the link-bounce-back rule for fluid-solid interfaces, we represent the bubble interface by boundary nodes

that are located halfway along each link that crosses the fluid-bubble interface. We then assume again that it is possible to write

$$n_{i'}(\mathbf{r}, t + \Delta t) = n_i^*(\mathbf{r}, t) + \delta_i(\mathbf{r}, t) \ . \tag{4.11}$$

Here, δ_i has to be determined such that Eq. (4.11) recovers the slip boundary condition at all boundary nodes. Hence, the condition of zero normal velocity,

$$\mathbf{n} \cdot \mathbf{u} = \mathbf{n} \cdot \mathbf{u}_b \ , \tag{4.12}$$

and the condition of zero tangential stress

$$\mathbf{n} \cdot \boldsymbol{\sigma} \cdot (\mathbf{I} - \mathbf{nn}) = \mathbf{0} \ , \tag{4.13}$$

must be satisfied at the entire bubble surface. Here $\mathbf{n}$ is the unit normal vector to the interface pointing into the fluid, $\mathbf{u}_b$ is the bubble velocity, $\mathbf{u}$ is the local fluid velocity, and $\boldsymbol{\sigma}$ is the local fluid viscous stress tensor, all calculated at the fluid-bubble interface. Eqs. (4.12) and (4.13) originate from the boundary conditions of velocity and shear stress at a fluid-fluid interface [24] in the limit that the viscosity of the fluid inside the spherical interface is vanishingly small. In general both velocity and shear stress must be continuous across the interface. However, when the viscosity of the fluid inside is negligible compared to that of the fluid outside, e.g., an air bubble in a liquid, the shear stress inside the bubble is very small and can be neglected. In this case, the shear stress of the fluid outside will also vanish at the interface. As a result, no boundary condition is required on the tangential velocity of the fluid outside the bubble, since the tangential velocity of the gas can adjust to any tangent fluid velocity outside without causing a significant shear stress. The normal velocity, however, is constrained by kinematic conditions, which require the fluid velocity normal to the interface to equal the normal velocity of

the interface. Finally, in a real bubble, the difference in the normal stress across the interface is balanced by the surface tension. Our assumption that the bubble is always spherical implies the surface tension is always sufficient to equal the normal stress difference with minimal bubble deformation. Thus we do not have a constraint on the normal stress of the fluid outside.

Our derivation of the free-slip boundary condition closely follows that of Ladd and Verberg [76] for the link bounce-back rule for solid-fluid interfaces. Here, we need the fact that the multi-time-scale analysis shows that $\boldsymbol{\sigma}$ in Eq. (4.8) equals $-\boldsymbol{\Pi}^{neq}$ [76] and has the form:

$$\boldsymbol{\sigma} = -\boldsymbol{\Pi}^{neq} = -\frac{\rho c_s^2 \Delta t}{\lambda}\left[\left(\nabla\mathbf{u} + \nabla\mathbf{u}^{\mathrm{T}}\right) - \frac{2}{3}\left(\nabla\cdot\mathbf{u}\right)\mathbf{I}\right] - \frac{2\rho c_s^2 \Delta t}{3\lambda_v}\left(\nabla\cdot\mathbf{u}\right)\mathbf{I}\ , \quad (4.14)$$

Substituting Eq. (4.14) into Eqs. (4.8) and (4.9) and using the fact that the velocity distribution function can be expanded in terms of its moments as

$$n_i = a^{c^i}\left[\rho + \frac{\mathbf{j}\cdot\mathbf{c}_i}{c_s^2} + \frac{\left(\boldsymbol{\Pi} - \rho c_s^2\mathbf{I}\right) : \left(\mathbf{c}_i\mathbf{c}_i - c_s^2\mathbf{I}\right)}{2c_s^4}\right] \quad (4.15)$$

yields a post-collision distribution expressed in terms of the local velocity gradients

$$n_i^*\left(\mathbf{r},t\right) = n_i\left(\mathbf{r},t\right) + \frac{\rho a^{c_i}\Delta t}{c_s^2}\left(\mathbf{c}_i\cdot\nabla\mathbf{u}\cdot\mathbf{c}_i - c_s^2\nabla\cdot\mathbf{u}\right)\ . \quad (4.16)$$

Substituting Eq. (4.14) into Eq. (4.13) implies that the no tangential stress boundary condition at the fluid-bubble interface can also be expressed in terms of the local velocity gradients:

$$\mathbf{n}\cdot\left(\nabla\mathbf{u} + \nabla\mathbf{u}^{\mathrm{T}}\right)\cdot\left(\mathbf{I} - \mathbf{nn}\right) = \mathbf{0}\ . \quad (4.17)$$

Using Eqs. (4.16) and (4.17) and then decomposing the local velocity gradient in components that are normal and tangential to the fluid-bubble interface, we obtain

$$n_i^*\left(\mathbf{r},t\right) = n_i\left(\mathbf{r},t\right) + \frac{\rho a^{c_i}\Delta t}{c_s^2}\left[\left(\mathbf{c}_i\cdot\mathbf{n}\right)^2\left(\mathbf{nn} : \nabla\mathbf{u}\right) + \mathbf{c}_i\cdot\mathbf{P}_{\parallel}\cdot\nabla\mathbf{u}\cdot\mathbf{P}_{\parallel}\cdot\mathbf{c}_i\right]\ , \quad (4.18)$$

with $\mathbf{P}_{\parallel} \equiv (\mathbf{I} - \mathbf{nn})$ being an operator that projects a vector into the plane tangent to the interface. Here, we neglected terms proportional to $\nabla \cdot \mathbf{u}$, which are of second order in the Mach number and can therefore be ignored in our simulations.

In the link-bounce-back rule, the adjustment to the reflected populations [the second term on the right hand side of Eq. (4.10)] assures that any distribution at node $\mathbf{r}$ that is consistent with the boundary node velocity $\mathbf{u}_b$ is stationary with respect to interactions with the boundary nodes. This requires that $n_{i'}(\mathbf{r}, t + \Delta t) = n_{i'}(\mathbf{r}, t)$ for any velocity $\mathbf{u}_b$ at the fluid-solid interface. To simulate bubbles, we require the same condition in order to obtain δ_i in Eq. (4.11), resulting in

$$\delta_i(\mathbf{r}, t) = n_{i'}(\mathbf{r}, t) - n_i^*(\mathbf{r}, t) \ , \tag{4.19}$$

for the boundary conditions in Eqs. (4.12) and (4.13). Substituting Eq. (4.18) into Eq. (4.19), and using Eq. (4.15) to relate two populations n_i and $n_{i'}$ with equal and opposite velocities at the same position and time results in

$$\delta_i = -\frac{2\rho a^{c_i}}{c_s^2}\mathbf{c}_i \cdot \mathbf{u} - \frac{\rho a^{c_i}\Delta t}{c_s^2}\left[(\mathbf{c}_i \cdot \mathbf{n})^2 (\mathbf{nn} : \nabla \mathbf{u}) + \mathbf{c}_i \cdot \mathbf{P}_{\parallel} \cdot \nabla \mathbf{u} \cdot \mathbf{P}_{\parallel} \cdot \mathbf{c}_i\right] \ . \tag{4.20}$$

Assuming that the fluid velocity varies over a length scale that is large compared to the lattice spacing, the fluid velocity at the boundary can be expanded in a Taylor series such that to leading order in the velocity gradients

$$\mathbf{u}(\mathbf{r}_b, t) = \mathbf{u}(\mathbf{r}, t) + \frac{\Delta t}{2}\mathbf{c}_i \cdot \nabla \mathbf{u}|_{\mathbf{r},t} \ , \tag{4.21}$$

Applying the boundary condition for the normal velocity at the interface [Eq. (4.12)] leads to

$$\begin{aligned} \mathbf{n} \cdot \mathbf{u}_b(\mathbf{r}_b, t) &= \mathbf{n} \cdot \mathbf{u}(\mathbf{r}, t) + \frac{\Delta t}{2}\mathbf{n} \cdot (\mathbf{c}_i \cdot \nabla \mathbf{u})|_{\mathbf{r},t} \\ &\approx \mathbf{n} \cdot \mathbf{u}(\mathbf{r}, t) + \frac{\Delta t}{2}(\mathbf{c}_i \cdot \mathbf{n})(\mathbf{nn} : \nabla \mathbf{u})|_{\mathbf{r},t} \ , \end{aligned} \tag{4.22}$$

with $\mathbf{u}_b$ again the velocity of the interface at the boundary node. Here, we neglected gradients in the tangential direction of the normal component of the velocity gradient, which is correct for a flat interface and applies to leading order to curved interfaces as well (i.e. for bubbles with radii that are large compared to the lattice spacing). Decomposing $\mathbf{c}_i \cdot \mathbf{u}$ in Eq. (4.20) into a sum of products of the normal and tangential components and using Eq. (4.22) to express the normal component of the fluid velocity at the interface in terms of the normal component of the boundary node velocity then yields

$$\delta_i = -\frac{2\rho a^{c_i}}{c_s^2}\left(\mathbf{c}_i \cdot \mathbf{nn} \cdot \mathbf{u}_b + \mathbf{c}_i \cdot \mathbf{P}_\parallel \cdot \mathbf{u} + \frac{\Delta t}{2}\,\mathbf{c}_i \cdot \mathbf{P}_\parallel \cdot \nabla\mathbf{u} \cdot \mathbf{P}_\parallel \cdot \mathbf{c}_i\right) . \tag{4.23}$$

The first term in Eq. (4.23) is similar to the change in population density in the link-bounce-back rule for the no-slip boundary condition except that only the normal components of the fluid and bubble velocities are involved. This reflects the fact that the tangential velocity at a free-slip boundary is not specified by the boundary conditions. The second and third terms on the right-hand side of Eq. (4.23) are adjustments to the population density that are obtained by using the zero tangential stress boundary condition and by using a tangential velocity at the boundary that is obtained from a Taylor series expansion of the velocity field about the fluid node.

Using $\mathbf{j} = \rho\mathbf{u}$ and Eq. (4.14) to express $\mathbf{u}$ and $\nabla\mathbf{u}$ back in terms of the first and second moment of the velocity distribution function, we finally arrive at

$$\begin{aligned} n_{i'}(\mathbf{r}, t+\Delta t) &= n_i^*(\mathbf{r}, t) - \frac{2a^{c_i}}{c_s^2}\left[\mathbf{c}_i \cdot \mathbf{nn} \cdot \rho\mathbf{u}_b(\mathbf{r}_b, t) + \mathbf{c}_i \cdot \mathbf{P}_\parallel \cdot \mathbf{j}(\mathbf{r}, t)\right] \\ &- \frac{\lambda a^{c_i}}{2c_s^4}\mathbf{c}_i \cdot \mathbf{P}_\parallel \cdot \overline{\mathbf{\Pi}^{neq}}(\mathbf{r}, t) \cdot \mathbf{P}_\parallel \cdot \mathbf{c}_i \ . \end{aligned} \tag{4.24}$$

Similar to the link-bounce-back rule for solid interface, this result is explicit in

time and first-order accurate in the spatial discretization with relative errors that are of second order in the Mach number.

4.4 Validation tests

We present three test problems to validate the new free-slip boundary rule in Eq. (4.24) as derived in the previous section. The first problem is a unidirectional flow above an impulsively started plate. Due to the two-dimensional nature and the simple geometry, it is possible to show the detailed actions of the propagation and bounce-back rules such that one can observe the differences between the no-slip bounce-back rule and the new rule for slip boundaries. In addition, since an analytical solution is available, this problem provides an opportunity to verify both the transient and the steady state behavior of the simulation. The second problem is the creeping flow around a cubic array of bubbles. In this problem, the model's ability to handle curved interfaces at a low Reynolds number is tested. This problem also serves as a calibration, from which the accuracy of the method can be improved. The last problem is a study of bubbles rising under gravity at moderate Reynolds numbers. By comparing the acceleration and terminal drag to results from the literature we validate the ability of the new model to simulate steady and unsteady bubbly flows where inertial effects are important.

4.4.1 Planar flow with a free surface driven by a flat plate

In this section we consider a two-dimensional unidirectional flow of a fluid bounded by a solid plate from below (at $y = L$) and a free surface from above (at $y = 0$) [see Fig. (4.1)]. Initially, the entire fluid is at rest. At time $t = 0$, the solid wall is set in

motion with a constant velocity U in the x direction. The fluid is accelerated by the momentum transferred from the solid wall to the fluid, and quickly develops into a plug flow because the free surface does not provide resistance of any kind. In this problem, the full Navier-Stokes equations reduce to a parabolic partial differential equation with a Fourier series solution,

$$\frac{u_x(y,t)}{U} = 1 - \sum_{k=0}^{\infty} \frac{4\,(-1)^k}{(2k+1)\,\pi}\, e^{-\frac{(2k+1)^2\pi^2\eta t}{4\rho L^2}} \cos\left[\frac{(2k+1)\,\pi y}{2L}\right] , \tag{4.25}$$

against which the accuracy of the new bounce-back rule can be tested directly.

Since the flow is planar, we project the three-dimensional 19-velocity lattice-Boltzmann model onto the xy-plane to a two-dimensional 9-velocity lattice-Boltzmann model. The resulting set of velocities and their associated weights are summarized in Table 4.1. We used $\rho = 36$ and $\Delta x = \Delta t = 1$, giving $c_s^2 = 1/3$. Since the flow properties only depend on the y coordinate we only need a single column of N lattice nodes. Periodic boundary conditions are then applied in the x direction. Furthermore, since both the link-bounce-back rule for a fluid-solid boundary and the new rule for a fluid-gas boundary simulate an interface position that is half way between the fluid node and its neighboring solid or gas node, we position the first and last node half a lattice unit away from the computational domain boundaries [see Fig. (4.1) for $L = N = 8$]. The fluid is at rest at $t = 0$, i.e. $\mathbf{j}(\mathbf{r}_j, 0) = 0$ and $\mathbf{\Pi}(\mathbf{r}_j, 0) = p\mathbf{I}$ throughout the entire fluid domain. Hence, the initial populations at each fluid node are simply $n_i(\mathbf{r}_j, 0) = \rho a^{c_i}$, while being unmodified by the first collision step. Therefore,

$$n_0^*\,(\mathbf{r}_j, 0) = 16, \;\; n_{1,\ldots,4}^*\,(\mathbf{r}_j, 0) = 4, \;\; n_{5,\ldots,8}^*\,(\mathbf{r}_j, 0) = 1 \;, \tag{4.26}$$

for $j = 1, \ldots, 8$.

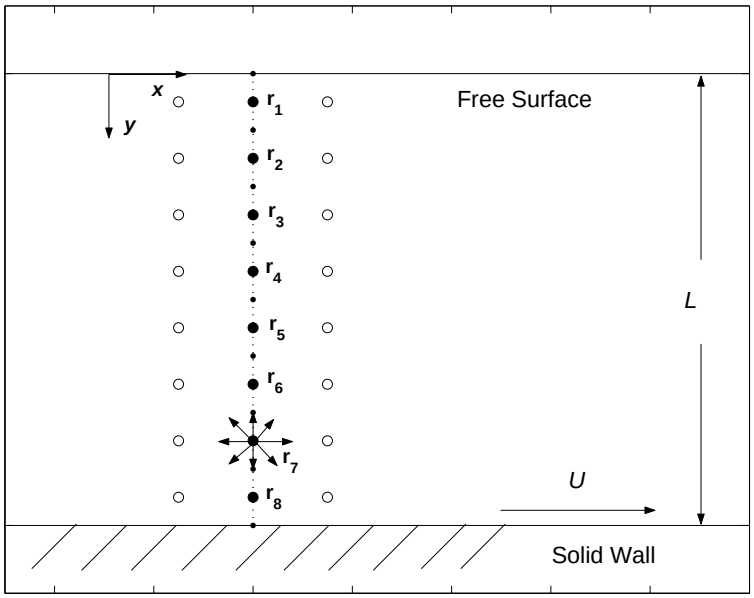

Figure 4.1: The computational domain between the free surface and the solid wall is divided equally into 8 segments. The filled circles are the fluid nodes $\mathbf{r}_1, \ldots, \mathbf{r}_8$ and the open circles are their periodic images.

Table 4.1: The two-dimensional 9-velocity lattice-Boltzmann model.

i	a^{c_i}	$\mathbf{c}_i$
0	4/9	$(0,0)$
1,2	1/9	$(\pm 1, 0)$
3,4	1/9	$(0, \pm 1)$
5,6	1/36	$(\pm 1, 1)$
7,8	1/36	$(\pm 1, -1)$

The propagation step for the inner fluid nodes $(\mathbf{r}_2, \ldots, \mathbf{r}_7)$ does not involve the boundary rules and follows straightforwardly from Eq. (4.2):

$$\begin{aligned} n_{0,1,2}(\mathbf{r}_j, t+1) &= n^*_{0,1,2}(\mathbf{r}_j, t) \\ n_{3,5,6}(\mathbf{r}_j, t+1) &= n^*_{3,5,6}(\mathbf{r}_{j-1}, t) \\ n_{4,7,8}(\mathbf{r}_j, t+1) &= n^*_{4,7,8}(\mathbf{r}_{j+1}, t) \ , \end{aligned} \tag{4.27}$$

for $j = 2, \ldots, 7$.

The nodes $\mathbf{r}_1$ and $\mathbf{r}_8$ need special treatment. The populations at $\mathbf{r}_8$ with velocities $\mathbf{c}_4$, $\mathbf{c}_7$, and $\mathbf{c}_8$ are determined by the link-bounce-back rule for a solid interface as given by Eq. (4.10), i.e.,

$$\begin{aligned} n_4(\mathbf{r}_8, t+1) &= n^*_3(\mathbf{r}_8, t) \\ n_7(\mathbf{r}_8, t+1) &= n^*_6(\mathbf{r}_8, t) + 6U \\ n_8(\mathbf{r}_8, t+1) &= n^*_5(\mathbf{r}_8, t) - 6U \ . \end{aligned} \tag{4.28}$$

Similarly, the populations at $\mathbf{r}_1$ with velocities $\mathbf{c}_3$, $\mathbf{c}_5$, and $\mathbf{c}_6$ are determined by the new free-slip boundary condition for a fluid-gas interface as given by Eq. (4.11), i.e.,

$$\begin{aligned} n_3(\mathbf{r}_1, t+1) &= n^*_4(\mathbf{r}_1, t) \\ n_5(\mathbf{r}_1, t+1) &= n^*_8 + \frac{1}{6}(n^*_1 - n^*_2 + n^*_5 - n^*_6 + n^*_7 - n^*_8) \\ &\quad -\frac{\lambda}{8}(n^{neq}_1 + n^{neq}_2 + n^{neq}_5 + n^{neq}_6 + n^{neq}_7 + n^{neq}_8) \\ n_6(\mathbf{r}_1, t+1) &= n^*_7 - \frac{1}{6}(n^*_1 - n^*_2 + n^*_5 - n^*_6 + n^*_7 - n^*_8) \\ &\quad -\frac{\lambda}{8}(n^{neq}_1 + n^{neq}_2 + n^{neq}_5 + n^{neq}_6 + n^{neq}_7 + n^{neq}_8) \end{aligned} \tag{4.29}$$

For clarity, we omitted the arguments on the right hand side of the last two equation which are all $(\mathbf{r}_1, t)$. Note that because of the particularly simple geometry, the

update rule for n_3 is identical to that what would have been obtained by using the regular link-bounce-back rule.

Compare Eqs. (4.28) and (4.29) and one can see the difference between the bounce-back rule for a solid interface and the rule for a fluid-gas interface. There are three terms on the right hand side of Eq. (4.29) (for n_5 and n_6). The first term originates from the regular bounce-back which is identical in both rules. The second term is proportional to the local fluid velocity parallel to the surface and is related to the second term in Eq. (4.23). The third term is proportional to the local fluid stress projected on the interface and is related to the third term in Eq. (4.23).

The remaining populations at node $\mathbf{r}_1$ and $\mathbf{r}_8$ follow the standard lattice-Boltzmann propagation rule, as in Eq. (4.27):

$$\begin{aligned} n_{0,1,2}(\mathbf{r}_1, t+1) &= n^*_{0,1,2}(\mathbf{r}_1, t) \\ n_{4,7,8}(\mathbf{r}_1, t+1) &= n^*_{3,6,5}(\mathbf{r}_2, t) \\ n_{0,1,2}(\mathbf{r}_8, t+1) &= n^*_{0,1,2}(\mathbf{r}_8, t) \\ n_{3,5,6}(\mathbf{r}_8, t+1) &= n^*_{3,5,6}(\mathbf{r}_7, t) \ . \end{aligned} \tag{4.30}$$

After resolving the propagation step and the boundary conditions, the populations at each node undergo collisions as determined by Eqs. (4.2), (4.8), and (4.9). The new populations are then ready for the next time step.

Fig. (4.2) shows the development of the velocity profile in the gap. The velocities are obtained from the first moments of the n_i's [Eq. (4.1)]. Comparing the simulation with the Fourier series solution of Eq. (4.25), we see that using only 8 fluid nodes already captures successfully the full transient behavior of flow field. Increasing the resolution to $L = N = 32$ makes the numerical solution even

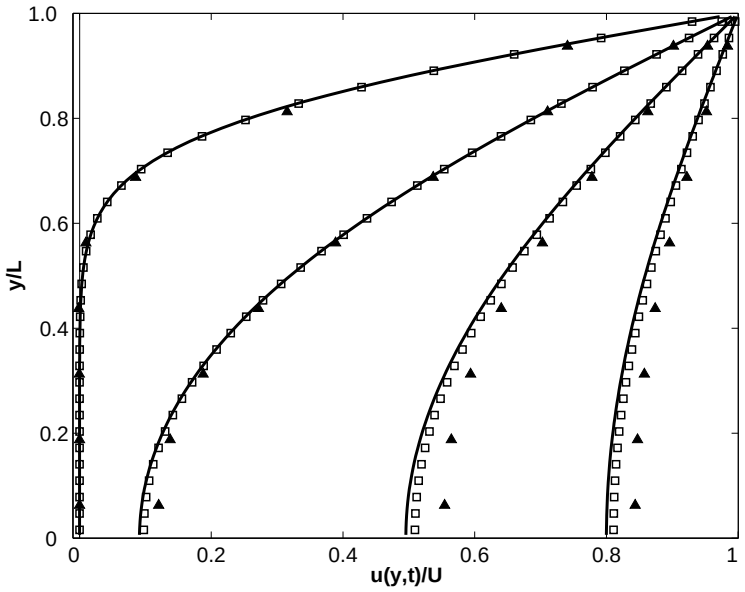

Figure 4.2: Velocity profiles above an impulsively started plate at non-dimensional times $\tau = \eta t/\rho L^2 = 1/64$, $1/8$, $3/8$, and $3/4$ (from left to right). The fluid is bounded by a solid wall at $y/L = 1$ and a free surface at $y = 0$. The fluid density $\rho = 36$, the wall velocity $U = 10^{-3}$, and the viscosity $\eta = 0.36$. The symbols are the lattice-Boltzmann results for $L = N = 8$ (filled triangles) and $L = N = 32$ (open squares). The solid lines are obtained from the Fourier series solution [Eq. (4.25)], by truncating the series at $k = 10000$.

more accurate. For $\eta t/\rho L^2 \to \infty$, the numerical solution approaches the plug flow solution $u_x(y)/U = 1$ [not shown in Fig. (4.2)].

The rate at which the errors decrease with increasing resolution can be observed from Fig. (4.3). The error is defined as

$$\epsilon(L,\tau) = \frac{1}{U}\left(\frac{1}{L}\sum_{\mathbf{r}\in L}\left[u_s\left(\mathbf{r},\tau\right) - u_x\left(\mathbf{r},\tau\right)\right]^2\right)^{1/2} \tag{4.31}$$

where $\tau = \eta t/\rho L^2$ is the non-dimensional time, $u_s(\mathbf{r},\tau)$ is the simulated velocity

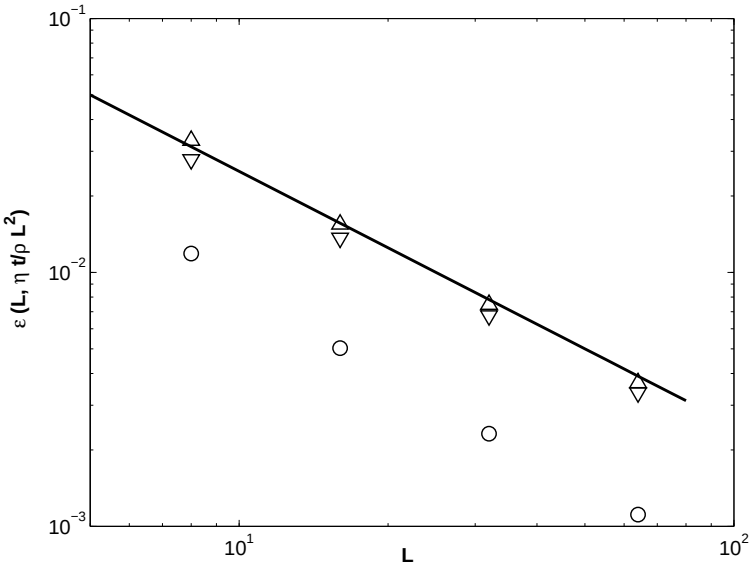

Figure 4.3: Root mean square error $\epsilon(L, \tau)$ at non-dimensional times $\tau = 1/8(\circ)$, $3/8(\triangle)$, and $3/4(\triangledown)$. The solid line represents the scale of L^{-1}. $L = 8$, 16, 32, and 64.

profile and $u_x(y, t)$ is the velocity profile according to Eq. (4.25). The results shown in Fig. (4.3) are obtained using four different resolutions: $L = N = 8$, 16, 32, and 64. They indicate that $\epsilon(L, \tau)$ scales roughly as L^{-1}, which means our method is first order accurate in lattice resolution.

4.4.2 Creeping flow past a cubic array of spherical bubbles

One of the great advantages of the link-bounce-back rule for the lattice-Boltzmann method is its ability to accurately handle curved interfaces and complex geometries with relative ease. By simulating the Stokes drag force on a cubic array of bubbles, we demonstrate here that this advantage also holds for our new boundary conditions. In these simulations, a cubic array of bubbles is constructed by placing

a single spherical bubble in a cubic computational domain and applying periodic boundary conditions in each direction. The bubble is then given a constant velocity U but its position is not advanced across the lattice. This artifice yields the correct fluid velocity and drag on the bubble owing to the quasi-steady nature of Stokes flows. A pressure gradient is applied to the fluid with a value that is adjusted to insure that the volume average velocity in the cubic cell (including the fluid and the bubble) is zero. We then calculated the total drag force F_D on the bubble from the exchange in momentum during the boundary node update [71]. The velocity U was chosen to be low enough to neglect any inertial effects, allowing us to compare our results with the theoretical prediction obtained by Sangani and Acrivos [114],

$$\frac{F_D(\phi)}{F_D^0} = \frac{1}{1 - 1.1734\phi^{1/3} - 0.1178\phi^2 + o(\phi^2)} \ , \tag{4.32}$$

where ϕ is the volume fraction and $F_D^0 = F_D(\phi = 0)$ is the Stokes drag force on an isolated bubble,

$$F_D^0 = 4\pi\eta a U \ , \tag{4.33}$$

with a being the bubble radius. The fact that the drag force on a bubble in a cubic array is larger than that on an isolated bubble is due to the hydrodynamic interactions between the bubble and its periodic images. Note, that the same procedure was used by Ladd [71] to simulate the Stokes drag force on a cubic array of spherical solid particles.

In Fig. (4.4), we summarize the results for a bubble radius $a = 2.92$ and velocity $U = 10^{-4}$. The fluid density and viscosity are $\rho = 36$ and $\eta = 6.0$, respectively. These parameters give $Re = 3.5 \times 10^{-3}$. Due to the discrete lattice, the drag force on a bubble varies slightly as the bubble's position changes relative to the underlying lattice. To minimize this discretization error, every data point is the

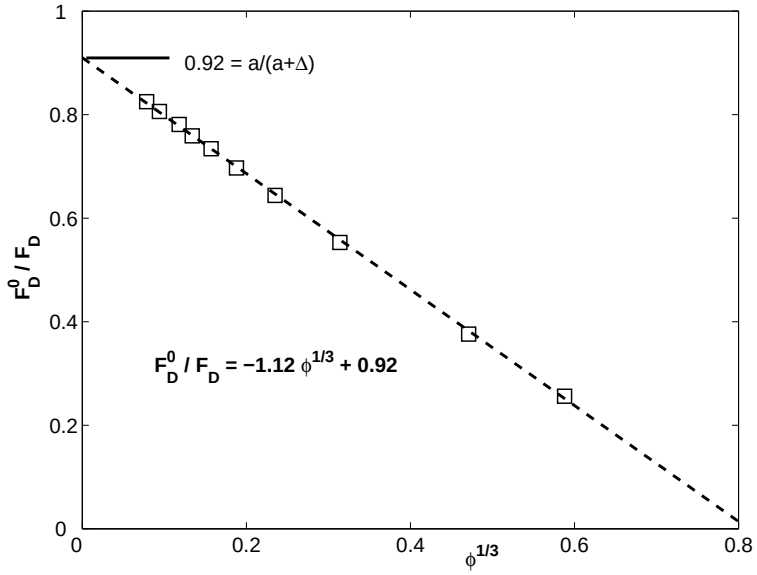

Figure 4.4: Stokes drag force on a spherical bubble in a cubic array versus volume fraction for a bubble radius $a = 2.92$, and velocity $U = 10^{-4}$. F_D^0 is the Stokes drag force on an isolated bubble. The dashed line is a linear fit to the simulation data.

average of four or five runs with each run using a randomly chosen position. The standard deviation in these runs relative to the mean value was 1% for the smallest bubble size and decreased with increasing resolution. Fig. (4.4) shows that the simulations produce the correct $\phi^{1/3}$ scaling, with only a small deviation at the highest simulated volume fraction, due to the higher order terms in Eq. (4.32).

Fig. (4.4) indicates that for a radius of 2.92, the respective relative error in the values of the slope and the intercept with the y axis is 5% and 8%. However, the accuracy can be improved considerably by a calibration process similar to that used in Ladd's solid particle simulations [71]. This calibration process compensates for the fact that the link-bounce-back rule in Eq. (4.10) is only first-order

accurate if the interface is not aligned with a lattice symmetry direction, resulting in a hydrodynamic boundary that is displaced from the physical boundary by an amount that depends on the orientation angle of the interface [40, 41]. For an object with a curved interface such as a sphere, it is not possible to derive an analytical expression for the position of the hydrodynamic boundary. However, one can interpret the results in terms of the "effective" or "hydrodynamic" radius $a_H = a + \Delta$ rather than the input radius a [see Fig. (4.5)], such that the drag coefficient on an isolated particle is identical to its theoretical value [45]. Ladd and Verberg [76] showed that this leads to approximate second order accuracy in the lattice resolution and a reduction of the error in the drag force of approximately an order of magnitude. Furthermore, they found that Δ depends only on the particle radius and the fluid viscosity and not on the particle volume fraction, flow conditions or Reynolds number, making it a well-defined physical parameter that can be obtained in a single calibration simulation.

The similarity between the link-bounce-back rule and our new boundary rule for a fluid-gas interface suggests that calibrations for spherical bubbles can be carried out in a similar way. Hence, we determined a_H, such that the Stokes drag force on a bubble in a cubic array of bubbles reduces in the dilute limit to its value for an isolated bubble, i.e. $F_D(\phi \to 0) = 4\pi\eta a_H U$. This implies that a/a_H can be identified with the intercept of $4\pi\eta a U/F_D(\phi)$ with the y axis [see Fig. (4.4)]. In Table 4.2, we summarize the values that were obtained for a range of bubble radii and two viscosities, $\eta = 6.0$ and $\eta = 0.36$.

In Fig. (4.6), we plot the inverse of the ratio between the Stokes drag force on a bubble in a periodic array and that of an isolated bubble versus the bubble volume fraction, both rescaled in terms of the hydrodynamic radius, i.e., $F^0_{D,H} = 4\pi\eta a_H U$

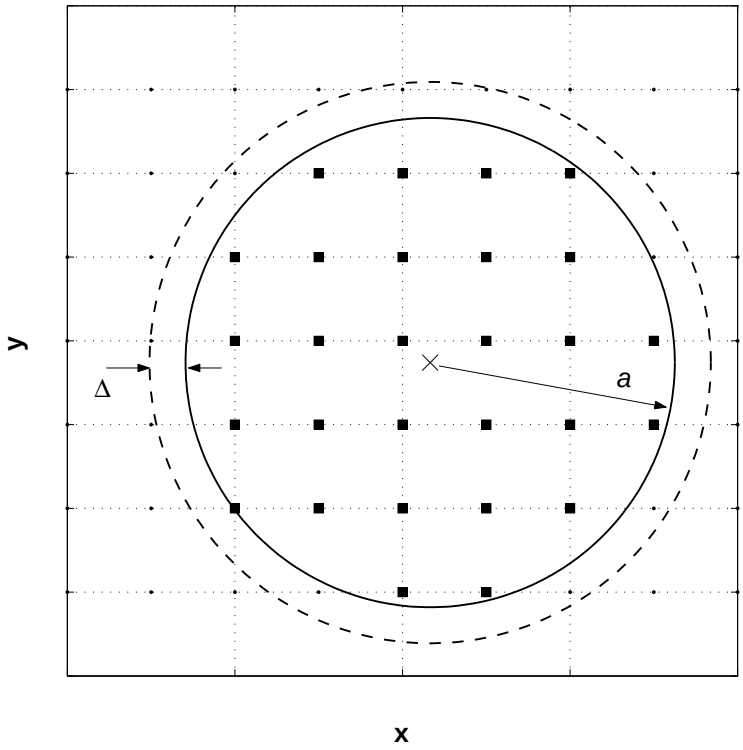

Figure 4.5: A cross-sectional view of a spherical particle or bubble on the lattice-Boltzmann grid. The dots indicate the fluid nodes; the nodes inside the particle or bubble are marked by squares. The solid line is the interface for the input radius a, and the dashed line that for the hydrodynamic radius $a_H = a + \Delta$.

Table 4.2: The hydrodynamic radii $a_H = a + \Delta$ for spherical bubbles for varying input radii a and viscosities η.

	$\eta = 0.36$			$\eta = 6.0$			
a	2.92	5.63	9.85	1.57	2.92	5.63	9.85
a_H	3.35	6.07	10.31	1.73	3.17	5.93	10.17
Δ	0.43	0.44	0.46	0.16	0.25	0.30	0.32

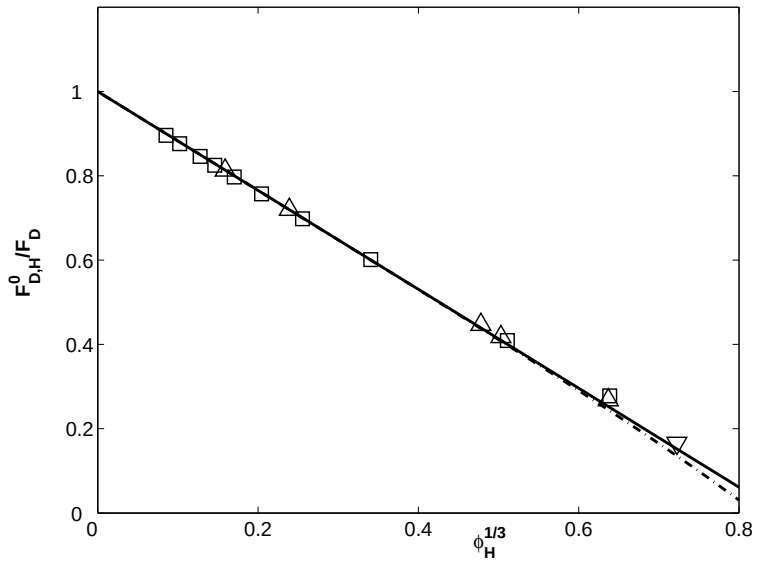

Figure 4.6: Stokes drag force on a spherical bubble in a cubic array versus volume fraction ϕ_H rescaled in terms of the hydrodynamic radius. $F^0_{D,H}$ is the rescaled Stokes drag force on an isolated bubble. The lines are Sangani and Acrivos' theoretical prediction [114] [see Eq. (4.33)]. The solid line is their result up to order $\phi_H^{1/3}$; the dash-dot line includes the ϕ_H^2 term. The symbols are the simulation results for: $a_H = 3.17$ ($\square$), $a_H = 5.93$ ($\triangle$), and $a_H = 10.31$ ($\bigtriangledown$). The viscosity and bubble velocity are $\eta = 6.0$ and $U = 10^{-4}$.

and $\phi_H = 4\pi a_H^3/3L^3$, with L being the size of the computational domain. The simulation results are now in excellent agreement with Eq. (4.32).

4.4.3 Moderate Reynolds number flow around an isolated spherical bubble

The acceleration and steady rise of an isolated spherical bubble outside the creeping flow region have been studied extensively in the literature [24, 67, 134, 91, 85, 103].

They provide therefore excellent opportunities to determine the accuracy of the method in the moderate Reynolds number regime.

First, we briefly review the relevant results from previous work. We start with the drag force on a steadily rising bubble since it is easily measured and thus much better known than the forces on accelerating bubbles. When documenting the steady state drag force on a spherical bubble, one usually expresses the results in terms of the dimensionless drag coefficient C_D,

$$C_D = \frac{F_D}{\frac{1}{2}\rho U_T^2 \cdot \pi a_H^2} \ , \tag{4.34}$$

and the Reynolds number $Re = (2\rho U_T a_H)/\eta$ based on the terminal velocity U_T. As the hydrodynamic correction improves the accuracy of the lattice-Boltzmann method, the hydrodynamic radius a_H, rather than the input radius a, is used consistently in this section. In the Stokes flow region, C_D and Re are related by

$$C_D = \frac{16}{Re} \ , \quad Re \ll 1. \tag{4.35}$$

For small but finite Re, Kumagai [67] derived the Oseen correction to the Stokes flow result:

$$C_D = \frac{16}{Re}\left(1 + \frac{Re}{8}\right) \ , \tag{4.36}$$

which is found to agree reasonably well with the experimental results up to $Re \approx 1$ [67]. For higher Reynolds numbers, Clift, Grace and Weber [24] suggested the following correlation:

$$C_D = 13.725 Re^{-0.74} \ , \quad 4 < Re < 100. \tag{4.37}$$

Finally, when Re is very large while the bubble remains spherical with the wake confined to a small region, we can assume potential flow in the entire fluid except for

a thin boundary layer surrounding the bubble. The drag can then be determined analytically [94]:

$$C_D = \frac{48}{Re}\left[1 - \frac{2.21}{Re^{1/2}} + O\left(Re^{-5/6}\right)\right] \quad , \qquad Re \gg 1. \tag{4.38}$$

The determination of the force on an accelerating spherical bubble is a much more difficult problem. To evaluate this force one must consider, in addition to the current acceleration, which gives rise to an added mass force, the forces due to the previous motion of the bubble. The latter contribution, known as the history integral, captures the effects of the transport and decay of the vorticity produced at the gas-liquid interface. Yang and Leal [134] first evaluated the history integral and derived the unsteady force on an accelerating spherical bubble in the creeping flow limit. Lovalenti and Brady [85] later used an Oseen point force and the reciprocal theorem to derive the unsteady force for small but finite Reynolds numbers. Based on numerical simulations and asymptotic analysis [90, 89], Mei *et al.* [91] proposed a semi-analytical expression for the kernel of the history integral for a spherical bubble for $Re > 1$. The history integral was later used in a set of equations (Park *et al.* [103]) which predicts both the unsteady acceleration and the steady state velocity of spherical bubbles for $0 < Re < 300$. We compare our simulation results with the prediction of this set of equations. Since these equations are in rather lengthy forms, they are not included here. One can refer to Park *et al.* [103] for more details.

The lattice-Boltzmann simulations of rising bubbles in a fluid with inertia are set up differently from the creeping flow simulations in the previous section because we want to study the transient acceleration of the bubble as well as the final steady state drag force. Moreover, at finite Reynolds numbers we can no longer assume

the flow to be quasi-steady, so it would be erroneous to give the bubble a constant velocity without accounting for the change in the bubble position. Thus, we took a more physical approach of releasing the bubble from a stationary position and letting it rise as a result of its buoyancy force. As in the previous simulations, a pressure gradient is applied to the fluid to assure that the mean velocity of the simulation cell is zero. Due to the initial imbalance of forces exerted on the bubble, it accelerates until the drag force, which increases with increasing velocity, equals the buoyancy force. Thereafter the bubble rises steadily, with only small fluctuations due to the discreteness of the underlying lattice. Since we cannot use the terminal velocity as an input parameter in these simulations, we use the Archimedes number to characterize our simulations. The Archimedes number, defined as

$$Ar = \frac{8\rho^2 g a_H^3}{\eta^2} \ . \tag{4.39}$$

is independent of the bubble's velocity and characterizes the relative importance of gravitational (or buoyancy) forces and viscous forces.

The simulations were carried out in a cubic domain of dimension L with periodic boundary conditions. We used six Archimedes numbers, chosen such that they give Reynolds numbers of approximately 1, 2, 5, 10, 20, and 30. To determine whether the finite cell influenced the results, we used three values of L for each Archimedes number. To allow the bubble to sample all points relative to the lattice, the simulations were repeated five to seven times with different orientations of the buoyancy force relative to the axes of the lattice. We avoided directions that were close to one of the primary lattice directions, since the drag force on a periodic array of bubbles is very different when the bubble is in the wake of its periodic images [62, 48, 49].

The acceleration of the bubble is shown in Fig. (4.7), where the bubble velocities are plotted as functions of time for a range of Archimedes numbers and the system size $L/a_H = 23.88$. The velocities are normalized by the terminal velocity for each run, so that they all approach unity for $t \to \infty$. The time is non-dimensionalized with $\rho a_H^2/\eta$. The simulation results are in good agreement with the predictions computed from the equations in Park *et al.* [103] for the four highest Archimedes numbers and the agreement is still reasonably good for $Ar = 27.0$ ($Re \approx 2$). At this lower Reynolds number, the velocity disturbance produced by the periodic images of the bubble propagates over a large enough distance so that the hydrodynamic interactions between a bubble and its periodic images cannot be ignored. This leads to a relatively faster convergence to U_T than predicted by Park *et al.* [103]. This effect becomes less important as either the system size or the Reynolds number is increased. Indeed, there is no significant difference between the acceleration of bubbles with higher Archimedes numbers observed in cells of size $L/a_H = 18.93$ and $L/a_H = 23.88$. As the Archimedes number decreases, the time required for the bubble to reach its terminal velocity increases and the acceleration gradually approaches the creeping flow limit of $Re \ll 1$. However, to accurately resolve the creeping flow behavior in a simulation of this kind would require a very large computational domain, because the final approach of the bubble velocity toward its terminal velocity is governed by momentum diffusion over very large distances.

We calculate Re and C_D from U_T and F_D, after the bubbles reach their terminal velocities. The results are summarized in Table 4.3. For the two lowest Archimedes numbers ($Ar = 13.7$ and 27.0), the system size still has a noticeable effect on the results. For the higher Archimedes numbers, however, the results are virtually independent of system size for the range of L/a_H studied. For $Re < 10$, a bubble

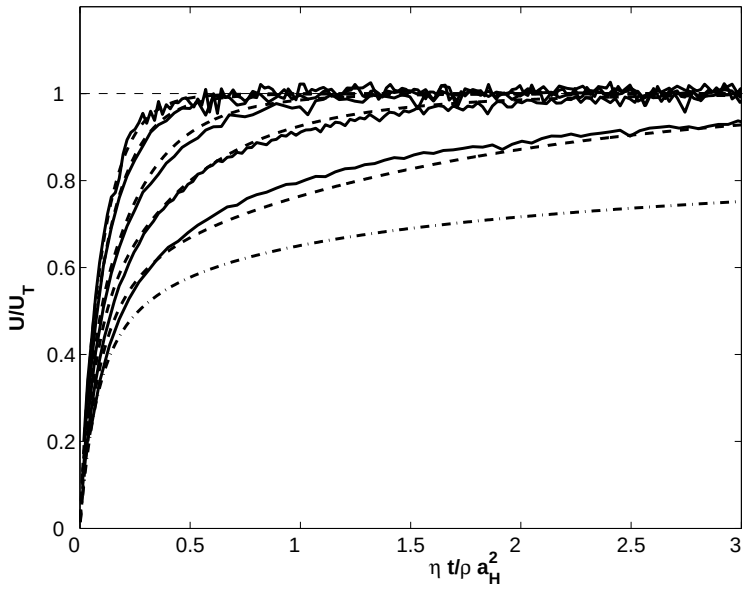

Figure 4.7: The transient motion of spherical bubbles rising due to buoyancy for $L/a_H = 23.88$. The solid lines are obtained from simulations and the dashed lines are calculated using the equations given by Park *et al.* [103]. From upper left to lower right, the Archimedes numbers are 748.9, 451.1, 197.9, 87.8, and 27.0, corresponding to Reynolds numbers in the range $2 < Re < 28$. The dash-dotted line represents the creeping flow limit [134].

radius as small as $a_H = 3.35$ is sufficient to keep the accuracy within $\pm 3\%$. As Re is increased beyond 10, however, a larger lattice resolution is necessary to maintain the accuracy. In Fig. (4.8), one can see that the simulation results, plotted as C_D versus Re, agree well with Eqs. (4.35), (4.36), and (4.37). The highest Reynolds number that we studied is still well below the lowest Reynolds number for which Eq. (4.38) applies, however, the simulations show a correct trend toward Eq. (4.38) with increasing Re.

Table 4.3: The drag coefficients and terminal Reynolds numbers of bubbles for a range of Archimedes numbers. The two columns in the center are the simulation results with the numbers in the brackets representing the standard deviations of successive runs with different orientations. The last two columns are the steady state values calculated from the equations given in [103]. All simulations were carried out with a bubble radius $a_H = 3.35$ and a fluid viscosity $\eta = 0.36$ except for: i) $a_H = 3.17$ and $\eta = 6.0$ (result is viscosity independent), and ii) $a_H = 6.07$ and $\eta = 0.36$ (for $Re > 10$ larger radius gives more accurate results).

Ar	L/a_H	Re	C_D	Re	C_D
	11.94	0.943 (0.005)	20.6 (0.2)		
13.7	17.92	0.992 (0.004)	18.6 (0.2)	1.037	17.0
	23.88	1.010 (0.005)	17.9 (0.2)		
13.8[i]	18.93	0.996 (0.003)	18.5 (0.1)	1.040	17.0
	11.94	1.81 (0.02)	11.0 (0.2)		
27.0	17.92	1.852 (0.004)	10.52 (0.04)	1.92	9.76

Continued on next page...

Table 4.3 – (continued)

Ar	L/a_H	Re	C_D	Re	C_D
	23.88	1.89 (0.02)	10.1 (0.2)		
	11.94	5.09 (0.09)	4.52 (0.16)		
87.8	17.92	5.23 (0.05)	4.28 (0.08)	5.35	4.10
	23.88	5.26 (0.03)	4.23 (0.05)		
	11.94	10.0 (0.1)	2.64 (0.07)		
197.9	17.92	10.22 (0.06)	2.53 (0.02)	10.54	2.38
	23.88	10.22 (0.08)	2.53 (0.01)		
198.6[ii]	13.18	10.3 (0.1)	2.51 (0.06)	10.57	2.37
	19.77	10.46 (0.04)	2.42 (0.02)		
	11.94	18.8 (0.1)	1.69 (0.02)		
451.1	17.92	19.1 (0.1)	1.65 (0.02)	20.9	1.38
	23.88	19.4 (0.1)	1.60 (0.02)		
	11.94	27.6 (0.4)	1.31 (0.04)		
748.9	17.92	27.9 (0.5)	1.28 (0.05)	31.9	0.98
	23.88	28.1 (0.5)	1.26 (0.05)		
747.9[ii]	13.18	29.4 (0.2)	1.16 (0.02)	31.8	0.98
	19.77	29.81 (0.05)	1.122 (0.004)		

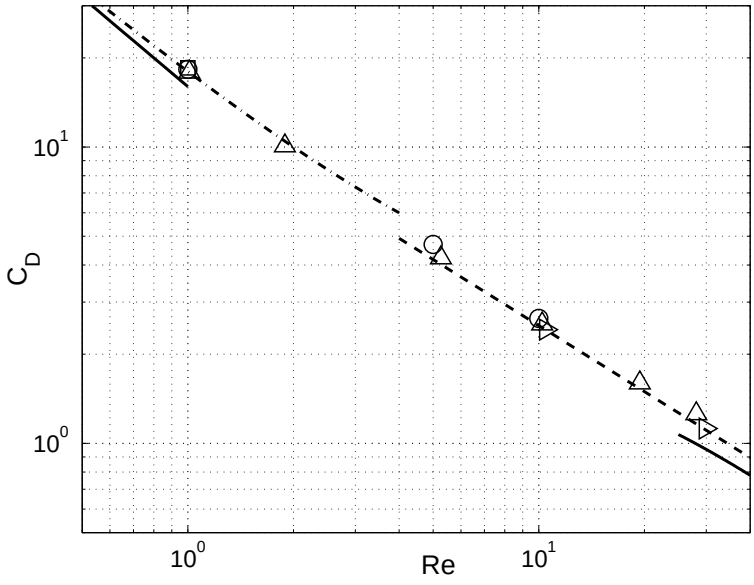

Figure 4.8: Drag coefficient C_D as a function of the Reynolds number. The symbols represent the simulation data. For clarity, for a given Ar only the largest L/a_H data are shown. The viscosity is $\eta = 0.36$ unless otherwise mentioned. ($\triangle$): $L/a_H = 23.88, a_H = 3.35$; ($\triangleright$): $L/a_H = 19.77, a_H = 6.07$; ($\square$): $L/a_H = 18.93, a_H = 3.17, \eta = 6.0$; ($\circ$): experimental measurements of deformable bubbles, cited in [24]. The solid line in the upper left corner represents the Stokes drag Eq. (4.35), the dash-dotted line is the Oseen solution Eq. (4.36), the dashed line the correlation Eq. (4.37), and the solid line on the lower right corresponds to Moore's solution for high Re Eq. (4.38).

4.5 Summary and Discussion

In this chapter, we presented a new lattice-Boltzmann boundary rule for a fluid-gas interface. The new rule recovers the free-slip boundary condition by modelling a bounce-back process for populations that cross the interface, which enforces a zero normal relative velocity and zero tangential stress condition at the fluid-gas interface. A two-dimensional test for flow driven by an impulsively started plate with a free surface above showed that the rule accurately accounts for both steady and unsteady flows near a flat interface.

This new lattice-Boltzmann model is an ideal tool to simulate a special class of multiphase flows involving nearly spherical, non-coalescing bubbles. By treating the bubbles as spheres with a free-slip boundary condition imposed on the surface, we only need to simulate the flow in the continuous phase. Numerical tests of flows around three-dimensional bubbles showed that our model can accurately solve transient and steady flows around spherical bubbles for Reynolds numbers in the range $0 < Re < 30$. Hence, our model allows for efficient simulation of bubbly suspensions in the intermediate Reynolds number regime, making it possible to bridge the gap in between previous studies of purely viscous and purely inertia-dominated flows [93, 5, 115, 141, 9, 137, 57, 121, 138].

Compared with bubble simulations that use two immiscible fluids, the direct simulation of the free-slip boundary condition offers several advantages. First, neglecting the gas component reduces the computational cost. Second, the numerical difficulty of employing two fluids with vastly different densities and viscosities can be avoided. Third, the complex geometry associated with moving interfaces can be treated with relative ease due to the simple nature of the single-component

lattice-Boltzmann bounce-back rule. Although we limited ourselves in this work to spherical bubbles, the new boundary rule applies equally well, and without modifications, to other shapes. Furthermore, after coupling our method to a correct surface tension model, the new boundary rule may be used to simulate deformable bubbles in the future.

While we did not carry out systematic studies on the stability of the algorithm, we found that the planar flow example is remarkably stable. A stable solution was obtained even at $\eta = 0.012$, which was the lowest viscosity tested. There were no signs of numerical instability for the three-dimensional bubble simulations at the dynamic viscosity 0.36 used for those studies.

Because a molecule undergoing a specular reflection from a surface experiences no change in its tangential momentum, it would be natural to consider developing a no-tangential stress boundary condition based on specular reflection. Indeed, there are a couple of papers on rarefied gas flows in microchannels, where a hybrid scheme of specular reflection and regular bounce-back was applied on a stationary, planar interfaces to simulate the partial velocity slip due to finite Knudsen number effect [84, 122, 142, 143]. We also tested such an approach during the early stages of our study. However, in practice we found specular reflection only works when the interface is aligned with the lattice directions, such as the planar flow example discussed in 4.4.1, and does not maintain a stationary solution near an oblique interface.

Consider a special example where there is a slip interface that is aligned with the lattice direction, as illustrated in Fig. (4.9a). Both the interface and the fluid above the interface are at rest, thus everywhere in the fluid the distribution is stationary: $n_i = \rho a^{c_i}$. In the propagation and boundary collision step, the populations that

collide with the interface, n_4, n_7, and n_8, are specularly reflected to 3, 5, and 6 directions. The populations propagated from neighbor fluid nodes now occupy 1, 2, 4, 7, and 8 directions. Since $n_i = \rho a^{c_i}$ is still satisfied, the post-collision distribution n_i^* remains stationary.

When the interface is not aligned with the lattice directions, as shown in Fig. (4.9b), the specularly reflected populations from n_4, n_7, and n_8 are skewed and are no longer in the 3, 5, and 6 directions. Since the velocities of the reflected molecules are not in lattice directions, some scheme is required so that the reflected molecules propagate on the lattice. We required that the molecules return to the same fluid node after the reflection. One can then use the zeroth, first and second moments of the velocity of molecules arriving at the node from the interface and from other fluid nodes in a collision operator for this fluid node. However, such a scheme does not preserve the equilibrium velocity distribution in a fluid at rest in the presence of a stationary interface. In contrast, the bounce-back boundary condition [Eq. (4.24)] developed here is designed specifically to preserve any velocity distribution function that is consistent with the no tangential stress and no normal velocity boundary conditions, irrespective of the angle between the surface normal and the underlying lattice directions.

Similar to the link-bounce-back rules for solid-liquid interfaces, the new boundary rule always assumes that the gas-liquid interface is represented by boundary nodes that are halfway between gas and fluid nodes. More accurate representations of the boundary can be obtained either via volumetric approaches [16, 18, 128, 129] or interpolations [92, 7, 77]. Among others, Bouzidi et al. [7] have proposed an improved bounce-back method based on interpolation to impose the slip boundary condition at an arbitrary distance from a fluid node instead of 1/2. In general,

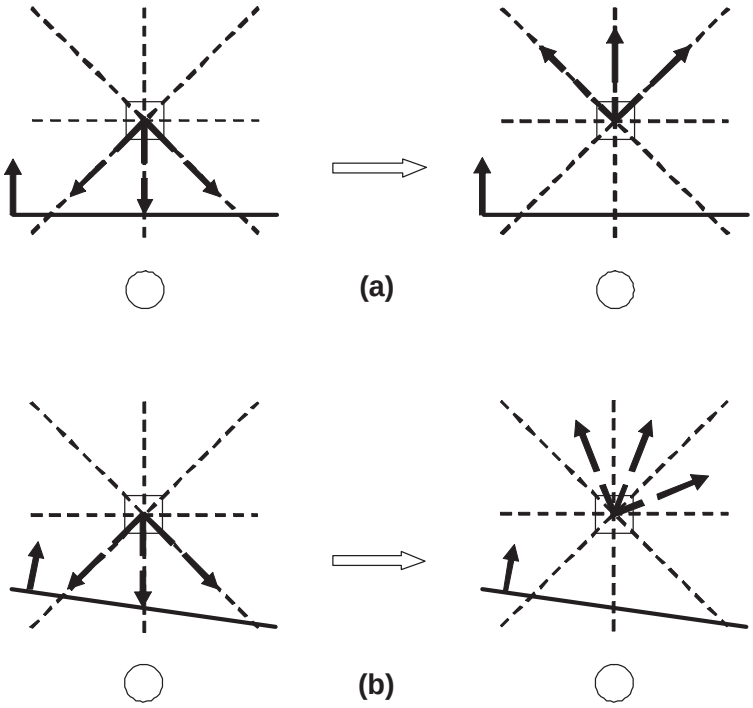

Figure 4.9: Specular reflection of populations near a) an interface aligned with a lattice direction, b) an oblique interface not aligned with any lattice directions. (□) represents a fluid node and (○) represents a node outside fluid. The thick solid line between the two nodes is the interface with an arrow representing the surface normal. The populations that collide with the interface are represented by the dashed arrows. They follow Table 4.1 and satisfy $n_i = \rho a^{c_i}$. The short dashed lines represent the lattice directions. In b), the reflected populations are skewed. The zeroth, first, and second moments of the reflected populations do not preserve the stationary solution $n_i = \rho a^{c_i}$ near an oblique interface.

when the interface is not located at 1/2 positions, the populations that start at fluid nodes and collide with the interface will not be bounced back to the original nodes. Thus, to prepare for the collision step, it is necessary to calculate the populations at the original nodes via linear or quadratic interpolations. Since our method for slip boundary condition is a special type of bounce-back rule, it is possible to use ideas similar to those developed in [7] to derive rules to improve the spatial accuracy. However, such an interpolation would always require additional information, such as the surface normals and the positions where the interface cuts the lattice links, making the method substantially more complicated. The determination of these structural parameters in an evolving geometry such a bubble suspension would incur substantial computational costs.

Chapter 5

Rise Velocity and Microstructure in Finite Re Bubble Suspensions

5.1 Introduction

Bubble suspensions are of great practical interest, because many engineering applications make use of them to exchange mass or heat between the gas and the liquid phases. Compared with solid particle suspensions, the dynamics of a bubble suspension is more complex, because bubbles are deformable, able to coalesce and break, and have a different type of boundary condition on the gas-liquid interface. The boundary condition is special in that the fluid can "slip" on a bubble surface, which greatly reduces the production and transport of vorticity into the fluid phase. This slip boundary condition not only reduces the drag on a bubble compared to that of a solid particle with the same shape and velocity, it also changes the hydrodynamic interaction between bubbles. As a result, the average properties of a bubble suspension may differ substantially from those of a solid particle suspension. To understand the effect of slip boundary condition on the average properties, it is desirable to study a simple suspension with monodisperse, nearly spherical and non-coalescing bubbles rising under the influence of gravity, where the effect of slip boundary condition can be isolated and interpreted without ambiguity. In this chapter, we present a numerical study of such suspensions.

In particular, we characterized the rise velocity, the microstructure in unbounded suspensions, and the flow profiles in wall-bounded vertical channels.

In our simulations, the bubbles are rising with moderate Reynolds numbers. Here the Reynolds number is defined as $\mathrm{Re} = \rho d u_t/\eta$, where ρ is the fluid density, η is the fluid viscosity, d is the bubble diameter, and u_t is the terminal velocity. Re defined this way measures the level of inertia on the bubble length scale. For a suspension of monodisperse, spherical, non-coalescing bubbles, it is possible to derive the averaged equations of motion from first principles, provided that the Reynolds number is either negligibly small or very large. In the low Re limit, the non-linear inertial term in the Navier-Stokes equations can be neglected and the remaining linear equations can be solved by a multipole expansion method [93]. In the high Re limit, Moore [94, 95] points out that the flow around a high Re bubble is vorticity-free except in a thin boundary layer near the bubble surface. The velocity field outside the boundary layer can thus be regarded as the gradient of a velocity potential. The velocity potential obeys linear equations and can also solved the multi-pole expansion method. Moore's prediction of bubble drag based on the potential flow theory has been verified experimentally by Duineveld [33]. And there are a number of theoretical and numerical studies on the average properties of high Re bubble suspensions developed from the potential flow approximation [5, 115, 141, 9, 137, 57, 121]. In the intermediate Re regime, however, we cannot ignore the non-linear inertial term; nor can we make use of the potential flow approximation to simplify the equations. It is generally believed that the best way to study the average properties of such suspensions is to conduct direct numerical simulations. For this reason, in this study we focus on suspensions with moderate Reynolds numbers: $5 < \mathrm{Re} < 20$. The range of volume fraction ϕ is 1% - 25%.

A suspension of spherical and non-coalescing bubbles is also experimentally relevant. It is well-known that the dynamics of a bubble is determined by its Eötvös number $\mathrm{Eo} = \rho d^2 g/\sigma$, and the Morton number $\mathrm{Mo} = g\eta^4/\rho\sigma^3$, where σ is the surface tension coefficient. Based on the empirical bubble deformation regime presented in the book by Clift, Grace, and Weber [24], both Eo and Mo must be small to ensure that the bubble is rising with a finite Reynolds number yet still remains nearly spherical. When Eo and Mo are small, surface tension is irrelevant and Re alone is sufficient to characterize the motion of bubbles. In recent experimental studies, Zenit *et al.*[138, 140] produced such suspensions by using a combination of tiny capillaries (0.1 mm ID) and a magnesium sulfate solution. The tiny capillaries ensure that the bubbles are small; the magnesium sulfate, on the other hand, produces a hydration force between interfaces and suppresses the coalescence of bubbles. The resulting bubble suspensions are highly monodisperse up to 15% volume fraction. The bubbles are about 1.5 mm in size, have high Reynolds numbers (~ 200) and moderate deformations (aspect ratio $1.2 \sim 1.5$). Unlike surfactants, which are also capable of suppressing bubble coalescence, electrolytes do not produce Marangoni stresses on gas-liquid interfaces and the slip boundary condition on the gas-liquid interface can be preserved.

Due to the high computational cost involved, it is only recently that direct numerical simulations of a suspension of freely rising, three-dimensional bubbles have become available. Esmaeeli and Tryggvason first simulated the rise of 8 three-dimensional bubbles that are rising with finite Reynolds numbers in periodic domains [34, 35]. Based on the same methodology, Bunner and Tryggvason simulated larger systems on parallel computers and characterized the rise velocity, microstructure, and fluctuations in finite Re bubble suspensions for the first time

[10, 11]. The largest system in their works contains 216 slightly ellipsoidal bubbles and the Reynolds number based on the terminal velocity is about 30. Their numerical method is based on a finite difference scheme with front tracking. In this method, there are two fluid components and they are separated by sharp interfaces, the positions of which are determined by the balance between nearby fluid stresses and the surface tension, and are tracked throughout the simulation. The fluid component inside the interface has a much smaller density and viscosity such that the behavior of the fluid particle approximates the behavior of a gas bubble. Thus, their method is capable of simulating deformable bubbles. When two bubbles collide, the coalescence is prevented by simply not allowing the interfaces to merge. More recently, this method is modified such that bubbles with higher Reynolds numbers [$O(100)$] can be simulated [36].

Bunner and Tryggvason's simulations [10, 11] are perhaps the most realistic to date. However, for nearly spherical, non-coalescing bubble suspensions it is possible to use a more efficient methodology to reduce the complexity of simulations and the computational cost. When bubbles are nearly spherical, the deformation does not have a significant effect on the dynamics of the suspension. It is very convenient, then, to neglect the deformation completely and approximate the bubbles as spheres with slip boundaries. In a recent paper by Yin *et al.*[135], a boundary rule for a lattice-Boltzmann fluid was developed such that the slip boundary condition on gas-liquid interfaces can be simulated, and this boundary rule was immediately applied on a sphere to simulate flows past a spherical bubble. Numerical tests show that the method is very accurate in the range $0 < \mathrm{Re} < 30$. This method is more efficient than Bunner and Tryggvason's method, because the Navier-Stokes equations is only solved for the flow in continuous phase, and it is

no longer necessary to track a deforming bubble interface. The motions of the bubbles are determined through a force balance between a surface integral of fluid stresses and the buoyancy. In this work, this lattice-Boltzmann method is used to simulate the motions of many monodisperse, spherical, and non-coalescing bubbles rising under the influence of gravity. When bubbles collide with each other, based on a study by Tsao and Koch [127] where it is found that collisions between slightly deformable bubbles are nearly elastic, we assumed elastic collisions in our simulations. The efficiency of our lattice-Boltzmann method allows us to simulate up to a thousand bubbles on a single computer. And we can run the simulations for relatively long times to obtain accurate statistics.

We simulated the rise of bubbles in computational domains that are either periodic in all directions, or bounded in one of the horizontal directions by a pair of solid walls. From simulations in periodic domains, we obtained the rise velocities as functions of Re and ϕ, and characterized the microstructure of the suspension by presenting the pair probability density distributions. In suspensions of solid particles, the average settling velocities can be expressed as simple power-law functions of $1-\phi$ [110, 39]. For suspensions of rising bubbles, however, the available empirical formula is not in a simple power-law form [53]; simulation results by Bunner and Tryggvason [10] also indicate that the rise velocity does not fit well to a power-law function of $1-\phi$ when Re $\sim$ 30. Compared with Bunner and Tryggvason's simulations, our simulations are with lower Reynolds numbers. It is generally expected that the difference between bubble and solid particle suspensions will be larger at higher Re due to the potential flow behaviors. Thus, it is of interest to check whether the rise velocities in the lower Re bubble suspensions will fit well to simple power-law functions of $1-\phi$.

On the microstructure in bubble suspensions, there has been many experimental and numerical evidences indicating that freely rising bubbles tend to align on a horizontal plane and form clusters or rafts [138, 15, 10, 36]. When Re is $O(10)$, both Cartellier and Rivière's experiments [15] and Bunner and Tryggvason's simulations [10] find moderate accumulation of bubbles in a horizontal plane. When Re is $O(100)$, Esmaeeli and Tryggvason [36] find from numerical simulations that the size of the cluster grows with increasing Re. In the experiments by Zenit *et al.*[138], horizontal clusters have also been found, although they are not as strong as in Esmaeeli and Tryggvason's simulations, which is possibly due to the finite deformation of the bubbles [36].

It is generally believed that this strong preference for the side-by-side orientation among freely rising bubbles comes from the anisotropic inertial interaction between pairs of bubbles. When Re is small but finite, the interaction is driven by wakes and is more of a drafting-kissing-tumbling type [37, 10, 87, 80], similar to the interaction between a pair of solid particles. When Re is large, the bubbles interact with each other through the velocity potentials, and they attract each other in the horizontal direction and repel each other in the vertical direction as if they were dipoles [133, 5, 68, 65, 66, 80]. Numerical simulations of high Re spherical bubbles interacting with each other by potentials [115] show that the potential flow interaction eventually leads to the formation of a single dense cluster. The clusters observed in high Re experiments [138] and simulations [36], on the other hand, are not as strong and it is suspected that the finite viscosity plays a role in breaking up the clusters. In our simulations, we have suspensions that are more viscous. It is worthwhile, then, to characterize the microstructure and check the level of clustering in such suspensions.

We also simulated the bubbly flow in a vertical channel and studied the interaction between walls and a suspension of bubbles. The interaction between a vertical wall and a rising spherical bubble nearby has been studied in great detail [124, 123, 86]. It is found that when Re < 30 the bubble is repelled from the wall, driven by the interaction between the inertial wake generated behind the bubble and the wall; when Re > 30, the bubble is attracted toward the wall instead, due to the potential flow interaction between the bubble and its wall image. In this work, we are interested in the effect of walls on the steady-state volume fraction and flow profiles in a vertical channel. Our Reynolds numbers are less than 20, so bubbles are always pushed away from the walls. The resulting non-uniform distribution of bubbles can affect the average flow profile through buoyancy effects. The flow profile, in turn, can modify the distribution of bubbles through convective motions and lift forces. Clearly, this close coupling between the volume fraction and flow profiles can only be solved accurately via numerical simulations.

This chapter is organized in the following order. In Section 5.2, we introduce the numerical method and explain how the simulations were set up; in Section 5.3, we show the average rise velocities obtained in our simulations as functions of Re and ϕ; in Section 5.4, we present the microstructure in the suspensions and discuss the mechanism; finally, in Section 5.5, we study the effect of walls. A summary is presented at the end.

5.2 Lattice-Boltzmann method

The lattice-Boltzmann method used in this work is originally developed by Ladd [71, 72] for a suspension of spherical particles. It was later supplemented with a

new boundary rule by Yin *et al.*[135] such that the slip boundary condition on gas-liquid interfaces can be simulated. Since this method has been described in detail in [135], here we will only give a condensed description.

The lattice-Boltzmann method is different from most conventional computational fluid dynamics routines in that it is not a direct solver of the Navier-Stokes equation. Rather, it uses a simplified kinetic model to simulate the evolution of a fluid molecular velocity distribution on a simple cubic lattice that fills the entire computational domain. The macroscopic quantities, such as density, momentum, and stress, are the zeroth, first, and second order moments of this molecular velocity distribution function. The evolution of the molecular velocity distribution occurs by two steps: propagation and collision. In the propagation step, the molecular population on a node is divided into fractions according to the current molecular velocity distribution, and these fractions travel along the lattice links to neighboring nodes based on their velocities. In the collision step, the populations that arrived in the propagation step undergo a collision, the rule of which is designed to conserve mass and momentum and recover the Navier-Stokes equation on the macroscopic scale, and a new set of populations are generated for the next propagation step. In our lattice-Boltzmann model, the molecular velocity distribution consists of 19 velocities, which correspond to the populations that are stationary during the propagation step ([000]), and the populations that move to the nearest ([100]) and next nearest ([110]) neighbors in one time step. The isothermal speed of sound in our system is $c_s = 1/\sqrt{3}$. This lattice-Boltzmann model recovers the Navier-Stokes equation in the limit of small Mach number $M = u/c_s \ll 1$, where u is a characteristic velocity, with an error of order M^2 [76]. In our simulations, M was kept below 0.1, which requires u to be a fairly small quantity. However,

by using a combination of low viscosity and relatively large bubble radii, an order $O(10)$ Reynolds number can still be reached. In this work, the density of the lattice fluid $\rho = 36$ and the viscosity η is between 0.36 - 0.72.

In a two-phase system, some of the lattice nodes belong to the continuous liquid phase and other nodes belong to the dispersed phase, gas or solid. In our method, the lattice-Boltzmann steps are only carried out on the liquid nodes. Thus, molecular populations that propagate from a liquid node to a non-liquid node must be treated in some way to conserve the fluid mass and recover the boundary condition. We are using a link-bounce-back rule developed by Yin *et al.*[135], where the slip boundary condition is recovered half-way between the liquid and the non-liquid nodes, with a relative error that is first-order in the spatial discretization [135]. By using an effective diameter, which can be obtained by calibrating the Stokes drag of a simple cubic array, approximate second-order accuracy can be achieved [135]. In this work, we used two different bubble sizes. The smaller bubbles have an effective diameter of $d = 6.70$ and the larger ones have $d = 12.14$. The larger bubbles were only used in validation runs to check whether the numerical results depend on the lattice resolution. It was found from those runs that $d = 6.70$ is sufficiently accurate for the range of Re and ϕ that we study. Thus, in all the results presented in the following sections $d = 6.70$.

This lattice-Boltzmann method allows us to approximate bubbles as spheres with slip boundaries and use a single-component lattice-Boltzmann solver to simulate the flow in the continuous phase. The motions of bubbles are determined by the balance between the hydrodynamic forces and the bubble's buoyancy. The bubbles have a density that is 0.001 times that of the fluid such that the equations of motion for the bubbles are stable. This density ratio is comparable to the den-

sity ratio of an air bubble in water under standard atmospheric conditions. When bubbles bounce into each other, elastic collisions are assumed. In the simulation of solid particle suspensions, it is often necessary to impose an explicit lubrication correction to recover the lubrication interaction between close pairs of solid particles [97]. In our simulations of bubble suspensions, there is no need to implement such corrections because bubbles do not have strong lubrication interactions [58].

In Sections 5.3 and 5.4, the computational domains are cubic in shape and are surrounded by periodic boundaries. In Section 5.5, as we are interested in the effect of walls, we used rectangular-shaped domains, with a pair of solid walls in the y direction. In the settling direction (x direction) and another perpendicular direction (z direction) periodic boundaries were assumed.

All simulations start with a random configuration of N bubbles with zero initial velocities. Once the simulations start, the bubbles accelerate until the net hydrodynamic drag balances the total buoyancy. Meanwhile, a reverse pressure gradient is applied to the liquid phase such that the net flow rate of the liquid phase is zero, as would happen in a bubble column with a stationary free surface.

As in our simulations the surface tension σ is irrelevant, it is more convenient to use the Archimedes number, defined as the ratio of the buoyancy to the viscous force

$$\mathrm{Ar} = \frac{\rho^2 g d^3}{\eta^2} \ , \tag{5.1}$$

as the dimensionless form of the buoyancy. Since Ar is independent of the terminal velocity u_t, it is more convenient to use Ar as an input parameter to characterize our simulations. When Ar is known, the terminal velocity of a bubble is uniquely determined. In fact, one can use the empirical relation between the drag coefficient of an isolated spherical bubble and its Reynolds number to calculate the terminal

velocity of a bubble. The drag coefficient C_D is defined as

$$C_D = \frac{8F_D}{\rho u_t^2 \pi d^2} \ , \tag{5.2}$$

where F_D is the hydrodynamic drag acting on the bubble. When a bubble is rising with its terminal velocity, $F_D = \rho g \pi d^3/6$. Thus, C_D is related to Ar and Re by

$$C_D = \frac{4}{3}\frac{\mathrm{Ar}}{\mathrm{Re}^2} \ . \tag{5.3}$$

For a spherical bubble that is moving with a finite Reynolds number, Clift *et al.*[24] have suggested the following correlation between C_D and Re:

$$C_D = 13.725\mathrm{Re}^{-0.74} \ , \quad 4 < \mathrm{Re} < 100 \ . \tag{5.4}$$

Combine Eqs. (5.3) and (5.4) and one can obtain

$$\mathrm{Re} = 0.1572\mathrm{Ar}^{0.794} \ , \quad 4 < \mathrm{Re} < 100 \ . \tag{5.5}$$

In this work, Ar is chosen to be 87.8 and 451.1. The corresponding Reynolds numbers based on Eq. (5.5) are 5.48 and 20.1.

The duration of the simulations, measured by the dimensionless time $t^* = tu_t/d$, varies between 500 and 900. Usually, it takes less than 1/4 of the total simulation time to reach the steady state. The final 1/2 of the record is then used for statistics. For each combination of Ar and ϕ, we run 4 to 5 simulations with different initial configurations, the statistical variations of which were found to be very small — the standard deviation is less than 2% of the mean for the average rise velocity and 7-8% of the mean for the pair probability distribution functions and it decreases further with increasing system size.

From time to time, we will compare the rise velocity and microstructure in bubble suspensions to the hindered settling velocity and microstructure in solid particle

suspensions with comparable Reynolds numbers to show the effects that the slip boundary has on suspension properties. The settling velocities and microstructure in solid particle suspensions were obtained using the lattice-Boltzmann method developed by Ladd [71, 72, 76]. The setup of these solid particle simulations and the procedures to obtain the settling velocity and the microstructure are similar to those in bubble suspension simulations.

5.3 Hindered rise velocities

In this section, we present the hindered rise velocities in a homogeneous suspension of monodisperse, spherical and non-coalescing bubbles as functions of ϕ. It is well known that in a homogeneous suspension the rise velocity decreases with increasing volume fraction, because the fluid has to take tortuous paths to be able to flow through a suspension. Thus, if we normalize the average rise velocity u by the terminal velocity u_t, we will obtain a dimensionless rise velocity $u^* = u/u_t$ whose value is always less than one. Clearly, $u^* \to 1$ when $\phi \to 0$. In our simulations, since the net flow rate of the liquid phase is zero, as in a bubble column with a free surface open to its ambient, the rise velocity u equals the relative velocity u_r between gas and liquid phases. In the studies of fluidization and sedimentation of solid particles or drops, it is often customary to use the drift velocity $u_d = (1-\phi)u_r$, which represents the velocity of the dispersed phase relative to the volumetric center of the mixture. Clearly, the dimensionless form of u_d is $u^*(1-\phi)$.

We used terminal velocities from actual simulations to normalize the rise velocity u and the drift velocity u_d. These single-particle simulations were conducted in large cubic periodic domains. We used three values of L/d to make sure that the

system size L does not have a significant effect on the rise velocity u_t and Re. We also changed the orientation of the gravity vector $\mathbf{g}$ relative to the underlying lattice 6-7 times such that the bubble can sample many different lattice positions as it rises. We avoided using directions that are close to the primary lattice directions so that the motion of the bubble would not be affected by its own periodic image [135]. The rise velocities and Reynolds numbers listed in Table 5.1 are the average of these 6-7 runs, the standard deviation of which seems to decrease with increasing system size. It can be observed from Table 5.1 that the Reynolds numbers obtained from the simulations are in very good agreement with those calculated from Eq. (5.5).

Ishii and Zuber [53] have reviewed a large set of experimental studies and proposed a number of formulae to describe the relation between drag and relative velocity in bubble, drop, and solid particle suspensions in terms of the drift velocity. Substituting our bubble size, liquid density and viscosity, gravity, and terminal velocity into their formula for suspensions of non-distorted bubbles, we have

$$u^*(1-\phi) = \frac{u_d}{u_t} = 1.025\frac{(1-\phi)^3}{1+0.296(1-\phi)^{9/7}} \tag{5.6}$$

for bubble suspensions with Ar = 87.8 and

$$u^*(1-\phi) = 1.450\frac{(1-\phi)^3}{1+0.801(1-\phi)^{9/7}} \tag{5.7}$$

for suspensions with Ar = 451.1.

Fig. (5.1) shows the dimensionless drift velocity $u^*(1-\phi)$ as functions of the volume fraction ϕ. This figure also includes the prediction from Eqs. (5.6) and (5.7), and the hindered settling velocities of monodisperse solid spheres at similar Reynolds numbers. Note that the empirical relation by Ishii and Zuber was proposed for $\phi > 0.05$ suspensions thus it is not surprising that Eqs. (5.6)

Table 5.1: The terminal velocities and Reynolds numbers for bubbles with Ar = 87.8 and Ar = 451.1. The third column shows the terminal velocities in terms of lattice units $\Delta x/\Delta t$. The fourth column shows the Reynolds numbers based on u_t, with the numbers in the brackets representing the standard deviations of successive runs with different orientations. The last column shows the Reynolds numbers calculated from empirical $C_D - \mathrm{Re}$ relation given in [24]. The fluid viscosity is $\eta = 0.72$ for Ar = 87.8 and 0.36 for Ar = 451.1.

Ar	L/d	u_t	Re	Re
	5.97	1.51×10^{-2}	5.09 (0.09)	
87.8	11.94	1.57×10^{-2}	5.26 (0.03)	5.48
	17.91	1.60×10^{-2}	5.35 (0.02)	
	5.97	2.80×10^{-2}	18.8 (0.1)	
451.1	11.94	2.90×10^{-2}	19.4 (0.1)	20.1
	17.91	2.90×10^{-2}	19.4 (0.1)	

and (5.7) do not approach unity when $\phi \to 0$. Nevertheless, our simulation data show good agreement with Eqs. (5.6) and (5.7) when $\phi > 0.10$. Compared with solid particle suspensions with the same Reynolds number, the drift velocity for bubbles decreases less rapidly with increasing volume fraction. Thus, the net drag in suspensions of freely rising bubbles is less than that in suspensions of settling solid particles, which is not surprising since the slip boundary condition on a bubble has less flow resistance than the no-slip boundary condition on a solid sphere.

In homogeneous solid particle suspensions, the drift velocities normalized by the terminal velocities can be expressed as power-law functions of $1 - \phi$, i.e. $u_d/u_t = (1 - \phi)^n$, which is known as the Richardson-Zaki law [110], with the power-law exponent n a function of the Reynolds number[110, 39]. More recent experimental and numerical studies find that in dilute suspensions the drift velocity changes more rapidly with ϕ than the power law predicts [39, 109, 23, 29, 32, 31] (also see Chapter 2). Thus, a modified power law in the form of $u_d/u_t = k(1 - \phi)^n$ was proposed [31] and it provides a better fit for the drift velocity than the original Richardson-Zaki law [31] (also see Chapter 2). The values of k, according to [31], varies in the range 0.8-0.9. In Chapter 2, the values of k was found to be 0.86-0.94.

In homogeneous bubble suspensions, it is generally believed that the drift velocity of bubbles does not fit to a power-law function of $1 - \phi$ as well as the drift velocity of solid particles. The early empirical relations by Ishii and Zuber [53] do not use power-law type formulae to describe u_d in bubble suspensions; Bunner and Tryggvason's simulations also show that the drift velocity u_d in Re $\sim$ 30 bubble suspensions does not fit well to a power-law function of $1 - \phi$. In our simulations, the drift velocity $u^*(1 - \phi)$ does not follow power law very well, either. The deviation of our drift velocities from the best power-law fits can be observed in Fig. (5.2),

where the drift velocities are plotted as functions of $1-\phi$ on a logarithmic coordinate. In the volume fraction range of $0.05 < \phi < 0.25$, the drift velocities for solid particles collapse very nicely onto straight lines. The drift velocities for bubbles, on the other hand, show a small yet noticeable downward curvature and certainly do not fit to straight lines as well as the solid particle drift velocities.

It is known that the microstructure, which characterizes the spatial distribution of the disperse phase in a suspension, can have dramatic effects on the average properties. In solid particle suspensions, the numerical study in Chapter 2 indicates that there is a relation between the microstructure and the drift velocity: when the microstructure is random and isotropic, the drift velocity u_d exhibits a power-law dependence on $1-\phi$; when the microstructure becomes non-random and anisotropic in dilute suspensions ($\phi \leq 0.05$), a deviation of u_d from the power-law can be observed. If this result can be generalized to bubble suspensions, then the fact that the drift velocities in bubble suspensions do not fit well to power laws suggests that finite Re bubble suspensions have anisotropic microstructure in a much wider range of volume fractions than solid particle suspensions. It is important, then, to determine the microstructure in bubble suspensions and study how it evolves with Re and ϕ. In the next section, we will study the microstructure in bubble suspensions in more detail.

5.4 Microstructure

The microstructure in a suspension of bubbles can be characterized by the pair probability distribution function $\mathrm{P}(\mathbf{r})$

$$\mathrm{P}(\mathbf{r}) = \frac{L^3}{N^2}\langle \sum_i \sum_{j\neq i} \delta(\mathbf{r}-\mathbf{r}_{ij})\rangle \ , \tag{5.8}$$

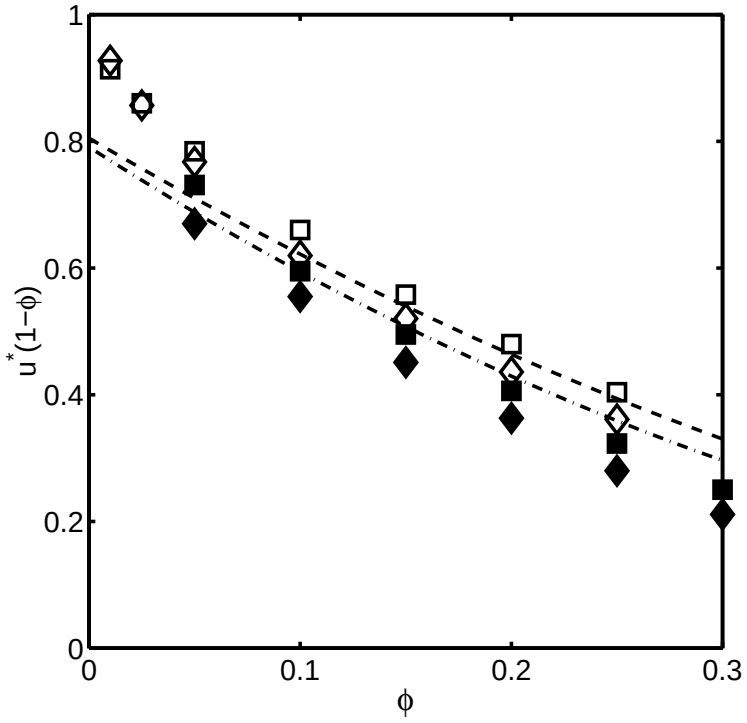

Figure 5.1: The dimensionless drift velocities $u^*(1-\phi)$ as functions of volume fraction ϕ. The open diamonds and squares represent the drift velocities in bubble suspensions with Re = 5.4 and 20. The filled diamonds and squares represent the drift velocities in solid particle suspensions with Re = 5 and 20. The dash-dot line corresponds to Eq. (5.6) and the dashed line corresponds to Eq. (5.7), both of which are based on the empirical formula in Ishii and Zuber [53] for suspensions of non-distorted bubbles. The data points for bubble suspensions were obtained with $L/d = 13.43$ ($\phi \leq 0.05$) or $L/d = 8.96$ ($\phi \geq 0.10$) and $\eta = 0.72$.

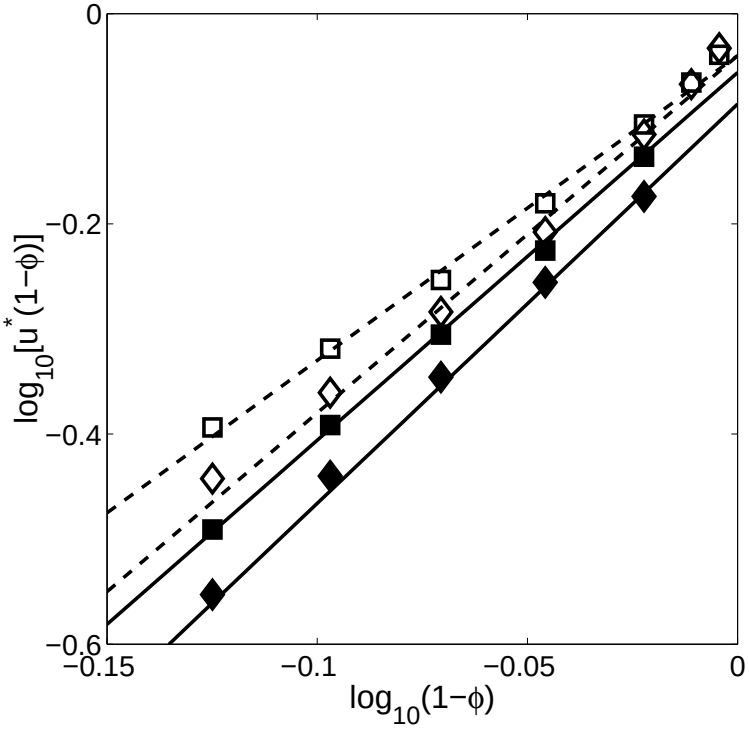

Figure 5.2: This figure shows the same data presented in Fig. (5.1) but using axes of $\log_{10}[u^*(1-\phi)]$ and $\log_{10}(1-\phi)$. The symbols have same meanings as in Fig. (5.1). The dashed lines corresponds to the best power-law fits to the drift velocities in bubble suspensions, the slope/intercepts of which are 3.9/0.91 and 3.5/0.90 for Re = 5.4 and 20, respectively. The solid lines corresponds to the best power-law fits in solid particle suspensions, with slope/intercepts being 4.0/0.86 and 3.6/0.88 for Re = 5 and 20.

where $\mathbf{r}_{ij}$ is the vector connecting bubble i and bubble j. The pair probability distribution $\mathrm{P}(\mathbf{r})$ has been measured experimentally by Cartellier and Rivière using phase detection optical probes [15] and it is found that when $\mathrm{Re} = O(10)$ there is a strong deficit in the rear of a test bubble, and moderate accumulation in the horizontal plane.

In numerical simulations, as the positions of the bubbles can be tracked accurately at all times, the determination of the microstructure is somewhat easier than in the experiments. However, to ensure that the microstructure obtained is accurate and meaningful, the suspension of interest must contain a sufficient number of bubbles, and the simulation should be long enough such that we can sample many independent configurations. In this section, we will present $\mathrm{P}(\mathbf{r})$ calculated from suspensions with 68 and 274 bubbles, which corresponds to $\phi = 0.05$ and $\phi = 0.20$ with $L/d = 8.96$. We have simulated larger suspensions with $L/d = 13.1$ to validate our results and find that the microstructure in larger systems is the same as obtained in smaller systems. The statistics of $\mathrm{P}(\mathbf{r})$ are based on 500-1000 configurations sampled from 4-5 independent runs. The time interval between samples in terms of the dimensionless time t^* is 1-2. These procedures ensure that $\mathrm{P}(\mathbf{r})$ obtained is accurate with small statistical variations.

Due to the axisymmetry in $\mathrm{P}(\mathbf{r})$ about the gravity direction, we can present $\mathrm{P}(\mathbf{r})$ as a function of two variables: the separation distance r and the angle θ with respect to the direction of gravity. Fig. (5.3) shows the pair probability distributions $\mathrm{P}(\mathbf{r})$ in bubble suspensions. When $\phi = 0.05$, the plots of $\mathrm{P}(r, \theta)$ show that there is a deficit region ($\mathrm{P} < 1$) surrounding the center bubble, and this deficit region extends longer in the vertical direction than in the horizontal direction with increasing Reynolds number. Outside the deficit region, a peak with

high probabilities (P > 1) can be found in the horizontal direction, the strength and position of which also depend on the Reynolds number: when Re = 5.4 the peak is rather weak and is located at $r/d \sim 2$; when Re = 20 the peak moves toward the center to a distance of $r/d \sim 1.5$ and becomes fairly strong. This anisotropic microstructure suggests that when $\phi = 0.05$ the bubbles tend to separate from each other and align themselves in the horizontal direction as they rise. Fig. (5.4) shows two snapshots of these dilute bubble suspensions and one can easily recognize the formation of clusters. The amount of clustering in our suspensions seems to be less than that observed in Bunner and Tryggvason's simulations with Re $\sim$ 30 [10], and is certainly less than the clustering observed in Sangani and Didwania's simulations, where bubbles are interacting with irrotational velocity potentials [115], and the clustering in Esmaeeli and Tryggvason's recent simulations where Re $\sim$ 100 [36]. This reduction proves that increasing viscosity does reduce the level of clustering in bubble suspensions. As the volume fraction increases to $\phi = 0.20$, the anisotropy becomes weaker and shorter in range. The deficit region now only appears at Re = 20 and it is in the shape of a spherical cap and is only present in the vertical direction at the contact distance of $r/d = 1$; in the horizontal direction, the high probability peak also moves to the contact distance.

Comparing the pair probability distributions in bubble suspensions to those in solid particle suspensions with comparable Reynolds numbers [Fig. (5.5)], one can see immediately the similarities and differences between the two types of suspensions. When volume fraction is low, the pair probabilities in bubble suspensions and those in solid particle suspensions have very similar shapes. The difference lies in that the pair probabilities in bubble suspensions have higher peaks in the horizontal direction at shorter distances, and the deficit region extends longer in

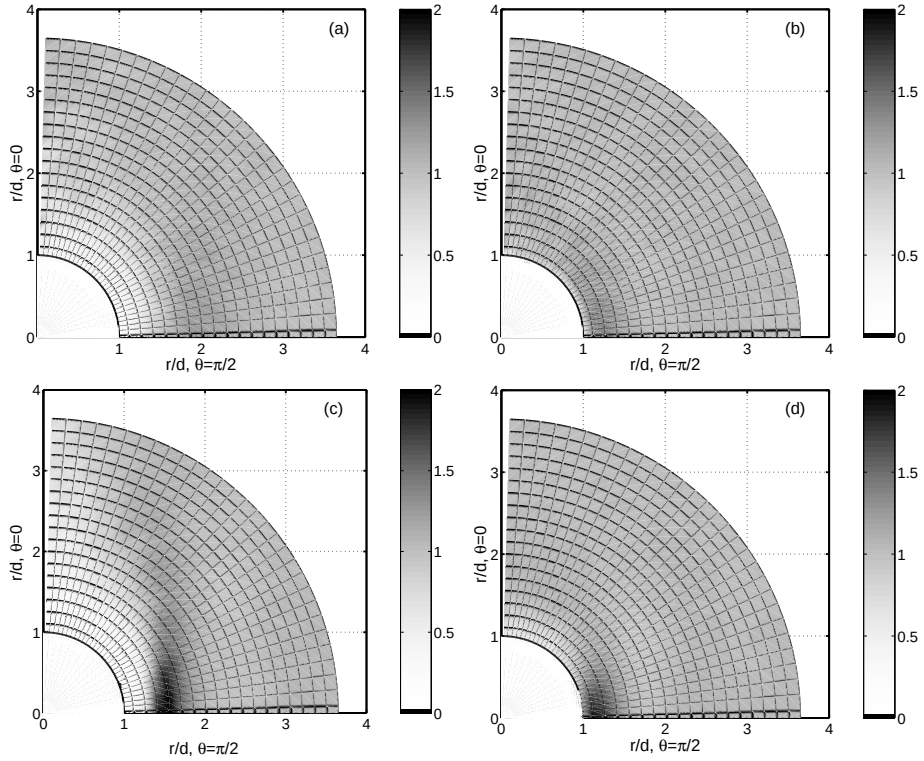

Figure 5.3: The pair probability density distribution $\mathrm{P}(\mathbf{r})$ in bubble suspensions. (a): Re = 5.4 and $\phi = 0.05$; (b): Re = 5.4 and $\phi = 0.20$; (c): Re = 20 and $\phi = 0.05$; (d): Re = 20 and $\phi = 0.20$. In these simulations $L/d = 8.96$.

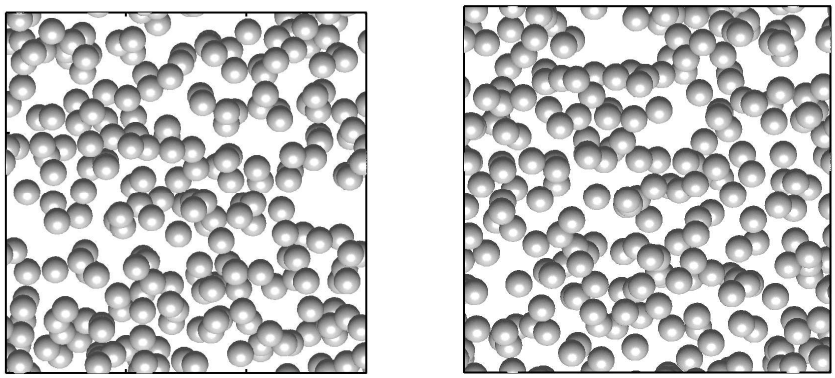

Figure 5.4: Snapshots of bubble suspensions with different Re to show the level of clustering in dilute suspensions ($\phi = 0.05$). Left: Re = 5; right: Re = 20. In both simulations $L/d = 13.4$ and the bubbles are moving upward.

the vertical direction. This difference is not that obvious when Re = 5 but becomes much more pronounced when Re = 20. When volume fraction is high, $\mathrm{P}(r, \theta)$ in solid particle suspensions become fairly random and isotropic, whereas $\mathrm{P}(r, \theta)$ in bubble suspensions still exhibit significant amount of anisotropy. At the end of last section, we have speculated based on the fact that $u^*(1-\phi)$ in bubble suspensions do not fit well to power laws that the microstructure in bubble suspensions may be anisotropic in a much wider range of volume fractions than that in solid particle suspensions. The pair probability distributions shown in Fig. (5.3) proves that this is indeed the case.

Based on the pair probability distribution $\mathrm{P}(r, \theta)$, one can calculate the radial distribution of bubbles in the suspension

$$\mathrm{g}(r) = \frac{1}{2} \int_0^{\pi} \mathrm{P}(r, \theta) \sin\theta \mathrm{d}\theta \tag{5.9}$$

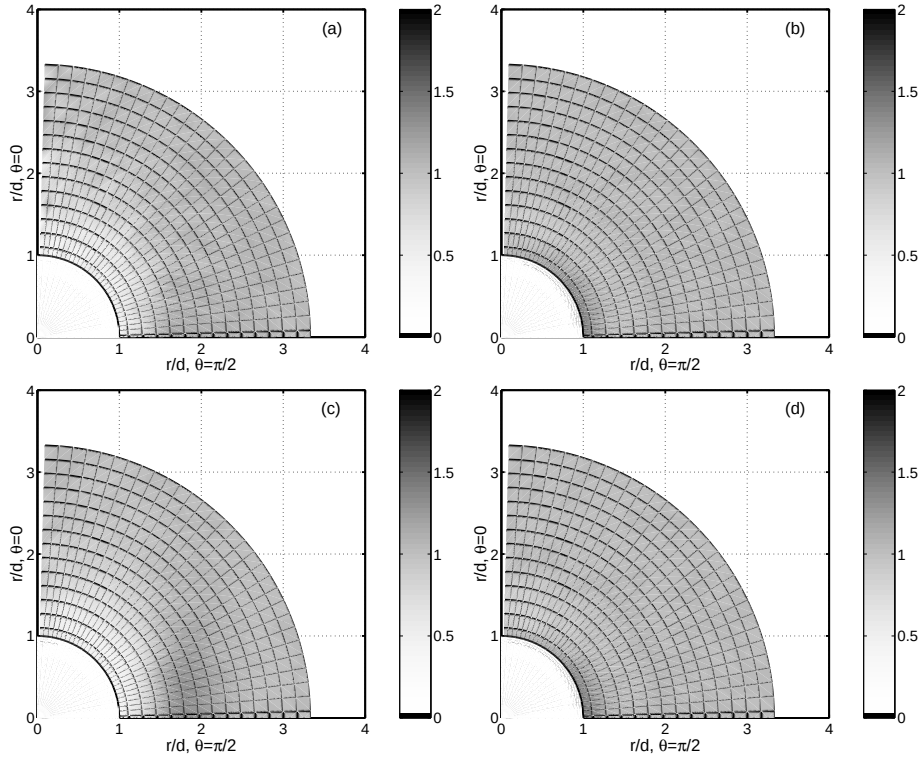

Figure 5.5: The pair probability density distribution P($\mathbf{r}$) in solid particle suspensions. (a): Re = 5 and $\phi = 0.05$; (b): Re = 5 and $\phi = 0.20$; (c): Re = 20 and $\phi = 0.05$; (d): Re = 20 and $\phi = 0.20$. In these simulations $L/d = 10.3$.

and the order parameter [74, 10]

$$\langle \mathrm{P}_2 \rangle(r) = \frac{\int_0^\pi \mathrm{P}(r,\theta)\mathrm{P}_2(\cos\theta)\sin\theta \mathrm{d}\theta}{\int_0^\pi \mathrm{P}(r,\theta)\sin\theta \mathrm{d}\theta} \ , \tag{5.10}$$

where $\mathrm{P}_2(\cos\theta) = (3\cos^2\theta - 1)/2$ is the second order Legendre polynomial. The radial distribution $\mathrm{g}(r)$ measures the availability of pairs with separation r in a suspension and it has an equilibrium value of one; the order parameter $\langle \mathrm{P}_2 \rangle(r)$, on the other hand, measures the probability of pair orientations. In a perfectly random and isotropic suspension, bubble pairs have no preferred direction and $\langle \mathrm{P}_2 \rangle(r)$ has an equilibrium value of zero. If all pairs are aligned with the rising direction of $\theta = 0$, $\langle \mathrm{P}_2 \rangle(r) = 1$; if all pairs are aligned with the horizontal direction of $\theta = \pi/2$, $\langle \mathrm{P}_2 \rangle(r) = -1/2$. Thus, the sign of $\langle \mathrm{P}_2 \rangle(r)$ becomes an indication of bubble pair orientations: a positive sign indicates that bubbles are more likely to align in the vertical direction; a negative sign, on the other hand, indicates that bubbles prefer to align in the horizontal direction.

Fig. (5.6) shows the radial distribution function $\mathrm{g}(r)$ in bubble and solid particle suspensions. When $\phi = 0.05$, $\mathrm{g}(r)$ in bubble suspensions and $\mathrm{g}(r)$ in solid particle suspensions have similar shapes: there is a deficit of pairs at close distance and an excess further away that corresponds to the peak in the pair probability distribution in the horizontal direction. $\mathrm{g}(r)$ in bubble suspensions is different from $\mathrm{g}(r)$ in solid particle suspensions in that it deviates much more from the equilibrium value of one, which is consistent with our earlier observations that the level of anisotropy in bubble suspensions is higher than that in solid particle suspensions. When $\phi = 0.20$, the radial distributions in solid particle suspensions are fairly close to those in a hard sphere suspension — peaks due to excluded volume interaction can be observed at the distance of $r/d = 1$ and $r/d = 2$. The radial distributions

in bubble suspensions, however, are very different from that in a hard sphere suspension. In the region of $1.2 < r/d < 1.7$, g(r) in bubble suspensions shows a considerable excess, which suggests at high volume fractions bubbles are grouped more tightly than solid particles.

Fig. (5.7) shows the order parameter $\langle \mathrm{P}_2 \rangle(r)$ in bubble and solid particle suspensions. When volume fraction is low, a general observation is that bubble or solid particle pairs that are very close ($r/d < 1.2$) are more likely to align in the vertical direction, and pairs that are further apart tend to align in the horizontal direction. When volume fraction is high, $\langle \mathrm{P}_2 \rangle(r)$ in solid particle suspensions is never positive, whereas $\langle \mathrm{P}_2 \rangle(r)$ in bubble suspensions can be positive at some intermediate distances ($1.7 < r/d < 2$). The overall difference between $\langle \mathrm{P}_2 \rangle(r)$ in bubble suspensions and that in solid particle suspensions is fairly small when $\mathrm{Re} = 5$, but becomes more dramatic when Re reaches 20, where it becomes very clear that the likelihood for bubble pairs to align in the horizontal direction is much more than that for solid particle pairs.

It is worth mentioning that both g(r) and $\langle \mathrm{P}_2 \rangle$ reach their equilibrium values at a distance of $r/d \sim 3$, which is less than the size of our computational domain. This proves that our suspensions are still homogeneous on large length scales, and the domain size used in our simulations is sufficiently to cover the length scale of the microstructure.

In order to understand why such microstructure would develop in bubble suspensions, it is useful to review the mechanism that produces the anisotropic microstructure in dilute solid particle suspensions, the pairwise inertial wake interaction. When a test particle is settling through the fluid with finite Re, the fore-aft symmetry of the flow field is broken and a wake, or velocity defect, develops behind

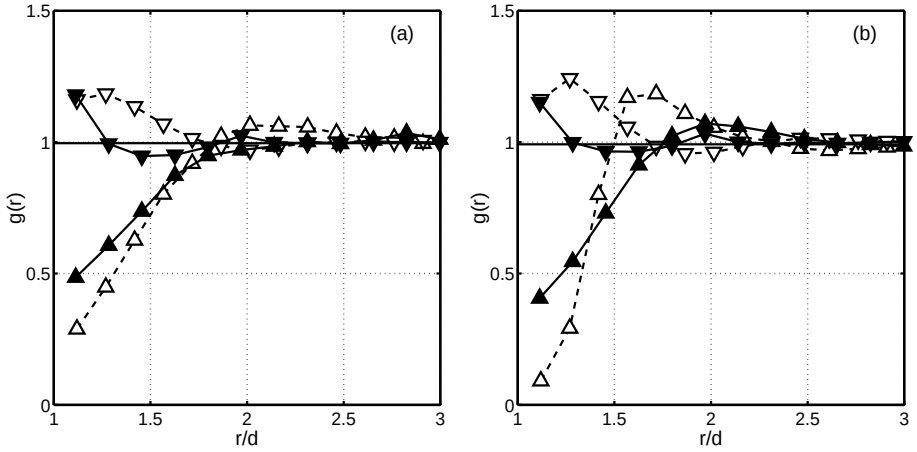

Figure 5.6: The radial distribution function g(r) in bubble and solid particle suspensions. (a): Re = 5; (b): Re = 20. The upward triangles represent $\phi = 0.05$; the downward triangles represent $\phi = 0.20$. Dashed lines with open symbols are for bubble suspensions; solid lines with filled symbols are for solid particle suspensions.

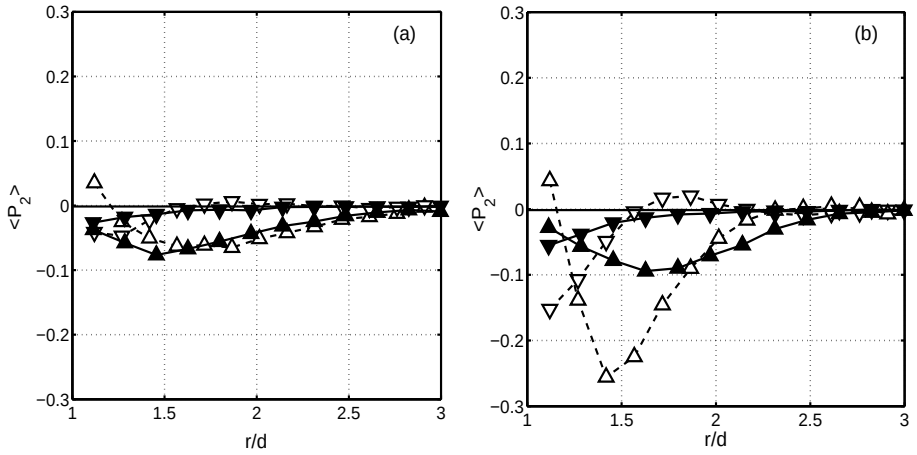

Figure 5.7: The order parameter $\langle \mathrm{P}_2 \rangle(r)$ in bubble and solid particle suspensions. (a): Re = 5; (b): Re = 20. The lines and symbols have the same meanings as in Fig. (5.6).

the test particle. During sedimentation, if another particle enters the test particle's wake, it experiences less drag and thus will approach the test particle from behind. However, the center of a wake is not a stable position, for the velocity gradient in the wake will produce a lift force which moves the trailing particle to the side [60]. Thus, when the trailing particle catches the test particle from behind, the pair will change its orientation, rotate into the horizontal direction, and then separate. This pairwise interaction between a pair of solid particles is often referred to as the drafting-kissing-tumbling mechanism [37]. In dilute suspensions, this pairwise interaction dominates and it removes most particles from each other's wake. As a result, a microstructure with a deficit in the vertical direction and a peak in the horizontal direction is formed. Since the strength of this pairwise interaction increases with increasing Re, the anisotropy in the microstructure is also stronger at higher Reynolds numbers. In concentrated suspensions, the pairwise interaction is disrupted by the more random and chaotic many-body interactions. Therefore, the anisotropy in solid particle suspensions disappears very quickly with increasing volume fraction.

The pairwise interactions between bubbles are known to be more complex than the interaction between a pair of solid particles. When Re is low but finite, it is known that a pair of bubbles will draft, kiss, and tumble just like solid particles. When Re is high, the potential flow theory gives a complete opposite prediction that bubbles rising in line would repel each other and bubbles rising side-by-side would attract each other [5, 65, 66, 68]. Harper [44] pointed out that bubbles moving with high Reynolds numbers still have thin wakes. As a result, bubbles rising in line will first approach each other under the influence of the wake, then slow down and stop at an equilibrium position where the attraction from the wake

balances the repulsion from the interacting velocity potentials. From numerical simulations, Yuan and Prosperetti verified that such equilibrium positions do exist when Re is between 50 and 200 [136]. However, the equilibrium position in the vertical direction is not a stable one, because the lift force will make trailing bubble move to the side [60]. In the studies by Cartellier and Rivière [15], and Bunner and Tryggvason [10], it has been observed that bubbles with Re of $O(10)$ do not collide but rather rotate smoothly past each other, consistent with the discussions above. For bubbles that are aligned side-by-side, based on the numerical study by Legendre *et al.*[80], fixed bubbles with Re < 30 always repel each other, and fixed bubbles with Re ≥ 30 will attract each other if their vorticity fields does not interact with each other, and repel each other otherwise. Clearly, the extent of the vorticity field decreases with increasing Reynolds number so high Re bubbles are more likely to attract each other from the side. Bunner and Tryggvason [10] have measured the relative velocities between pairs of bubbles in a freely evolving suspension and confirmed that bubbles with Re ~ 20 (based on the relative velocity) always repel in the horizontal direction.

In our simulations, the Reynolds numbers based on terminal velocities are 5.4 and 20. Based on the above discussions, we expect that our bubbles will attract each other if they are aligned in the vertical direction and repel each other if aligned in the horizontal direction, similar to the interaction between solid particles. However, there are still many details about bubble-bubble interactions waiting to be worked out, such as how a bubble pair turns from the vertical direction to the horizontal direction, and how this process differs from the drafting-kissing-tumbling between solid particles. We conducted two sets of simulations to probe such details. In the first set of simulations, we placed two bubbles/solid particles one on top of

another in a large rectangular computation domain and let them rise/settle. The trajectories of the trailing bubble/particle relative to the leading one are shown in Fig. (5.8). In the second set of simulations, we placed the bubbles/solid particles side-by-side and the trajectories are shown in Fig. (5.9). From Fig. (5.8), it can be observed that bubbles with Re = 5.4 are interacting with each other in a way very similar to the drafting-kissing-tumbling interaction between solid particles. Bubbles with Re = 20, however, interact with each other differently in that they do not collide and rotate but rather pass each other smoothly without touching, as observed in Cartellier and Rivière [15] and Bunner and Tryggvason [10]. This difference clearly shows that the interaction between bubbles with Re = 20 is not completely controlled by the wake interaction but also controlled, at least partially, by the irrotational velocity potentials. From Fig. (5.9), it can be observed that during the same rise/settling time ($t^* = 60$), bubbles are not pushed away in the horizontal direction as far as the solid particles of the same Re. Moreover, the repulsion is weaker at higher Reynolds numbers.

Although the vertical pair interaction in Re = 5.4 bubble suspensions is different from that in Re = 20 bubble suspensions — one is completely dominated by the inertial wake and another is partially controlled by wake and partially by the velocity potentials, the net effects are the same in that both interactions will turn a vertically aligned pair into a horizontally aligned one, and, given enough time, they will move most bubbles into horizontally aligned clusters. Once the bubbles move into clusters, they will stay there for a relatively long time — longer than solid particles because, as indicated by Fig. (5.9), the bubbles do not repel as strongly as solid particles. This difference, we think, can explain why bubble suspensions have higher and closer peaks in $P(r, \theta)$ than solid particle suspensions.

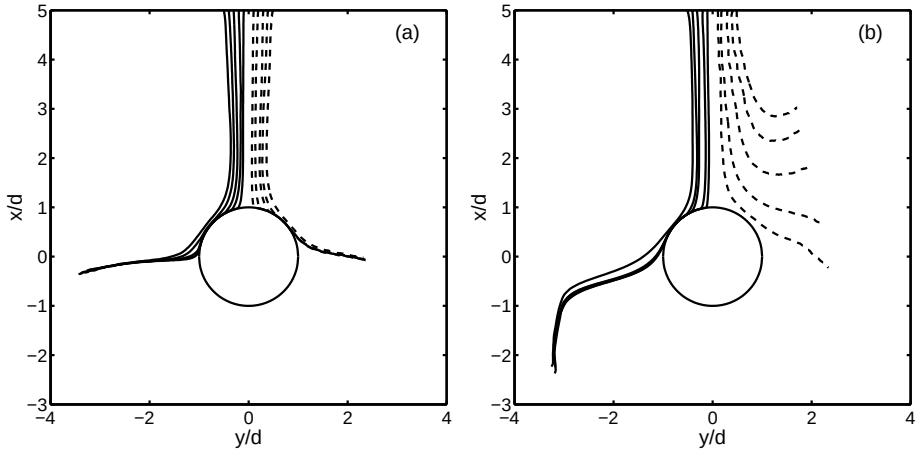

Figure 5.8: The trajectories of a trailing bubble or solid particle approaching a leading one and migrating to the side. (a): Re = 5; (b): Re = 20. Length units are normalized by d. Simulations were conducted in domains with size $17.9\times8.96\times8.96$ in terms of d, with gravity aligned to the longest dimension. The duration of the simulations is $t^* = 60$. The solid lines are for solid particles and dashed lines are for bubbles.

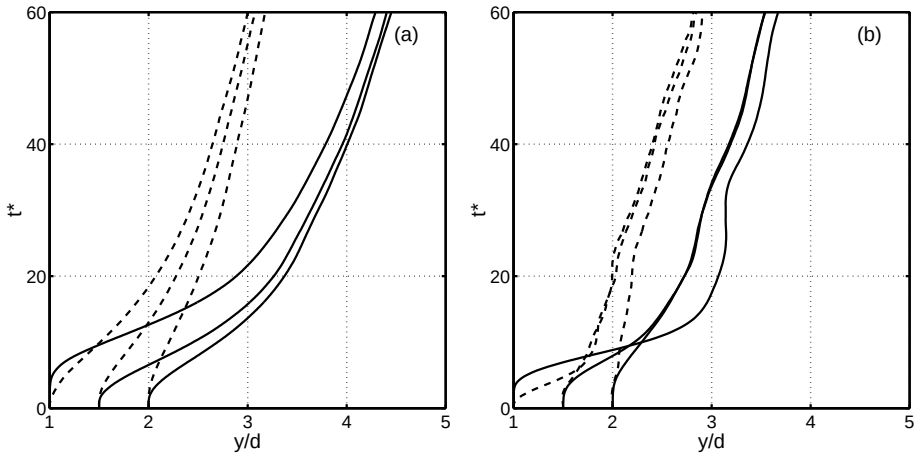

Figure 5.9: The interaction between a pairs of bubbles and the interaction between a pair of solid particles rising side-by-side. (a): Re = 5; (b): Re = 20. The horizontal axis is the horizontal separation normalized by d; the vertical axis is the dimensionless time t^*. Simulations were conducted in domains with size $17.9 \times 11.9 \times 11.9$ in terms of d, with gravity aligned to the longest dimension. The solid lines are for solid particles and dashed lines are for bubbles.

5.5 Effect of vertical walls in a bubble channel

In this section, we are interested in a bubbly flow bounded between a pair of solid walls, and, in particular, the volume fraction and flow profiles. This study is motivated by the fact that walls can modify the spatial distribution of bubbles through a repulsive interaction. The non-uniform distribution of bubbles will affect the flow profile between walls, and the disturbed non-uniform flow profile, in turn, can affect the distribution of bubbles. Due to this close coupling, the volume fraction and flow profiles can only be solved accurately by simulations. As the volume fraction and flow profiles in a wall-bounded channel are strongly influenced by whether there is a net flow of the liquid phase [6], in this study we adjusted the reverse pressure gradient such that the net flow of the liquid phase is exactly zero.

The simulations were conducted in rectangular domains ($L_x \times L_y \times L_z$) with the gravity aligned to the $-x$ direction. Solid walls with no-slip conditions were applied at $y = 0$ and $y = L_y$; on the x and z boundaries periodic conditions were assumed. We used two different domain sizes: $8.96 \times 6.72 \times 6.72$ and $8.96 \times 11.2 \times 6.72$ (normalized by bubble diameter d) to see whether wall-to-wall distance has an effect on the volume fraction and flow profiles. The Reynolds numbers, again, are 5.4 and 20; the volume fractions of the suspensions are 0.05 and 0.10.

In Fig. (5.10) and Fig. (5.11), we show the steady-state volume fraction and velocity profiles in the channels. Due to the repulsive bubble-wall interaction, there are deficits of bubbles near the walls. These deficits reduce the buoyancy force acting on the fluid and generate backflows, which can be recognized from the fluid velocity profiles. In the region less than $0.5d$ away from the walls, the velocity gradients in the backflows produce lift forces on the bubbles, which are

in the same direction as the wall repulsive forces; in the region $0.5 < y/d < 1.5$ (approximately), the fluid velocity profiles turn back and the lift forces change directions. As a result, the migration of bubbles from the wall to the bulk is stopped in this region, and bubbles accumulate and form two very distinctive peaks in the volume fraction profiles.

What are more surprising are the oscillations of the volume fraction profiles in the bulk region, which are not found in simulations in periodic domains. These oscillations suggest that bubbles form "layers" when they rise between solid walls. As Fig. (5.10) and Fig. (5.11) show, the wavelength of these oscillations seems to decrease with increasing ϕ and Re; the strength of the oscillation also decreases with increasing ϕ. Interestingly, the distance between layers, or the wave length of the oscillations, is not affected by the wall-to-wall distance: when wall-to-wall distance is increased, the suspension simply adjusts itself and produces more layers such that the distance between layers is approximately a constant.

As the distance between layers is independent of the wall-to-wall distance L_y/d, the only macroscopic length scale in the system, it must be an intrinsic property of the suspension. By measuring this distance from the volume fraction profiles, we find that it agrees very well with the distance r/d where the peak of the pair probability $\mathrm{P}(r, \theta)$ is located [see Table 5.2]. Thus, we believe that these layers must come from the non-random microstructure in bubble suspensions. Although the distance between layers is not affected by the wall-to-wall distance, the presence of walls is still critical in that it introduces the first pair of peaks in the volume fraction profile. These primary peaks near the walls then modify the distribution of bubbles through the anisotropic hydrodynamic interactions and arrange the bubbles into layers, the distance between which is determined by the most probable distance

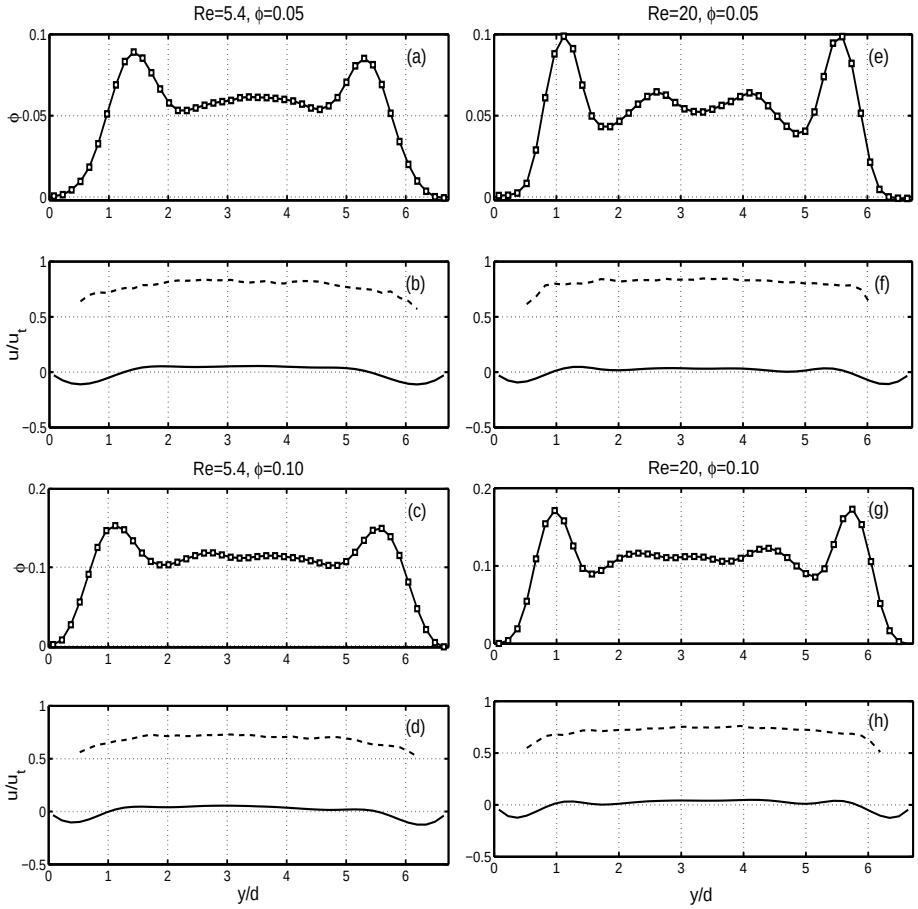

Figure 5.10: Volume fraction and fluid and particle velocity profiles in a vertical channel with $L_y/d = 6.72$. (a), (c), (e), and (g) are the volume fraction profiles and (b), (d), (f), and (h) are the velocity profiles, where solid lines are for fluid velocities and dashed lines are for the bubble velocities. The figures on the left have Re = 5.4; the figures on the right have Re = 20.

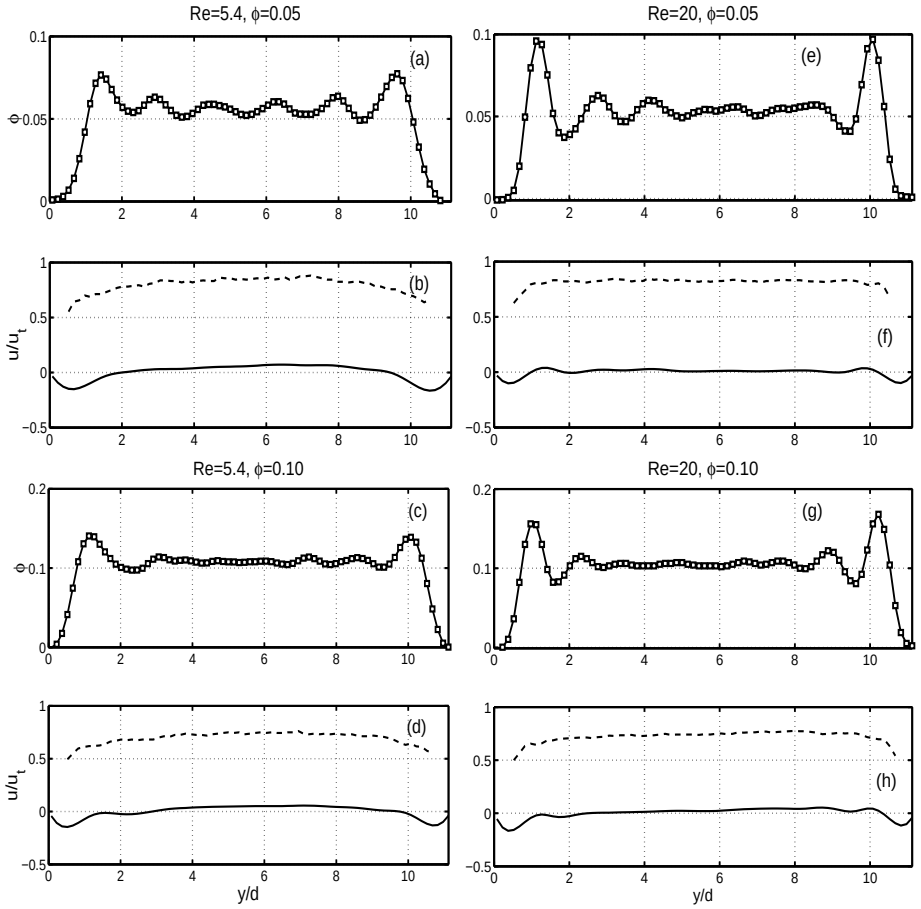

Figure 5.11: Volume fraction and fluid and particle velocity profiles in a vertical channel with $L_y/d = 11.2$. (a), (c), (e), and (g) are the volume fraction profiles and (b), (d), (f), and (h) are the velocity profiles, where solid lines are for fluid velocities and dashed lines are for the bubble velocities. The figures on the left have Re = 5.4; the figures on the right have Re = 20.

Table 5.2: The distances between layers in vertical channels compared to the most probable distances between bubble pairs. All distances are normalized using bubble diameter d. In each entry, the number before the slash is the distance between the two primary peaks near the wall and the number after is the average distance between recognizable layers. r_p is the location of the peak in $\mathrm{P}(r, \theta)$.

Ar	ϕ	$L_y/d = 6.72$	$L_y/d = 11.2$	r_p/d
87.8	0.05	3.9 / 1.9	8.2 / 1.6	1.9
	0.10	4.5 / 1.5	9.0 / 1.6	1.6
451.1	0.05	4.5 / 1.5	9.0 / 1.5	1.5
	0.10	4.8 / 1.3	9.2 / 1.3	1.4

between bubble pairs — the distance of maximum $\mathrm{P}(r, \theta)$.

In a wall-bounded system of hard spheres, it is known that at high volume fractions, the presence of walls will force the spheres to form layers, and the resulted volume fraction profile resembles those shown in Fig. (5.10) and Fig. (5.11). This resemblance, however, is only superficial. In hard sphere systems, the layers come from excluded volume interactions and they are stronger at higher volume fractions. In wall-bounded bubble suspensions, the layers come from the anisotropic microstructure, the strength of which decreases with increasing volume fraction. Therefore, the layers in a wall-bounded bubble suspension respond to a volume fraction change in a very different way: at a low volume fraction of $\phi = 0.05$, the layers are strong and can be easily recognized; with the volume fraction increased to $\phi = 0.10$, the layers become weaker, especially in the bulk region away from the walls.

5.6 Summary

In this chapter, using a lattice-Boltzmann method developed for bubbles with slip boundary conditions, we simulated the free rise of bubbles and studied the rise velocity, microstructure, and effect of walls on the suspension. Our bubbles are monodisperse, spherical and are not allowed to coalesce, which allows us to focus on how the slip boundary condition affects the hydrodynamic interaction and suspension properties. In our simulations, the bubbles have moderate Reynolds numbers in the range 5-20, thus inertial effects are important. The range of volume fraction in this study is $0.01 < \phi < 0.25$.

By comparing the drift velocities of bubbles in our simulations to the drift velocities of sedimenting solid particles with comparable Reynolds numbers, we find out that the drag acting on bubbles is less than that acting on solid particles, which is not surprising because slip boundaries always have less flow resistance compared to no-slip boundaries. It is widely known that the drift velocities of settling solid particles can be well described by simple power-law functions of $1 - \phi$, except for some deviation at low volume fractions, which can be attributed to a non-random microstructure where particle pairs are more likely to separate and align in the horizontal direction. In the region where the drift velocities fit well to power laws a random and isotropic microstructure is always observed (see Chapter 2). We attempted to fit the drift velocities of bubbles to the same form of power laws, but found instead that power laws do not provide an accurate fit. Inspired by the relation between the power law behavior of the drift velocity and a random and isotropic microstructure, we studied the microstructure in bubble suspensions and find that bubbles have stronger tendency to align in the horizontal

direction than solid particles. Moreover, the resulted anisotropic microstructure in bubble suspensions, which has a strong pair correlation in the horizontal direction, occurs for a wider range of volume fractions than that in solid particle suspensions. In our simulations, we find that bubble suspensions have strong anisotropic pair probabilities at $\phi = 0.20$, whereas the anisotropy in solid particle suspensions diminishes around 0.05-0.10. This difference in the microstructure, we believe, causes the drift velocities of bubbles to deviate from simple power laws.

The anisotropic microstructure in bubble suspensions is generated by the strong anisotropic inertial interactions between pairs of bubbles. In our simulations, we find that bubbles with $\mathrm{Re} = 5.4$ interact with each other primarily through wakes. The interaction between bubbles with $\mathrm{Re} = 20$, however, is partially controlled by the potential flow interaction. As a result, when $\mathrm{Re} = 5.4$, bubble pairs are like solid particle pairs in that both types draft, kiss, and tumble [37]; when $\mathrm{Re} = 20$ the bubbles still approach each other in the vertical direction, but do not collide but rather pass each other smoothly, then push each other away. Over time, such interactions eliminate most of the vertical pairs and drive the bubbles into horizontally aligned clusters. Because the repulsion between horizontally aligned bubbles is less than that between solid particles, larger clusters can be maintained in bubble suspensions, making the pair probability distributions $\mathrm{P}(r, \theta)$ more anisotropic in bubble suspensions than in solid particle suspensions.

Finally, we studied the effect of walls on bubble suspensions. This study is motivated by the fact that effect of a wall on a nearby rising bubble has been studied in great details [124, 123, 86], the effect of a wall on a suspension of freely rising bubbles, on the other hand, has not been studied accurately. Our simulations in wall-bounded channels show that wall repulsion, buoyancy and lift

force work together and produce deficit layers near the walls and volume fraction peaks right next to the deficit layers. These peaks then induce more vertical layers that extend all the way into the bulk suspension, far away from the walls. It is discovered that the distance between layers agrees with the distance of maximum pair probability $\mathrm{P}(r, \theta)$. Thus, we believe that these layers are associated with the non-random microstructure in bubble suspensions. Although the distance between layers does not depend on walls, it does requires the presence of walls to produce initial inhomogeneities such that the "intrinsic modes" hidden in the non-random pair probabilities can be excited.

Chapter 6

Numerical and Experimental Studies on the Lift Force in a Sheared Bubble Suspension in a Slightly Inclined Channel

6.1 Introduction

It is well known that a bubble moving in a linear shear flow will experience a transverse force known as the lift force. The lift force acting on an isolated spherical bubble as a function of its Reynolds number and local shear rate has been studied in great detail [83, 2, 78, 79] and the knowledge on the lift force coefficient for an isolated spherical bubble is fairly complete. In many practical flows, however, the volume fraction of the suspension is not dilute enough that we can direct apply the lift force coefficient of an isolated bubble. The effect of finite volume fraction ϕ on the lift force, therefore, is worth studying. In order to measure the lift force in a suspension, one must shear a suspension and analyze the force balance on the bubbles. In this numerical study, we were able to generate a nearly viscometric linear shear flow in a suspension of monodisperse, non-coalescing, spherical bubbles in a slightly inclined channel. In the direction perpendicular to the walls, the force balance on the bubbles only involves a effective lift force from the linear shear, and

a gravity component from the finite inclination angle θ. From this simple force balance, we determined the effective lift force coefficients in sheared suspensions.

In this work, the problem of the shear-induced lift force is considered in a reference frame $(\mathbf{e}_x, \mathbf{e}_y, \mathbf{e}_z)$ where $\mathbf{e}_x$ is the direction of the relative motion u_r, $\mathbf{e}_y$ is the direction of the velocity gradient, i.e., $\mathrm{d}u/\mathrm{d}y = \alpha$, and $\mathbf{e}_z$ is the direction of the vorticity $\boldsymbol{\omega} = \nabla \times \mathbf{u} = -\alpha \mathbf{e}_z$. In this reference frame, the lift force $\mathbf{F}_L$ is in the direction of $\mathbf{e}_y$ and its magnitude is proportional to the relative velocity u_r and velocity gradient α by

$$F_L = \frac{\rho \pi d^3}{6} C_L u_r \alpha \ , \tag{6.1}$$

where ρ is the fluid density, d is the bubble diameter, and C_L is the lift force coefficient. To differentiate the lift force coefficient in a suspension with that of an isolated bubble, we will use C_L^* from now on to represent the lift force coefficient in a suspension, and C_L to represent the lift force coefficient of an isolated bubble.

The shear-induced lift force acting on a spherical bubble is known to be an inertial effect, because the reversibility in Stokes flows does not allow such a force to occur. Due to the three-dimensional nature of the problem, analytical determination of C_L is difficult and solutions are limited to flows with either very high Reynolds numbers, where a weak shear is imposed on a potential flow field, or flows with very low but still finite Reynolds numbers, where the effects of inertia and shear can be considered as perturbations. Here the Reynolds number is defined as $\mathrm{Re} = \rho u_r d/\eta$ with η the viscosity of the fluid. The velocity gradient α can be non-dimensionalized into $\mathrm{Sr} = \alpha d/u_r$. In the high Re limit, based on the early work of Lighthill [83], Auton [2] obtained the well-known limit of $C_L = 1/2$. In the low but finite Re limit, based on Saffman [112] and McLaughlin [88]'s analysis for rigid spheres, Legendre and Magnaudet [78] derived an expression of C_L for an

isolated bubble

$$C_L = \frac{6}{\pi^2} \left(\mathrm{ReSr}\right)^{-1/2} J(\epsilon) \ , \tag{6.2}$$

where $\epsilon = (\mathrm{Sr}/\mathrm{Re})^{1/2}$ and $J(\epsilon)$ is the value of a three-dimensional integral which has been determined numerically in [88]. $J(\epsilon)$ is a monotonically increasing function of ϵ. In the limit of $\epsilon \to \infty$, $J(\epsilon) \to 2.255$. In the intermediate Re regime, an analytical solution of C_L is not available. Legendre and Magnaudet [79] conducted numerical simulations in the range $0.1 < \mathrm{Re} < 500$ and $0.02 < \mathrm{Sr} < 1$, measured the lift force acting on a bubble fixed in a steady linear flow, and proposed the following expression:

$$C_L = \left(\left[\frac{6}{\pi^2} \left(\mathrm{ReSr}\right)^{-1/2} J'(\epsilon) \right]^2 + \left[\left(\frac{1}{2} \right) \left(\frac{1 + 16\mathrm{Re}^{-1}}{1 + 29\mathrm{Re}^{-1}} \right) \right]^2 \right)^{1/2} \ , \tag{6.3}$$

where

$$J'(\epsilon) = \frac{2.255}{\left(1 + 0.2\mathrm{Re}/\mathrm{Sr}\right)^{3/2}} \tag{6.4}$$

is an empirical function based on the computational results and the requirement that when Re is small, $J'(\epsilon)$ should approach $J(\epsilon)$.

In a sheared suspension, the flow field that a bubble experiences is modified by the inclusion of other bubbles. As a result, the effective lift force coefficient C_L^* is going to be different from C_L. Sankaranarayanan and Sundaresan [119] studied the rise of a nearly spherical bubble in a cubic computational domain with imposed shear and found that the lift force increases with decreasing domain size (increasing ϕ). Their computational domains are periodic in the flow and vorticity directions (x and z) so this increase in the lift force is very likely the result of the hydrodynamic interaction between the bubble and its periodic images. According to their simulations where the Reynolds number of the bubble is around 200, at $\phi = 0.08$ there is a 10% increase in C_L compared to the theoretical value of 1/2.

In this work, we studied the effect of finite volume fraction on the lift force in more details. Our simulations are set up differently from [119] in that we are simulating the shearing motion of a disordered suspension, which is more realistic than a periodic suspension with one bubble in a periodic box. Moreover, the shearing motion is not imposed explicitly, but rather established gradually instead in an inclined channel as the flow approaches its steady state. The characteristics of the steady state volume fraction and velocity profiles allow us to isolate the lift force and buoyancy from other forces, especially the influence from the bubble phase pressure gradient. Thus, the effective lift force coefficient in a sheared suspension can be determined unambiguously. In our simulations, the Reynolds number is from 5 to 20; the volume fraction of the suspension is from 5% to 10%; the value of Sr, which can be adjusted by changing the inclination angle, varies between 0.1 and 0.6. In the end, we conducted experiments and verified our simulation results.

This chapter is organized as follow. In Section 6.2, we describe the numerical method, explain the inclined channel configuration, and show that it can produce a nearly viscometric shear flow in the middle of the channel. In Section 6.3, we present the effective lift force coefficients from simulations, establish a simple analytical model for the flow profiles, and discuss the parametric range where we can obtain such flows. In Section 6.4, we present an experimental study of bubbly flows in inclined channels and compare the experimental results to the simulations. Finally, in Section 6.5, we summarize and conclude the chapter.

6.2 Numerical method and the inclined channel configuration

Our numerical method is based on a lattice-Boltzmann scheme developed by Ladd [71, 72, 76] for suspensions of spherical solid particles. A boundary rule developed by Yin *et al.*[135] that can recover the slip boundary condition on gas-liquid interfaces is added such that suspensions of spherical, non-coalescing bubbles can be simulated. In this method, the bubbles are approximated as spheres with slip boundaries, the density of which is 0.001 times the density of the fluid. The flow in the continuous phase is solved by the lattice-Boltzmann method. The motions of bubbles are then determined using the mass of the bubble and the difference between the integral of the fluid stresses on the bubble surface and the buoyancy force. When two bubbles collide, elastic collisions are assumed. More detailed descriptions and validation tests are available in Chapter Eq. (4). In our lattice-Boltzmann model, the density of the fluid is $\rho = 36$, the viscosity of the fluid is $\eta = 0.36$. We used a bubble size of $d = 6.7$ in our simulations, which, according to the validation tests in Chapter 4, is sufficiently accurate for the range of Re that we are interested compared to bubbles with larger sizes.

We simulated the rise of bubbles in an inclined channel shown schematically in Fig. (6.1). This configuration is inspired by the experimental setup used by Zenit *et al.*[140] to generate a weak shear flow of a suspension of monodisperse and nearly spherical nitrogen bubbles in an aqueous solution of 0.05 $mol \cdot l^{-1}$ magnesium sulfate. The role of the magnesium sulfate is to suppress bubble coalescence and maintain the monodispersity of the suspension and the slip boundary condition on bubble surface [140, 82, 138]. In their experiments, the bubbles are about

1.5 mm in size thus have high Reynolds numbers (Re $\sim$ 200) but relatively low deformations (aspect ratio $\sim$ 1.2). They measured the bubble volume fraction profiles and bubble and liquid velocity profiles in sheared suspensions at different volume fractions ($0.02 < \phi < 0.10$) and different inclination angles ($0^\circ < \theta < 10^\circ$).

In our simulations, we attempt to use the same configuration to set a suspension of monodisperse, spherical bubbles into a shearing motion. Our computational domains are rectangular, bounded in the x and z directions by periodic conditions, and bounded in the y direction by a pair of solid walls. The size of the computational domain, normalized by the bubble size, is $14 \times 14 \times 7$ in x, y, and z directions, respectively. We will see in Section 6.4 that the ratio of L_y/d in our simulations is in good agreement with the gap to bubble size ratio in the experiments. We conducted a few verification runs, some with higher lattice resolutions ($d = 12.1$) and others with higher L_x/d and L_z/d ratios, and proved that our results are not sensitive to the choice of lattice resolution and the periodic lengths in the x and z directions.

Initially, the bubbles are placed randomly in the computational domain and have zero velocity. Once the simulation begins, they start to accelerate in the x direction and migrate in the y direction under the influence of gravity. For simplicity, we will refer to the wall that the bubbles migrate to as the "upper" wall and the wall in the opposite direction as the "lower" wall although in fact they are nearly vertical. Because of the bubble migration, a layer with high bubble concentration is formed near the upper wall, and a fluid layer that is almost depleted with bubbles is formed near the lower wall. These layers will be referred to the bubble-rich layer and the depletion layer in the following sections, respectively.

Because the bubble-rich layer is more buoyant than the depletion layer on the

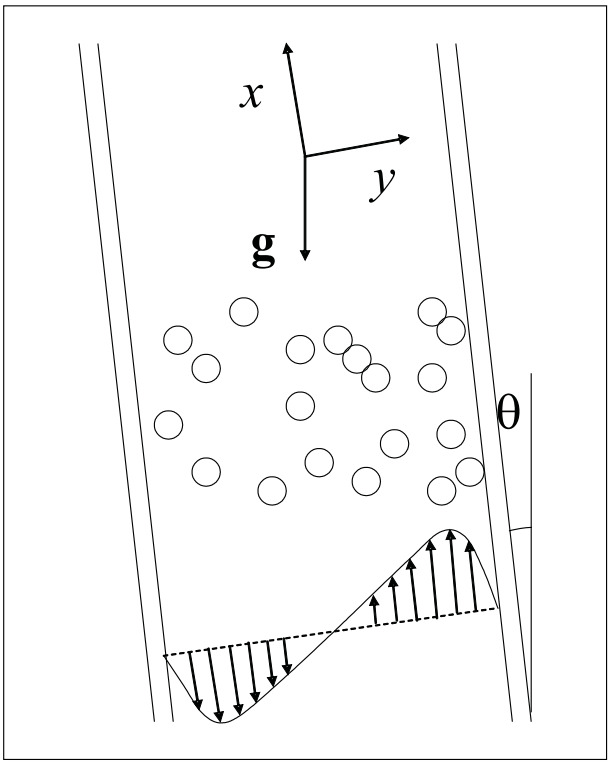

Figure 6.1: A schematic of the inclined channel configuration.

other side of the channel, as the bubbles migrate to the upper wall, the suspension in the middle starts to experience this difference in the buoyancy and a shear flow starts to develop. This shear flow plays an important role in the dynamics of the system, because it produces a lift force that is opposite to g_y and thus will slow down further migration of bubbles toward the upper wall. Under the right combination of Re, θ, and ϕ, [see Fig. (6.4) and the discussion in Section 6.3], the suspension can evolve into a stable equilibrium, where the shear flow generated by the buoyancy difference between the wall layers is just sufficient to stop the bubble migration (in an averaged sense) before most bubbles could reach the upper wall. After this balance has been established, the bubbles in the middle form a homogeneous suspension and its properties can therefore be studied.

Based on the above discussions, we monitor the average y-position of all bubbles $\langle y/d \rangle$ as a function of time. When $\langle y/d \rangle$ stops moving toward the upper wall, a steady state is reached. The dynamics approaching the steady state is controlled by the buoyancy and the viscous diffusion of momentum. In general, the diffusion of momentum must be sufficiently fast such that the shear flow can develop before the buoyancy has moved all bubbles to the upper wall. In our simulations, it usually takes 100 - 200 dimensionless time units $t^* = tu_r/d$ for the suspensions to reach steady states. The duration of the transients seems to decrease with increasing ϕ. The length of the steady states, from which we calculated the volume fraction and velocity profiles, are usually 400 - 800 in terms of t^*.

In our simulations, the rise velocity of bubbles is not an input parameter. Rather, it depends on the gravity and the average bubble concentration in the suspension. The gravity and the number of bubbles in the suspensions, which determines ϕ, are the input parameters that we have direct control. The dimen-

sionless form of the gravity is the Archimedes number, defined as

$$\mathrm{Ar} = \frac{\rho^2 g d^3}{\eta^2} \ . \tag{6.5}$$

We chose the magnitudes of the gravity g such that they give Archimedes numbers of 87.8, 198, and 451, which, according to the single bubble simulations in Chapter 4, produce terminal Reynolds numbers of 5.4, 10 and 20. In suspensions, due to the hindering effect, the actual rising velocities are always smaller than the terminal velocities. In our simulations, we find that the rise velocities in slightly inclined channels are very close to the hindered rise velocities characterized in Chapter 5. The Reynolds numbers based on u_r are in the range of 4 - 16.

Fig. (6.2) shows an example of the volume fraction, and the fluid and bubble velocity profiles at the steady state. In the volume fraction profile, the bubble-rich layer near the upper wall and the depletion layer near the lower wall are very distinctive. In the middle of the channel ($4 < y/d < 10$), ϕ is nearly a constant, the value of which equals the averaged concentration of the suspension; the velocity profiles suggest that a linear shear flow is developed; the relative velocity u_r between the bubble phase and the fluid phase is also a constant. Thus, a nearly viscometric linear shear, with constant volume fraction, constant shear rate, and constant relative velocity between the two phases, is generated in this section of the channel. In the next section, we will analyze the force balance on the bubbles in these nearly viscometric shear regions and present the effective lift force coefficients.

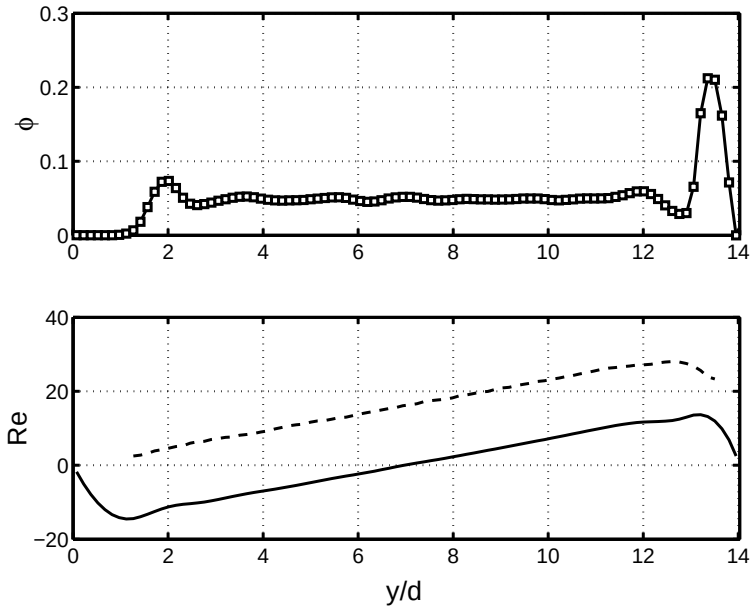

Figure 6.2: The volume fraction and the bubble and fluid velocity profiles in an inclined channel where Ar = 451, $\phi = 0.05$, and $\theta = 2°$. The Reynolds number based on the relative velocity between the bubbles and the fluid is 16.1. The top figure shows the volume fraction profile and the bottom one shows the bubble velocity profile (the dashed line) and the fluid velocity profile (the solid line).

6.3 Effective lift in a sheared suspension

Our simulations show that the bubbly flow in the middle of a slightly-inclined channel is very close to be an ideal one, with a linear shear and a homogeneous distribution of bubbles rising at a constant velocity relative to the continuous phase. In this nearly-ideal linear shear flow region, the bubble phase pressure [57, 121], which is related to the fluctuating motions of the bubbles, has no spatial variation. The bubble phase pressure does not vary because all sources of the fluctuations, including the relative motion, the volume fraction, and the velocity gradient, are invariant in this region. Therefore, bubbles rising in this linear shear region do not experience a gradient in the bubble phase pressure, and they have a simple force balance that involves only the cross-stream buoyancy force from g_y, and the lift force F_L from the linear shear. With this simple balance, we can determine the effective lift force F_L in a sheared suspension and the corresponding effective lift force coefficients C_L^*. In contrast, in the experiments by Zenit *et al.*[140], a shear flow is also generated in the middle of the channel. However, the lift force on those high Re bubbles does not balance the buoyancy in the y direction, possibly due to the effect of the bubble phase pressure gradient. Apparently, when several forces are involved in the force balance, it is no longer easy to isolate the lift force and estimate its magnitude.

From the force balance between the lift and g_y, it is easy to obtain

$$C_L^* = \frac{g_y}{\alpha u_r} \ , \tag{6.6}$$

the dimensionless form of which is

$$C_L^* = \frac{\mathrm{Ar} \sin\theta}{\mathrm{Re}^2 \mathrm{Sr}} \ . \tag{6.7}$$

Table 6.1: The values of Re, Sr and C_L^* found in simulations with $\phi = 0.05$.

Ar	θ	Re	Sr	C_L^*	C_L	C_L^*/C_L
87.8	2°	4.36	0.20	0.80	0.33	2.4
	4°	4.56	0.45	0.66	0.36	1.8
198	2°	8.44	0.17	0.56	0.33	1.7
	4°	8.51	0.38	0.50	0.33	1.5
451	2°	16.1	0.14	0.42	0.36	1.2
	4°	16.2	0.29	0.42	0.36	1.2
	6°	16.2	0.46	0.39	0.36	1.1

The values of Re, Ar and C_L^* in our simulations are listed in Table 6.1 and Table 6.2. In these simulations, the width of the linear shear regions normalized by d is at least 6. We find that C_L^* in sheared suspensions are all higher than C_L of isolated bubbles. This result, which agrees qualitatively with Sunkaranarayanan and Sundaresan's simulations [119], suggests that the lift force in a sheared suspension is enhanced by the hydrodynamic interaction among bubbles. From the values of C_L^*/C_L, it is easy to see that the difference between C_L^* and C_L is most remarkable in lower Re suspensions, and it increases with increasing bubble concentration in the range of ϕ that we have simulated.

As the shear flow in the middle of an inclined channel is driven by the moment that comes from the buoyancy difference between the bubble-rich layer and the depletion layer, it is of great interest to find out how thick these layers need to be in order to produce the desired moment and thus the correct lift force to balance g_y. Using Eq. (6.6) and C_L^* tabulated in Table 6.1 and Table 6.2, we can build

Table 6.2: The values of Re, Sr and C_L^* found in simulations with $\phi = 0.10$.

Ar	θ	Re	Sr	C_L^*	C_L	C_L^*/C_L
	2°	3.78	0.20	1.08	0.34	3.2
87.8	4°	3.92	0.40	1.00	0.37	2.7
	6°	3.95	0.64	0.93	0.40	2.3
	2°	7.37	0.18	0.72	0.32	2.2
198	4°	7.44	0.34	0.72	0.33	2.2
	6°	7.50	0.54	0.68	0.34	2.0
	2°	14.3	0.16	0.48	0.35	1.4
451	4°	14.4	0.30	0.51	0.35	1.4
	6°	14.4	0.44	0.51	0.35	1.4

a simple analytical model to calculate the thicknesses of the wall layers. As the simulation data suggest, when the flow in a slightly inclined channel reaches the steady state, in the middle of the channel the volume fraction equals approximately the average volume fraction of the suspension. Based on this observation, we can use a step function to represent the distribution of bubbles in a slightly inclined channel

$$\phi(y) = \begin{cases} 0 & , \quad 0 < y < H_1 \\ \phi_0 & , \quad H_1 < y < L_y - H_2 \\ \left(1 + \frac{H_1}{H_2}\right)\phi_0 & , \quad L_y - H_2 < y < L_y \end{cases} , \tag{6.8}$$

where the thicknesses of the wall layers, H_1 and H_2, are undetermined parameters. Here we require that the volume fraction in the middle of the channel equals ϕ_0. The volume fraction in the bubble-rich layer can thus be determined from the condition $\int_0^{L_y} \phi \mathrm{d}y = \phi_0 L_y$.

Assuming that the average fluid flow in the channel is one-dimensional at the steady state, we can write down the x-momentum equation of the fluid phase as

$$\eta_j \frac{\mathrm{d}^2 u_x}{\mathrm{d}y^2} - \frac{\mathrm{d}p}{\mathrm{d}x} + \phi(y)\rho g_x = 0 \ , \tag{6.9}$$

where the term $\phi(y)\rho g_x$ describes the body force acting on the fluid due to the presence of bubbles, and the term $\mathrm{d}p/\mathrm{d}x$ is the reverse pressure gradient which keeps the average fluid velocity zero. The term η_i describes the apparent viscosity in the depletion layer ($j = 1$), linear shear region ($j = 2$), and the bubble-rich layer ($j = 2$). Here we assume that they all equal the viscosity of the continuous phase *. Since $\mathrm{d}p/\mathrm{d}x = \phi_0 \rho g_x$, we can rewrite Eq. (6.9) into

$$\eta_j \frac{\mathrm{d}^2 u_x}{\mathrm{d}y^2} + \left[\phi(y) - \phi_0\right] \rho g_x = 0 \ . \tag{6.10}$$

When we substitute Eq. (6.8) into Eq. (6.10), it becomes apparent then that the excess of bubbles near the upper wall and the deficit of bubbles near the lower wall produce non-zero body forces in the wall layers, which, in turn, generate a moment and put the suspension into a shearing motion.

From Eq. (6.10), we can also determine the shape of the fluid velocity profile. Since $\phi(y) = \phi_0$ in the middle of the channel, u_x must be a linear function of y; in the wall layers, on the other hand, $\phi(y)$ does not equal ϕ_0, thus u_x must have a quadratic dependence on y. Integrate the momentum equation Eq. (6.10) with

*This assumption neglects the influence of the finite volume fraction on the apparent viscosity and thus is only a crude estimate. However, the velocity profiles obtained based on this assumption, which are perfectly symmetric about the channel centerline, turn out to be fairly close to the actual profiles at low inclination angles.

respect to y, and we have

$$u_x = \begin{cases} A_1 y^2 + B_1 y + C_1 & , \quad 0 < y < H_1 \\ B_2 y + C_2 & , \quad H_1 < y < L_y - H_2 \\ A_3 y^2 + B_3 y + C_3 & , \quad L_y - H_2 < y < L_y \end{cases} , \tag{6.11}$$

where the coefficients A_i, B_i, C_i are also undetermined parameters.

Including H_1 and H_2, the total number of unknowns in Eq. (6.11) is 10 and we need the same number of equations to solve them. The no-slip boundary condition at $y = 0$ and $y = L_y$, and the continuity of the velocity and the stress at $y = H_1$ and $y = L_y - H_2$ provide 6 equations; the momentum equations in the wall layers [Eq. (6.10)], and the constraint of no net fluid flow $\int_0^{L_y} u_x \mathrm{d}y = 0$ provide 3 more. It turns out that the balance between the lift force and the cross-stream gravity g_y, Eq. (6.6), is the last equation needed to close this model. Take a channel that is inclined 2° from the vertical direction and with Ar = 87.8 and $\phi = 0.10$ for an example, one can look up the value of C_L^* from Table 6.2 and calculate the velocity gradient $\alpha = B_2$ from Eq. (6.6). The rest of the unknowns can then be determined from the boundary conditions and the momentum equations. In Fig. (6.3), we plotted the fluid velocity profile $u(y)/u_r$ and the volume fraction profile solved from the model, together with the actual profiles obtained from the simulation. It can be observed that the model predictions are very close to the actual profiles.

It is of interest to calculate and compare the first order moments of the volume fraction profiles

$$M = \frac{4}{\phi_0 L_y^2} \int_0^{L_y} [\phi(y) - \phi_0] \left(y - \frac{L_y}{2} \right) \mathrm{d}y \ , \tag{6.12}$$

from the model and the simulations. In Eq. (6.12), ϕ_0 is used to denote the average volume fraction in the suspension. Clearly, M is a measure of the moment that

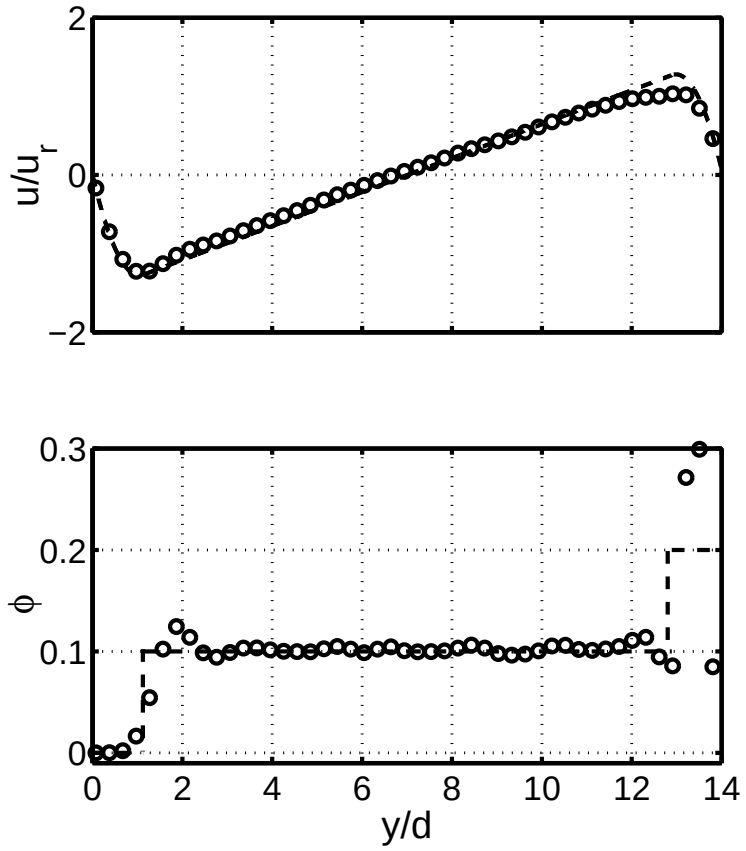

Figure 6.3: The profiles solved from the model Eqs. (6.8) and (6.11) compared to the profiles from the simulation. Re = 5, $\phi = 0.10$, and $\theta = 2°$. The dashed lines are the model predictions and the symbols are simulation results.

Table 6.3: The first order moments of the volume fraction distributions in inclined channels. The numbers before the slash are the moments from simulations; the numbers after the slash are the predictions of the model Eqs. (6.8) and (6.11).

Ar	ϕ	$\theta = 2^\circ$	$\theta = 4^\circ$	$\theta = 6^\circ$
87.8	0.05	0.494/0.421	0.888/0.596	
	0.10	0.271/0.288	0.488/0.400	0.618/0.489
198	0.05	0.434/0.368	0.723/0.518	
	0.10	0.244/0.255	0.383/0.349	0.520/0.426
451	0.05	0.365/0.314	0.549/0.425	0.784/0.521
	0.10	0.215/0.226	0.316/0.302	0.416/0.363

drives the suspension into a shearing motion. If $\phi = \phi_0$ everywhere in the channel, $M = 0$. On the other hand, if $\phi = 2\phi_0$ in one half of the channel and $\phi = 0$ in another, $M = 1$. We calculated the values of M in our simulations and listed them in Table 6.3. Not surprisingly, the values of the moments increase with increasing inclination angle. We also included the moments calculated from the model Eqs. (6.8) and (6.11). It can be observed that the best agreement between the model and the simulations occurs at the lowest inclination angle of $\theta = 2^\circ$. When the inclination angle increases, the difference between the simulations and the model predictions grows, possibly by the fact that at higher inclination angles, the simulation profiles are not perfectly symmetric and the volume fraction in the middle is slightly less than the average volume fraction ϕ_0. But M from model predictions do follow the same trend as M from simulations.

We have mentioned in Section 6.2 that only the right combination of Re, θ,

and ϕ can lead to the desired stable equilibrium state with a linear shear flow region in the middle of the channel. We conducted more simulations to probe the borders of the regions of acceptable (Re, θ) and plotted the results in Fig. (6.4). We find that the deviation from the desired ideal flow state occurs first as a drop in the volume fraction in the middle of the channel. Thus, in Fig. (6.4) we use $\phi_0 - \phi \leq 0.01$ as a criterion. It can be seen that the range of acceptable inclination angles increases with increasing Re and ϕ. This dependence on Re and ϕ, we think, can be understood as follow. First, the lift force on spherical bubbles is an inertial effect. Therefore, the Reynolds number of the bubbles need to be at least moderate such that the lift force can balance g_y. Second, in the model, the moment produced by the wall layers is directly proportional to the average volume fraction ϕ_0. Thus, at the same inclination angle, the wall layer thickness needed to generate a shear flow to balance g_y is less in a suspension with higher ϕ_0 than in a suspension with lower ϕ_0. In addition, the fact that C_L^* increases with increasing volume fraction also helps to reduce the thicknesses of the wall layers and increase the range of acceptable θ.

In Fig. (6.5), we show the volume fraction and velocity profiles of two bubbly flows where the input parameters do not lead to the desired viscometric linear shear flow state. The first example is a low Re bubbly flow with $\mathrm{Re} = 0.1$ and $\phi = 0.05$, which shows that if Re is too small, there is not enough lift force to balance g_y and nearly all bubbles move to the upper wall even when $\theta = 2^\circ$. The second example is a high Re bubbly flow with $\mathrm{Re} = 20$ and $\phi = 0.10$. The inclination angle is 10°. This example shows that at higher Re, when deviation from the viscometric state occurs, the flow in the middle is still approximately a linear one; the volume fraction, however, is no longer uniform. Clearly, for such a flow, one must consider

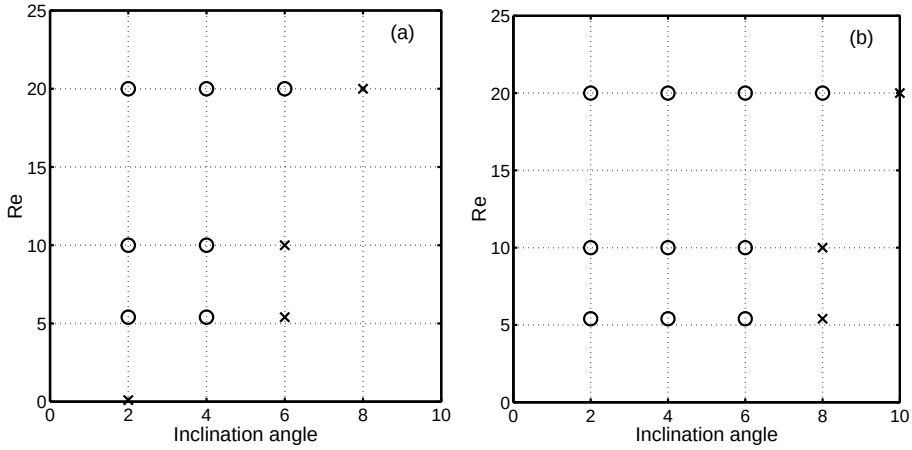

Figure 6.4: The parametric range where one can obtain a linear shear flow of a homogeneous suspension. (a): $\phi = 0.05$; (b): $\phi = 0.10$. The circles represent the simulations from which we have successfully generated such flows; the crosses represent the failures. Here the Reynolds numbers are defined based on the terminal velocity u_t.

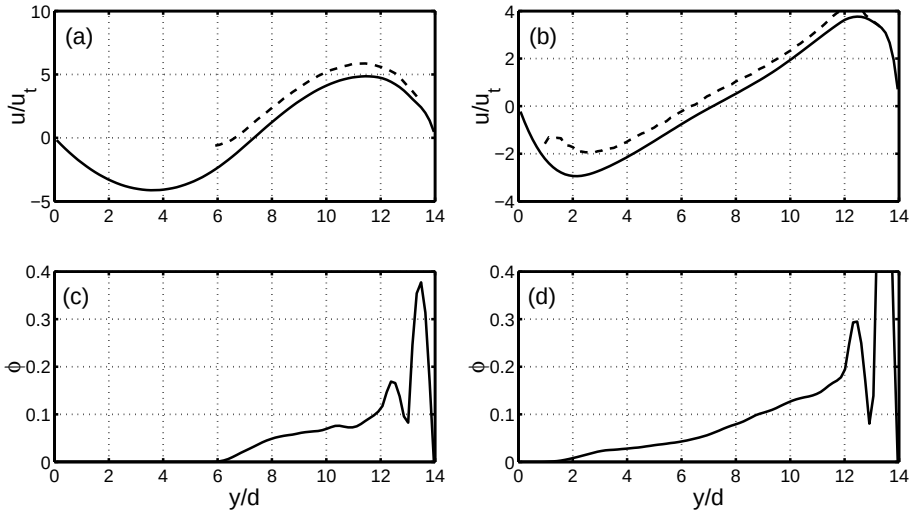

Figure 6.5: Examples of non-viscometric flows in inclined channels. Left: Re = 0.1, $\phi = 0.05$, and $\theta = 2°$; right: Re = 20, $\phi = 0.20$, and $\theta = 10°$. (a) and (c) are the velocity profiles, where the solid lines represent the velocity of the fluid phase and the dashed lines represent the velocity of the bubble phase. (b) and (d) are the volume fraction profiles.

the effect of the gradient of the bubble phase pressure on the force balance of bubbles.

6.4 Experiments on bubbly flows in inclined channels

In this section, we present an experimental study on bubbly flows in inclined channels. In this study, we measured the bubble volume fraction and velocity profiles in a channel that is inclined 2° from the vertical direction. The average bubble concentration in the channel is $\phi = 0.1$. By using a mixture of glycerin (ACS grade) and water (HPLC grade), we were able to increase the viscosity of the

fluid phase and reduce the Reynolds numbers to 2 - 20, a range that is comparable to the simulations. As our experimental apparatus and measurement techniques are very similar to those used in Zenit *et al.*[140], here we will only give a brief description.

The experiments are conducted in an inclined channel that is 200 cm in height (x direction) and 20 cm in width (z direction). The gap thickness in the y direction in which the velocity gradient occurs is 2 cm. This 10:1 ratio of the length scales was designed to ensure that the flow in the channel is approximately two-dimensional and has negligible gradient in the z direction, which is similar to the condition in the simulations where we have assumed periodic conditions in x and z directions. Nitrogen bubbles are generated from a hexagonal array of capillaries (ID 0.1 mm) fixed at the bottom of the channel. In the fluid phase, we applied a mangesium sulfate concentration of 0.3 $mol \cdot l^{-1}$ to prevent bubble coalescence and boost the signal strength observed by the impedance probes, the characteristics of which will be introduced later. The size and aspect ratio of the bubbles are measured by a digital camera (Panasonic FZ-15, 2304×1728 pixels, 1/1000 s shutter speed) and are listed in Table 6.4, where it can be seen that the bubbles are highly monodisperse and nearly spherical. The size of the bubbles is in the range of 1.4 - 1.6 mm. The ratio of channel gap thickness to bubble size is thus in the range of 13-14, very close to the ratio of $L_y/d = 14$ ratio in the simulations. The statistical variation in the bubble size is about 0.1 mm.

When there is no gas flow, the free surface is located at 150 cm above the capillaries; when the gas flow is turned on, the free surface rises. After the free surface is stabilized at a new position, the average volume fraction of the suspension can be calculated from the ratio between the distance that the free surface has trav-

Table 6.4: A summary of experimental conditions and results. The kinematic viscosities were measured using capillary viscometers (Cannon Instrument Company) in a water bath at temperatures listed above. The temperature variation is approximately ± 1°C in the experiments and ± 0.2°C in the water bath. The Reynolds numbers are based on the relative velocities.

Exp. No.	1	2	3
glycerin /water (% wt.)	61/39	56/44	51/49
bubble size (mm)	1.46	1.56	1.44
aspect ratio	1.01	1.06	1.09
kinematic viscosity (m^2/s)	2.48×10^{-5}	9.48×10^{-6}	6.71×10^{-6}
temperature (°C)	22	21	21
Re	2.7	12	19
Sr	0.27	0.14	0.10
C_L^*	0.84	0.44	0.58

elled and the current height of the suspension. When the average volume fraction is about 0.1, the absolute error in the average volume fraction is approximately ± 0.01. The volume fraction profile in the y direction, on the other hand, must be determined using an impedance probe, designed to detect subtle changes in the electric field near the tip of the probe due to the passing of a bubble [139]. In the signal detected by the impedance probe, the passing of a bubble appears as a peak. By measuring the fraction of the signal that is above a given threshold value relative to the entire signal duration, one can get a measurement of the local volume fraction near the tip of the probe. When two such probes are separated in the vertical direction by a small distance, one can obtain the average rise velocity of the bubbles from the time correlation between the two signals. In our glycerin/water mixtures, the electric resistance of the fluids is much higher than that in an aqueous solution. Therefore, the salt concentration must be increased compared to the salt concentration used in the experiments by Zenit *et al.*[140, 138] to ensure that the signal strength of the impedance probe is usable. In our experiments, we arranged two impedance probes vertically and 1.4 mm apart from each other. The probes were then placed 120 cm above the capillaries. This distance, based on the duration of the transients observed in the simulations, is sufficient for the flow to reach the steady state. The tips of the probes, controlled by a micrometer thread, can move back and forth in the y direction with an accuracy of ± 0.2 mm. Thus, the volume fraction and bubble velocity profiles in an inclined channel can be measured. In our experiments, the sampling frequency of the impedance probe is set to 10 kHz, and the sampling time is 52.4 seconds. This setting allows us to have enough bubble passing events in the duration of a signal; it also has a reasonably high time resolution to ensure the accuracy of the measured bubble velocities. In

our measurements we find that the statistical variation in the bubble velocities is usually about 15% of the mean.

We measured the volume fraction and bubble velocity profiles in three different suspensions. The fractions of glycerin and water used in these suspensions are 61/39, 56/44, and 51/49 (% wt.). Based on our measurements in inclined channels, bubbles in these suspensions have Reynolds numbers of approximately 2.7, 12, and 19. Fig. (6.6) shows the volume fraction and bubble velocity profiles measured from these suspensions. It can be observed that in the two higher Reynolds number suspensions, the volume fraction in the middle of the channel has no significant variation. In the suspension with the lowest Re, the volume fraction fluctuations are higher but there is still no significant gradient in the profile. The bubble velocities fit reasonably well to linear functions of y. The 90% confidence intervals of α from these fits are 20% - 30% of the values shown in Fig. (6.6). These findings prove that the bubbly flow in the middle of our slightly inclined channel is quite similar to the nearly viscometric one observed in the simulations.

In order to determine the effective lift force coefficient C_L^* from experiments, one needs to know the velocity gradient α, the inclination angle θ, and the relative velocity u_r. Of these three parameters, the inclination angle is an input parameter of the system and the velocity gradient α can be obtained from linear regression. Although we do not have a direct measure of u_r in our experiments, as the simulation results suggest, the bubble velocity at the center of the channel is very close to u_r. Thus, we can use the bubble velocity at the center of the channel to approximate u_r and calculate the effective lift force coefficients from Eq. (6.6). In Fig. (6.7), we plotted C_L^* from both experiments and simulations, and compared them to C_L of an isolated bubble from Eq. (6.3) [79]. Despite of the rather large

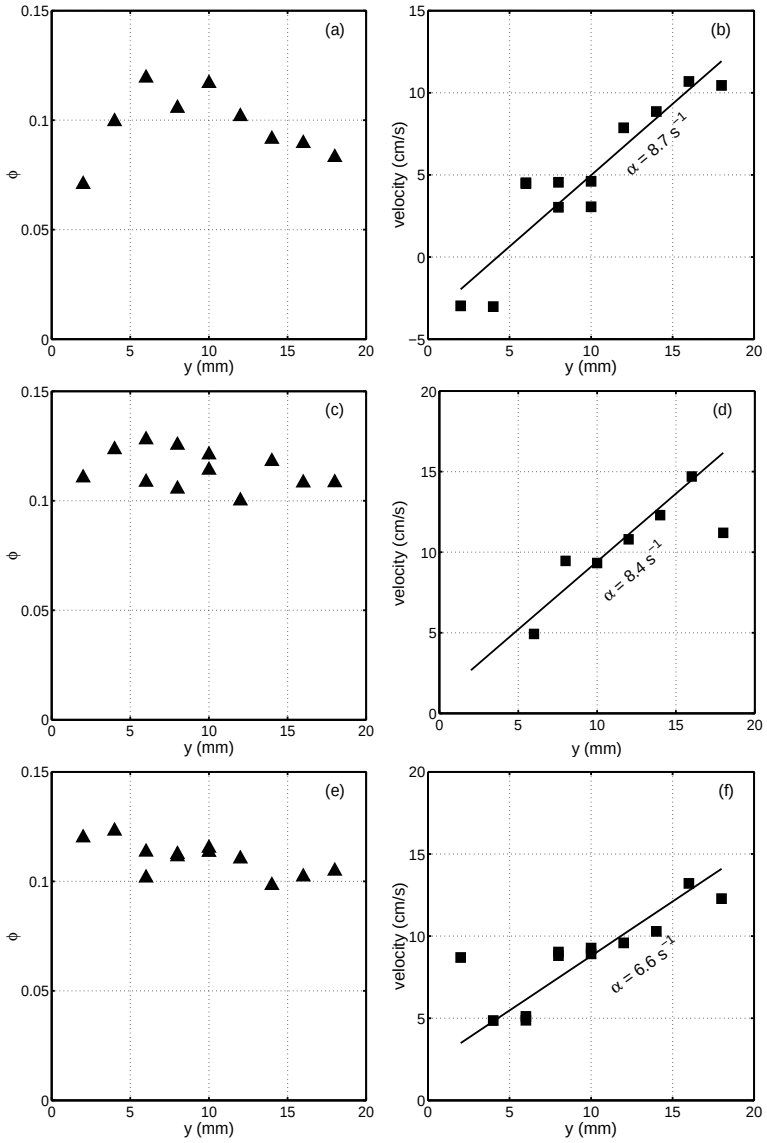

Figure 6.6: The volume fraction and bubble velocity profiles measured from experiments. The Reynolds numbers are 2.7 in (a) and (b), 12 in (c) and (d), and 19 in (e) and (f). (a), (c), and (e) are volume fraction profiles; (b), (d), and (f) are bubble velocity profiles. The solid lines accompanying the velocity profiles are the best linear fits, the slopes of which are also given in the plots.

error bars, which are mostly due to the variations in u_r and the uncertainties in α, one can see that C_L^* from experiments agree qualitatively with those from the simulations. Again, these experimental measurements suggest that the effective lift force in a sheared bubble suspension under the influence of the hydrodynamic interactions is indeed larger than the lift force of an isolated bubble.

6.5 Summary

In this work, we have generated a nearly ideal linear shear flow of a homogeneous suspension of monodisperse, spherical bubbles in the middle of a slightly inclined channel. In this linear shear region, the force balance on the bubbles in the direction perpendicular to the walls involves only the lift force from the linear shear, and a small component of the gravity from the finite angle of inclination. From this force balance, the effective lift force in a sheared suspension can be exactly determined. In our simulations, we characterized the effective lift force coefficients C_L^* in suspensions with different Reynolds numbers, shear rate, and volume fractions. We find that C_L^* is always higher than the lift force coefficient of an isolated spherical bubble C_L. The difference between C_L^* and C_L increases with increasing volume fraction, and decreases with increasing Re and local shear rate.

The linear shear, as it turns out, comes from an asymmetric distribution of bubbles. At the steady state, the volume fraction profiles feature a peak near one wall, and a deficit layer near another wall. In the middle of the channel, the volume fraction approximately equals the average volume fraction of the suspension. The difference in the buoyancy between the two wall layers, therefore, produces a moment and drives the suspension into a shearing motion. With the characterization

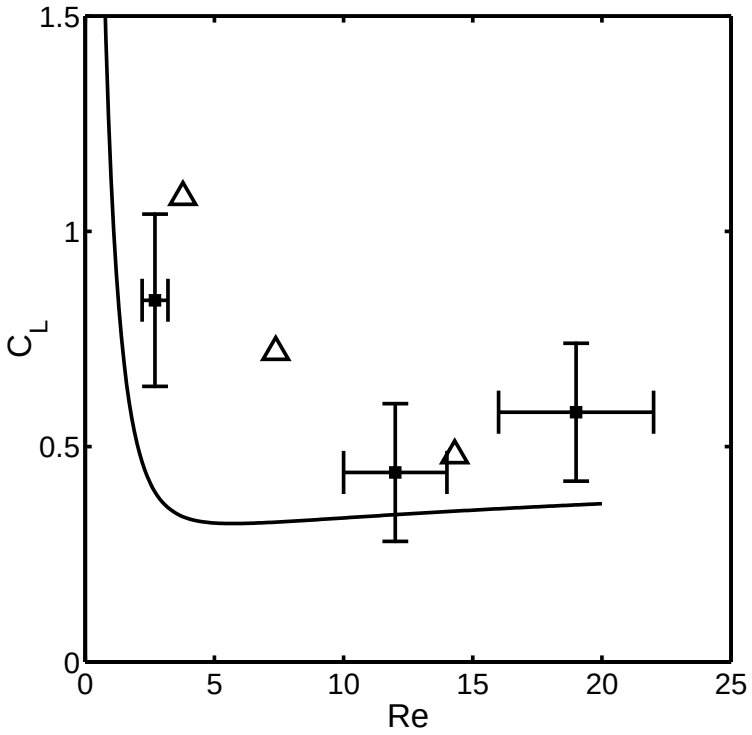

Figure 6.7: The lift force coefficients in an inclined channel with $\phi = 0.10$ and $\theta = 2°$. The triangles are the effective lift force coefficients obtained from simulations; the solid squares are the effective lift force coefficients measured from experiments, with error bars representing the errors propagated from u_r and α. The solid line corresponds to C_L of an isolated bubble calculated from Eq. (6.3) using $\mathrm{Sr} = 0.2$.

of the effective lift, we show the thicknesses of the wall layers can be determined from a simple analytical model.

In order to verify the simulation results, we conducted bubbly flow experiments in a slightly inclined channel where $\theta = 2^\circ$ and $\phi = 0.1$. We used glycerin/water mixtures in our experiments such that the Reynolds numbers in the experiments fall into the range of our simulations. The measured bubble volume fraction and velocity profiles support the finding from the simulations that there is a nearly viscometric linear shear flow in the middle of the channel. The effective lift force coefficients from the experiments also agree with those from the simulations.

BIBLIOGRAPHY

[1] N. W. Ashcroft and D. C. Langreth. Structure of binary liquid mixtures. I. *Phys. Rev.*, 156(3):685–692, 1967.

[2] T. R. Auton. The lift force on a spherical body in a rotational flow. *J. Fluid Mech.*, 197:241–257, 1987.

[3] E. Barnea and J. Mizrahi. A generalized approach to the fluid dynamics of particulate systems. Part 1. General correlation for fluidization and sedimentation in solid multiparticle systems. *Chem. Eng. J.*, 5:171–189, 1973.

[4] G. K. Batchelor. Sedimentation in a dilute dispersion of spheres. *J. Fluid Mech.*, 52:245–268, 1972.

[5] A. Biesheuvel and L. Van Wijngaarden. The motion of pairs of gas bubble in a perfect liquid. *J. Eng. Math.*, 16:349–365, 1982.

[6] S. Biswas, A. Esmaeeli, and G. Tryggvason. Comparison of results from DNS of bubbly flows with a two-fluid model for two-dimensional laminar flows. *Int. J. Multiphase Flow*, 31:1036–1048, 2005.

[7] M. Bouzidi, M. Firdaouss, and P. Lallemand. Momentum transfer of a Boltzmann-lattice fluid with boundaries. *Phys. Fluids*, 13(11):3452–3459, 2001.

[8] M. P. Brenner. Screening mechanisms in sedimentation. *Phys. Fluids*, 11:754, 1999.

[9] H. F. Bulthuis, A. Prosperetti, and A. S. Sangani. Particle stress in disperse two-phase potential flow. *J. Fluid Mech.*, 294:1–16, 1995.

[10] B. Bunner and G. Tryggvason. Dynamics of homogeneous bubbly flows. Part 1. Rise velocity and microstructure of the bubbles. *J. Fluid Mech.*, 466:17–52, 2002.

[11] B. Bunner and G. Tryggvason. Dynamics of homogeneous bubbly flows. Part 2. Velocity fluctuations. *J. Fluid Mech.*, 466:53–84, 2002.

[12] B. Bunner and G. Tryggvason. Effect of bubble deformation on the properties of bubbly flows. *J. Fluid Mech.*, 495:77–118, 2003.

[13] R. Buscall, J. W. Goodwin, R. H. Ottewill, and T. F. Tadros. The settling of particles through Newtonian and non-Newtonian media. *J. Colloid Interf. Sci.*, 85(1):78–86, 1981.

[14] R. E. Calflisch and J. H. C. Luke. Variance in the sedimentation speed of a suspension. *Phys. Fluids*, 28:759, 1985.

[15] A. Cartellier and N. Rivière. Bubble-induced agitation and microstructure in uniform bubbly flows at small to moderate particle Reynolds numbers. *Phys. Fluids*, 13:2165–2181, 2001.

[16] H. Chen. Volumetric formulation of the lattice Boltzmann method for fluid dynamics: Basic concept. *Phys. Rev. E*, 58:3955–3963, 1998.

[17] H. Chen, S. Chen, and W. H. Matthaeus. Recovery of the Navier-Stokes equations using a lattice-gas Boltzmann method. *Phys. Rev. E*, 58:3955–3963, 1992.

[18] H. Chen, C. Teixeira, and K. Molvig. Realization of fluid boundary conditions via discrete Boltzmann dynamics. *Int. J. Mod. Phys. C*, 8:1281–1292, 1998.

[19] S. Chen and G. D. Doolen. Lattice Boltzmann method for fluid flows. *Ann. Rev. Fluid Mech.*, 30:329–364, 1998.

[20] S. Chen, Z. Wang, X. Shan, and G. D. Doolen. Lattice-Boltzmann computational fluid dynamics in three dimensions. *J. Stat. Phys.*, 68:379, 1992.

[21] S. Y. Chen, D. Martinez, and R. W. Mei. On boundary conditions in lattice Boltzmann methods. *Phys. Fluids*, 8:2527–2536, 1996.

[22] M. K. Cheung, R. L. Powell, and M. J. McCarthy. Sedimentation of noncolloidal bidisperse suspensions. *AIChE J.*, 42(1):271–276, 1996.

[23] Y. S. Chong, D. A. Ratkowsky, and N. Epstein. Effect of particle shape on hindered settling in creeping flow. *Powder Technol.*, 23:55–66, 1979.

[24] R. Clift, J. R. Grace, and M. E. Weber. *Bubbles, Drops and Particles.* Academic Press, 1978.

[25] E. Climent and M. R. Maxey. Numerical simulations of random suspensions at finite Reynolds numbers. *Int. J. Multiphase Flow*, 29:579–601, 2003.

[26] F. R. Cunha, G. C. Abade, A. J. Sousa, and E. J. Hinch. Modeling and direct simulation of velocity fluctuations and particle -velocity correlations in sedimentation. *J. Fluid Eng-T ASME*, 124:957–968, 2002.

[27] F. R. Cunha, A. J. Sousa, and E. J. Hinch. Numerical simulation of velocity fluctuations and dispersion of sedimentating particles. *Chem. Eng. Comm.*, 189:1105–1129, 2002.

[28] J. F. Davidson, R. Clift, and D. Harrison, editors. *Fluidization*, chapter 1. Academic Press, second edition, 1985.

[29] R. H. Davis and K. H. Birdsell. Hindered settling of semidilute monodisperse and polydisperse suspensions. *AIChE J.*, 34:123–129, 1988.

[30] D. d'Humières, I. Ginzburg, M. Krafczyk, P. Lallemand, and L.-S. Luo. Multiple-relaxation-time lattice Boltzmann models in three dimensions. *Philos. T. Roy. Soc. A*, 360:437–451, 2002.

[31] R. Di Felice. The sedimentation velocity of dilute suspensions of nearly monosized spheres. *Int. J. Multiphase Flow*, 25:559–574, 1999.

[32] R. Di Felice and E. Parodi. Wall effects on the sedimentation velocity of suspensions in viscous flow. *AIChE J.*, 42:927–931, 1996.

[33] P. C. Duineveld. The rise and shape of bubbles in pure water at high Reynolds number. *J. Fluid Mech.*, 292:325–332, 1995.

[34] A. Esmaeeli and G. Tryggvason. Direct numerical simulations of bubbly flows. Part 1. Low Reynolds number arrays. *J. Fluid Mech.*, 377:313–345, 1998.

[35] A. Esmaeeli and G. Tryggvason. Direct numerical simulations of bubbly flows. Part 2. Moderate Reynolds number arrays. *J. Fluid Mech.*, 385:325–358, 1999.

[36] A. Esmaeeli and G. Tryggvason. A direct numerical simulation study of the buoyant rise of bubbles at o(100) Reynolds number. *Phys. Fluids*, 17:093303, 2005.

[37] A. F. Fortes, D. D. Joseph, and T. S. Lundgren. Nonlinear mechanics of fluidization of beds of spherical particles. *J. Fluid Mech.*, 20:467–483, 1987.

[38] U. Frisch, D. d'Humières, B. Hasslacher, P. Lallemand, Y. Pomeau, and J.-P. Rivet. Lattice gas hydrodynamics in two and three dimensions. *Complex Systems*, 1:649, 1987.

[39] J. Garside and M. R. Al Dibouni. Velocity-voidage relationships for fluidization and sedimentation in solid-liquid systems. *Ind. Eng. Chem. Proc. Des. Dev.*, 16(2):206–214, 1977.

[40] I. Ginzbourg and P. M. Adler. Boundary flow condition analysis for the 3-dimensional lattice Boltzmann model. *J. Phys. II*, 4:191–214, 1994.

[41] I. Ginzbourg and D. d'Humières. Local second-order boundary methods for lattice-boltzmann models. *J. Stat. Phys.*, 84:927–971, 1996.

[42] E. Guazzelli. Evolution of particle-velocity correlations in sedimentation. *Phys. Fluids*, 13:1537–1540, 2001.

[43] J. M. Ham and G. M. Homsy. Hindered settling and hydrodynamic dispersion in quiescent sedimenting suspensions. *Int. J. Multiphase Flow*, 14(5):533–546, 1988.

[44] J. F. Harper. On bubbles rising in line at large reynolds numbers. *J. Fluid Mech.*, 351:289–300, 2005.

[45] H. Hasimoto. On the periodic fundamental solution of the Stokes equations and their application to viscous flow past a cubic array of spheres. *J. Fluid Mech.*, 5:317–328, 1959.

[46] X. He and L.-S. Luo. Lattice-Boltzmann model for the incompressible Navier-Stokes equation. *J. Stat. Phys.*, 88:927, 1997.

[47] X. He, Q. Zou, L.-S. Luo, and M. Dembo. Analytic solutions of simple flows and analysis of nonslip boundary conditions for the lattice-Boltzmann BGK model. *J. Stat. Phys.*, 87:115–136, 1997.

[48] R. J. Hill, D. L. Koch, and A. J. C. Ladd. The first effects of fluid inertia on flows in ordered and random arrays of spheres. *J. Fluid Mech.*, 448:213–241, 2001.

[49] R. J. Hill, D. L. Koch, and A. J. C. Ladd. Moderate-Reynolds-number flows in ordered and random arrays of spheres. *J. Fluid Mech.*, 448:243–278, 2001.

[50] H. H. Hu. Direct simulation of flows of solid-liquid mixtures. *Int. J. Multiphase Flow*, 22:335–352, 1996.

[51] H. H. Hu, N. A. Patankar, and M. Y. Zhu. Direct numerical simulations of fluid-solid systems using the arbitrary Lagrangian-Eulerian technique. *J. Comput. Phys.*, 169:427–462, 2001.

[52] T. Inamuro, T. Ogata, S. Tajima, and N. Konishi. A lattice-Boltzmann method for incompressible two-phase flows with large density differences. *J. Comp. Phys.*, 198:628–644, 2004.

[53] M. Ishii and N. Zuber. Drag coefficient and relative velocity in bubbly, droplet or particulate flows. *AICHE J.*, 25:843–855, 1979.

[54] A. A. Johnson and T. E. Tezduyar. Simulation of multiple spheres falling in a liquid-filled tube. *Comput. Method Appl. M.*, 134:351–373, 1996.

[55] A. A. Johnson and T. E. Tezduyar. 3D simulation of fluid-particle interac-

tions with the number of particles reaching 100. *Comput. Method Appl. M.*, 145:301–321, 1997.

[56] A. A. Johnson and T. E. Tezduyar. Advanced mesh generation and update methods for 3d flow simulations. *Comput. Mech.*, 23:130–143, 1999.

[57] S.-Y. Kang, A. S. Sangani, H.-K. Tsao, and D. L. Koch. Rheology of dense bubble suspensions. *Phys. Fluids*, 9(6):1540–1561, 1997.

[58] S. Kim and S. J. Karrila. *Microhydrodynamics — Principles and Selected Applications*. Dover, 2005.

[59] D. L. Koch. Kinetic theory for a monodisperse gas-solid suspension. *Phys. Fluids A*, 2:1711–1723, 1990.

[60] D. L. Koch. Hydrodynamic diffusion in dilute sedimenting suspensions at moderate Reynolds numbers. *Phys. Fluids A*, 5:1141–1155, 1993.

[61] D. L. Koch. Hydrodynamic diffusion in a suspension of sedimenting point particles with periodic boundary conditions. *Phys. Fluids*, 6:2894–2900, 1994.

[62] D. L. Koch and A. J. C. Ladd. Moderate Reynolds number flows through periodic and random arrays of aligned cylinders. *J. Fluid Mech.*, 349:31–66, 1997.

[63] D. L. Koch and A. S. Sangani. Particle pressure and marginal stability limits for a homogeneous monodisperse gas-fluidized bed: kinetic theory and numerical simulations. *J. Fluid Mech.*, 400:229–263, 1999.

[64] D. L. Koch and E. S. G. Shaqfeh. Screening in sedimenting suspensions. *J. Fluid Mech.*, 224:275, 1991.

[65] J. B. Kok. Dynamics of a pair of gas bubbles moving through liquid Part I. Theory. *Eur. J. Mech. B-Fluid*, 12:515–540, 1993.

[66] J. B. Kok. Dynamics of a pair of gas bubbles moving through liquid Part II. Experiment. *Eur. J. Mech. B-Fluid*, 12:541–560, 1993.

[67] T. Kumagai. Analytical solution to Oseen's equation for creeping flow around a spherical gas-bubble in liquid. *B. JSME*, 29(256):3367–3374, 1986.

[68] V. Kumaran and D. L. Koch. The effect of hydrodynamic interactions on the average properties of a bidisperse suspension of high Reynolds number, low Weber number bubbles. *Phys. Fluids A*, 5:1123–1134, 1993.

[69] E. Kuusela, J. M. Lahtinen, and T. Ala-Nissila. Sedimentation dynamics of spherical particles in confined geometries. *Phys. Rev. E*, 69:066310, 2004.

[70] A. J. C. Ladd. Dynamical simulations of sedimenting spheres. *Phys. Fluids A*, 5(2):299–310, 1993.

[71] A. J. C. Ladd. Numerical simulations of particulate suspensions via a discretized Boltzmann equation. Part 1. Theoretical foundation. *J. Fluid Mech.*, 271:285–309, 1994.

[72] A. J. C. Ladd. Numerical simulations of particulate suspensions via a discretized Boltzmann equation. Part 2. Numerical results. *J. Fluid Mech.*, 271:311–339, 1994.

[73] A. J. C. Ladd. Hydrodynamic screening in sedimenting suspensions of non-Brownian spheres. *Phys. Rev. Lett.*, 76(8):1392–1395, 1996.

[74] A. J. C. Ladd. Sedimentation of homogeneous suspensions of non-brownian sphers. *Phys. Fluids*, 9:491–499, 1997.

[75] A. J. C. Ladd. Effects of container walls on the velocity fluctuations of sedimenting spheres. *Phys. Rev. Lett.*, 88:048301, 2002.

[76] A. J. C. Ladd and R. Verberg. Lattice-Boltzmann simulations of particle-fluid suspensions. *J. Stat. Phys.*, 104:1191–1251, 2001.

[77] P. Lallemand and L.-S. Luo. Lattice-Boltzmann method for moving boundaries. *J. Comput. Phys.*, 184:406–421, 2003.

[78] D. Legendre and J. Magnaudet. A note on the lift force on a bubble or a drop in a low-Reynolds-number shear flow. *Phys. Fluids*, 9:3572–3574, 1997.

[79] D. Legendre and J. Magnaudet. Lift force on a bubble in a viscous linear shear flow. *J. Fluid Mech.*, 368:81–126, 1998.

[80] D. Legendre, J. Magnaudet, and G. Mougin. Hydrodynamic interactions between two spherical bubbles rising side by side in a viscous liquid. *J. Fluid Mech.*, 497:133–166, 2003.

[81] X. Lei, B. J. Ackerson, and P. Tong. Settling statistics of hard sphere particles. *Phys. Rev. Lett.*, 86:3300–3303, 2001.

[82] R. R. Lessard and S. A. Zieminski. Bubble coalescence and gas transfer in electrolitic aqueous solutions. *Ind. Eng. Chem. Fundam.*, 10:260–269, 1971.

[83] M. J. Lighthill. Drift. *J. Fluid Mech.*, 1:31–53, 1956.

[84] C. Y. Lim, C. Shu, X. D. Niu, and Y. T. Chew. Application of lattice-Boltzmann method to simulate microchannel flows. *Phys. Fluids*, 14(7):2299–2308, 2002.

[85] P. M. Lovalenti and J. F. Brady. The force on a bubble, drop, or particle in arbitrary time-dependent motion at small Reynolds number. *Phys. Fluids A*, 5(9):2104–2116, 1993.

[86] J. Magnaudet. Small inertial effects on a spherical bubble, drop or particle moving near a wall in a time-dependent linear flow. *J. Fluid Mech.*, 485:115–142, 2003.

[87] T. Maxworthy, C. Gnann, M. Kürten, and F. Durst. Experiments on the rise of air bubbles in clean viscous liquids. *J. Fluid Mech.*, 321:421–441, 1996.

[88] J. B. McLaughlin. Inertial migration of a small sphere in linear shear flows. *J. Fluid Mech.*, 224:261–274, 1991.

[89] R. Mei and R. J. Adrian. Flow past a sphere with small oscillation in the free stream velocity and unsteady drag at finite Reynolds number. *J. Fluid Mech.*, 237:323, 1992.

[90] R. Mei and J. F. Klausner. Unsteady force on a spherical bubble at finite Reynolds number with small fluctuations in the free-stream velocity. *Phys. Fluids A*, 4:63, 1992.

[91] R. Mei, J. F. Klausner, and C. J. Lawrence. A note on the history force on a spherical bubble at finite Reynolds number. *Phys. Fluids*, 6(1):418–420, 1994.

[92] R. W. Mei, L.-S. Luo, and W. Shyy. An accurate curved boundary treatment in the lattice Boltzmann method. *J. Comput. Phys.*, 155:307–330, 1999.

[93] G. Mo and A. S. Sangani. A method for computing Stokes flow interactions among spherical objects and its application to suspensions of drops and porous particles. *Phys. Fluids A*, 6(5):1637–1652, 1994.

[94] D. W. Moore. The boundary layer on a spherical gas bubble. *J. Fluid Mech.*, 16:161–176, 1963.

[95] D. W. Moore. The velocity of rise of distorted gas bubbles in a liquid of small viscosity. *J. Fluid Mech.*, 23:749–766, 1965.

[96] P. J. Mucha, S. Y. Tee, D. A. Weitz, B. I. Shraiman, and M. P. Brenner. A model for velocity fluctuations in sedimentation. *J. Fluid Mech.*, 501:71–104, 2004.

[97] N.-Q. Nguyen and A. J. C. Ladd. Lubrication corrections for lattice-Boltzmann simulations of particle suspensions. *Phys. Rev. E*, 66:046708, 2002.

[98] N.-Q. Nguyen and A. J. C. Ladd. Microstructure in a settling suspension of hard spheres. *Phys. Rev. E*, 69:050401, 2004.

[99] N.-Q. Nguyen and A. J. C. Ladd. Sedimentation of hard-sphere suspensions at low Reynolds number. *J. Fluid Mech.*, 525:73–104, 2005.

[100] H. Nicolai and E. Guazzelli. Effect of the vessel size on the hydrodynamic diffusion of sedimenting spheres. *Phys. Fluids*, 7:3, 1995.

[101] H. Nicolai, B. Herzhaft, E. J. Hinch, L. Oger, and E. Guazzelli. Particle velocity fluctuations and hydrodynamic self-diffusion of sedimenting non-Brownian spheres. *Phys. Fluids*, 7:12–23, 1995.

[102] T. W. Pan, D. D. Joseph, R. Bai, R. Glowinski, and V. Sarin. Fluidization of 1204 spheres: simulation and experiment. *J. Fluid Mech.*, 451:169–191, 2002.

[103] W. C. Park, J. F. Klausner, and R. Mei. Unsteady forces on spherical bubbles. *Exp. Fluids*, 19:167–172, 1995.

[104] R. N. Parthasarathy and G. M. Faeth. Turbulent dispersion of particles in self-generated homogenous turbulence. *J. Fluid Mech.*, 220:515–537, 1990.

[105] R. N. Parthasarathy and G. M. Faeth. Turbulent modulation in homogeneous dilute particle-laden flows. *J. Fluid Mech.*, 220:485–514, 1990.

[106] R. J. Phillips, J. F. Brady, and G. Bossis. Hydrodynamic transport properties of hard-sphere dispersions. I. Suspensions of freely mobile particles. *Phys. Fluids*, 31(12):3462–3472, 1988.

[107] Y. H. Qian, D. d'Humières, and P. Lallemand. Lattice BGK models for the Navier-Stokes equation. *Europhys. Lett.*, 17:479–484, 1992.

[108] S. Rapagná, R. Di Felice, L. G. Gibilaro, and P. U. Foscolo. Steady-state expansion characteristics of monosized spheres fluidized by liquids. *Chem. Engng. Commun.*, 79:131–140, 1989.

[109] J. P. Riba and J. P. Couderc. Expansion de couches fluidisées par des liquids. *Can. J. Chem. Engng.*, 55:118–121, 1977.

[110] J. F. Richardson and W. N. Zaki. Sedimentation and fluidization: part I. *Trans. Instn. Chem. Engrs.*, 32:35–53, 1954.

[111] F. Rouyer, D. Lhuillier, J. Martin, and D. Salin. Structure, density, and velocity fluctuations in quasi-two- dimensional non-brownian suspensions of spheres. *Phys. Fluids*, 12:958–963, 2000.

[112] P. G. Saffman. The lift force on a small sphere in a slow shear flow. *J. Fluid Mech.*, 22:385–400, 1965.

[113] A. S. Sangani and A. Acrivos. Slow flow through a periodic array of spheres. *Int. J. Multiphase Flow*, 8:343–360, 1982.

[114] A. S. Sangani and A. Acrivos. Creeping flow through cubic arrays of spherical bubbles. *Int. J. Multiphase Flow*, 9:181–185, 1983.

[115] A. S. Sangani and A. K. Didwania. Dynamic simulations of flows of bubbly liquids at large Reynolds numbers. *J. Fluid Mech.*, 250:307–337, 1993.

[116] A. S. Sangani, G. Mo, H.-K. Tsao, and D. L. Koch. Simple shear flows of dense gas-solid suspensions at finite Stokes numbers. *J. Fluid Mech.*, 313:309–341, 1996.

[117] K. Sankaranarayanan, X. Shan, I. G. Kevrekidis, and S. Sundaresan. Bubble flow simulations with the lattice Boltzmann method. *Chem. Eng. Sci.*, 54:4817–4823, 1999.

[118] K. Sankaranarayanan, X. Shan, I. G. Kevrekidis, and S. Sundaresan. Analysis of drag and virtual mass forces in bubbly suspensions using an implicit

formulation of the lattice Boltzmann method. *J. Fluid Mech.*, 452:61–96, 2002.

[119] K. Sankaranarayanan and S. Sundaresan. Lift force in bubbly suspensions. *Chem. Eng. Sci.*, 57:3521–3542, 2002.

[120] P. N. Segrè, E. Herbolzheimer, and P. M. Chaikin. Long-range correlations in sedimentation. *Phys. Rev. Lett.*, 79:2574–2577, 1997.

[121] P. D. M. Spelt and A. S. Sangani. Properties and averaged equations for flows of bubbly liquids. *Appl. Sci. Res.*, 58:337–386, 1998.

[122] S. Succi. Mesoscopic modeling of slip motion at fluid-solid interfaces with heterogeneous catalysis. *Phys. Rev. Lett.*, 89(6):064502, 2002.

[123] F. Takemura and J. Magnaudet. The transverse force on a clean or contaminated bubble rising near a vertical wall at moderate Reynolds number. *J. Fluid Mech.*, 495:235–253, 2003.

[124] F. Takemura, S. Takagi, J. Magnaudet, and Y. Matsumoto. Drag and lift forces on a bubble rising near a vertical wall in a viscous liquid. *J. Fluid Mech.*, 461:277–300, 2002.

[125] L. Talini, J. Leblond, and F. Feuillebois. A pulsed field gradient NMR technique for the determination of the structure of suspensions of non-Brownian particles with application to packings of spheres. *J. Magn. Reson.*, 132:287–297, 1998.

[126] J. Tölke, M. Krafczyk, M. Schulz, and E. Rank. Lattice-Boltzmann simula-

tions of binary fluid flow through porous media. *Phil. Trans. R. Soc. Lond. A*, 360:535–545, 2002.

[127] H.-K. Tsao and D. L. Koch. Collisions of slightly deformable, high Reynolds number bubbles with short-range repulsive forces. *Phys. Fluids*, 6:2591–2605, 1994.

[128] R. Verberg and A. J. C. Ladd. Lattice-Boltzmann model with sub-grid scale boundary conditions. *Phys. Rev. Lett.*, 84:2148–2151, 2000.

[129] R. Verberg and A. J. C. Ladd. Accuracy and stability of a lattice-Boltzmann model with subgrid scale boundary conditions. *Phys. Rev. E*, 65:016761, 2001.

[130] B. Wachmann, W. Kalthoff, S. Schwarzer, and H. Hermann. Collective drag and sedimentation: comparison of simulation and experiment in two and three dimensions. *Granular Matter*, 1(2):75–82, 1998.

[131] B. Wachmann and S. Schwarzer. Three-dimensional massively parallel computing of suspensions. *Int. J. Mod. Phys. C*, 9(5):759–775, 1998.

[132] A. J. Wagner. The origin of spurious velocities in lattice-Boltzmann. *Int. J. Mod. Phys. B*, 17:193–196, 2003.

[133] L. Van Wijngaarden. Hydrodynamic interaction between gas bubbles in liquid. *J. Fluid Mech.*, 77:27–44, 1976.

[134] S.-M. Yang and L. G. Leal. A note on the memory-integral contributions to the force on an accelerating spherical drop at low Reynolds number. *Phys. Fluids A*, 3(7):1822–1824, 1991.

[135] X. Yin, D. L. Koch, and R. Verberg. Lattice-Boltzmann method for simulating spherical bubbles with no-tangential stress boundary conditions. *Phys. Rev. E*, 73:026301, 2006.

[136] H. Yuan and A. Prosperetti. On the in-line motion of two spherical bubbles in a viscous fluid. *J. Fluid Mech.*, 278:325–349, 1994.

[137] Y. Yurkovetsky and J. F. Brady. Statistical mechanics of bubbly liquids. *Phys. Fluids*, 8(4):881–895, 1995.

[138] R. Zenit, D. L. Koch, and A. S. Sangani. Measurements of the average properties of a suspension of bubbles rising in a vertical channel. *J. Fluid Mech.*, 429:307–342, 2001.

[139] R. Zenit, D. L. Koch, and A. S. Sangani. Impedance probe to measure local gas volume fraction and bubble velocity in a bubbly liquid. *Rev. Sci. Instrum.*, 74:2817–2827, 2003.

[140] R. Zenit, Y. H. Tsang, D. L. Koch, and A. S. Sangani. Shear flow of a suspension of bubbles rising in an inclined channel. *J. Fluid Mech.*, 515:261–292, 2004.

[141] D. Z. Zhang and A. Prosperetti. Averaged equations for inviscid disperse two-phase flow. *J. Fluid Mech.*, 267:185–219, 1994.

[142] Y. Zhang, R. Qin, and D. R. Emerson. Lattice-Boltzmann simulation of rarefied gas flows in microchannels. *Phys. Rev. E*, 71:047702, 2005.

[143] L. Zhu, D. Tretheway, L. Petzold, and C. Meinhart. Simulation of fluid slip

at 3D hydrophobic microchannel walls by the lattice Boltzmann method. *J. Comput. Phys.*, 202(1):181–195, 2005.